N° d'ordre : 42023

UNIVERSITE DE LILLE I

THESE EN COTUTELLE INTERNATIONALLE

Présentée par

Alberto MEJIAS

Pour l'obtention du titre de :

DOCTEUR EN MECANIQUE, ENERGETIQUE ET MATERIAUX DE
L'UNIVERSITE DE LILLE I
ET
DOCTEUR EN INGÉNIERIE DE L'UNIVERSITE DE CARABOBO

Sur le thème :

DÉVELOPPEMENT DE L'INDENTATION MULTICYCLIQUE À L'ETUDE DES MATERIAUX MASSIFS, REVÊTUS ET HETEROGÈNES

Soutenue le **07 *juillet 2016*** devant le jury composé de :

Directeurs: **Didier CHICOT**, Professeur, Université de Lille I
Alberto PERTUZ, Professeur, Universidad Central de Venezuela (Venezuela)
Rapporteurs: **Eric LE BOURHIS**, Professeur, Université Poitiers
Gérard MAUVOISIN, Maître de Conférences HDR, Université Rennes I
Membres: **Olivier BARTIER**, Maître de Conférences, Université de Rennes I
Francine ROUDET, Maître de Conférences HDR, Université de Lille I
Alain IOST, Professeur, Arts et Métiers ParisTech
Puchi CABRERA, Professeur, Universidad Central de Venezuela (Venezuela)
Mariana H. STAIA, Professeur, Universidad Central de Venezuela (Venezuela)

N° d'ordre : 42023

UNIVERSITE DE LILLE I

Co-tutorial Ph.D. Thesis

presented by

Alberto MEJIAS

to obtain the degree of:

Ph.D. IN MECHANICAL, ENERGY AND MATERIALS OF THE
UNIVERSITY OF LILLE I
And
Ph.D. IN ENGINEERING OF THE UNIVERSITY OF CARABOBO

On the subject:

DEVELOPMENT OF MULTICYCLE INDENTATION TO STUDY SOLID, COATED AND HETEROGENEOUS MATERIALS

Defended on **July 7, 2016** in front of the jury:

Directors: **Didier CHICOT**, Professor, Université de Lille I
Alberto PERTUZ, Professor, Universidad Central de Venezuela (Venezuela)
Referees: **Eric LE BOURHIS**, Professor, Université Poitiers
Gérard MAUVOISIN, Lecturer HDR, Université Rennes I
Examiners: **Olivier BARTIER**, Maître de Conférences, Université de Rennes I
Francine ROUDET, Lecturer HDR, Université de Lille I
Alain IOST, Professor, Arts et Métiers ParisTech
Puchi CABRERA, Professor, Universidad Central de Venezuela (Venezuela)
Mariana H. STAIA, Professor, Universidad Central de Venezuela (Venezuela)

Acknowledgment

I have to thanks to God who gives me the life and the opportunity to be here, allowing me to finish successfully this Ph.D. thesis.

This work has been possible thanks to the financial support of the University of Carabobo (UC), who in spite of all difficulties made possible this academic formation. Concerning this great institute, I would like to thanks to Professor Laura SAENZ (Post-graduate director of the UC) to its support and attention on all the stages of this path.

As any undertaken project, sometimes there are inevitably moments of difficulties, but fortunately, I counted with the support and trust of my thesis director, Professor Didier CHICOT. I feel truly honored to work with you. Thanks for all the advices, for the conduction and above all for the opportunity to exploit my investigation skills. I have to express my gratitude for all the time that you invest with me to finish successfully this project. It has been honestly a gladness working with you. I hope we can keep working together in next years. Thanks again.

I also thanks to Professor Alberto PERTUZ co-director of this thesis, who encourage me to be part of this project, he was the first to support and orient me to initiate this work three years ago. Thank you very much.

I am honored and I really appreciate the gesture of M. Eric LE BOURHIS (Professeur, Université de Poitiers) and M. Gérard MAUVOISIN (Maître de Conférences HDR, Université Rennes I) by accepting to be reporters of this manuscript at l'Université de Lille 1.

Also, it has been an honor to me and I thank also to Mme. Francine ROUDET (Maître de Conférences HDR, Université de Lille 1), Mme. Mariana H. STAIA (Professeur, Universidad Central de Venezuela), M. Alain IOST (Professeur, Arts et Métiers ParisTech), M. Puchi CABRERA (Professeur, Universidad Central de Venezuela) and M. Olivier BARTIER (Maître de Conférences, Université de Rennes I) who accepted the invitation to be part of the thesis jury to examine my work.

I appreciate and express my gratitude to the Laboratoire de Mécanique de Lille (LML) for the support administrative and to l'écolde doctorale des Sciences pour l'Ingenieur for the various offered transversal programs to improve my investigation abilities.

I can forget to express my thanks to the IUT-A's group, specially to Xavier DECOOPMAN, Francine ROUDET, Ion Cosmin GRUESCU and Noureddine BENSEDDIQ for the great company, the coffee breaks and the advices received in this three years. Thanks to Abderrahim TALHA for his helpful assistance when I arrived here. I would also to express my gratitude to Alex MONTAGNE for his assistance at the ENSAM.

I must also show my appreciation to my colleagues Michel YETNA, Phillemon NOGNING KAMTA, and Stephania KOSSMAN for the support and the good shared moments. Good luck to all of you.

It has not been easy to be apart from my family, nevertheless, they have been there to support me in remote mode, one big thanks to my brothers, my sister and my wise and loved parents.

Specially, I want to thank to you, Scarling, my beautiful and beloved wife, for all magnificent and tremendous moments that we have shared this time.

General Index

Figure Index..v

Table Index...xi

Abstract..xiii

Nomenclature...xv

General Introduction.. 1

Chapter I: LITERATURE SUMMARY 5

I.1. INTRODUCTION 5

I.2. THE LOAD-DISPLACEMENT CURVE 6

I.2.1. Classical instrumented indentation test 6

I.2.2. Multicycle protocol tests.. 10

I.2.3. Continuous stiffness measurement (CSM) test. 11

I.3. CONTACT AREA FUNCTION... 13

I.3.1. Oliver and Pharr's contact area function [1] 13

I.3.2. Troyon et Huang's contact area description [21] 14

I.3.3. Chicot *et al.*'s contact area function [27]... 15

I.4. DATA CORRECTION FROM INSTRUMENTED INDENTATION TESTS 16

I.4.1. Frame compliance of the instrument... 16

I.4.2. Geometric correction factor.. 18

I.4.3. Material correction factor.. 19

I.5. DEFORMATION MODE AROUND THE RESIDUAL IMPRESSION 20

I.6. INDENTATION SIZE EFFECT.. 22

I.6.1. Li and Bradt's Model [44].. 22

I.6.2. Nix and Gao's Model [45].. 24

I.7. ANALYSIS OF HETEROGENEOUS MATERIALS.. 26

I.8. ANALYSIS OF FILM-SUBSTRATE SYSTEMS.. 28

I.8.1. Elastic modulus from thin films 28

I.8.2. Hardness from thin films........ 30

I.8.3. Elastic modulus from multilayer coating systems........ 32

I.8.4. Hardness from multilayer coating systems........ 35

I.9. CONCLUSIONS........ 38

Chapter II: MATERIALS AND EXPERIMENTS........ 41

II.1. INTRODUCTION 41

II.2. MATERIALS........ 41

II.2.1. Carbon steel samples........ 41

II.2.2. Hydroxyapatite coating specimens 42

II.2.3. Carbon steels coated with a bilayer electroless Ni-P deposits........ 44

II.2.4. Metallography preparation and polishing 46

II.3. INDENTATION EXPERIMENTS........ 47

II.3.1. Fundaments of the Instrumented Indentation Test (IIT) 47

II.3.2. Description of instruments........ 47

II.3.3. The experimental design of the instrumented indentation test 50

Chapter III: RESULTS AND DISCUSSION 53

III.1. EVALUATION OF HARDNESS AND ELASTIC MODULUS OF CARBON STEEL SAMPLES BY CONTINUOUS MULTICYCLE INDENTATION TESTS AND CONTINUOUS STIFFNESS MEASUREMENT 54

III.1.1. Mechanical properties evaluated by continuous multicycle indentation tests 54

III.1.2. Contact area from the nanoindentation experimental contact stiffness 62

III.1.3. Conclusions........ 71

III.2. MECHANICAL PROPERTIES BY MULTICYCLE INDENTATION TEST FROM HETEROGENEOUS SAMPLES 72

III.2.1. Introduction........ 72

III.2.2. Microstructure of hydroxyapatite coating samples 73

III.2.3. Surface condition of hydroxyapatite coatings 76

III.2.4. Mechanical properties from continuous multicycle Indentation tests. 76

III.2.5. Discussion.. 84

III.2.6. Conclusions... 90

III.3. MECHANICAL PROPERTIES BY MULTICYCLE INDENTATION TEST FROM A BILAYER COATING SYSTEMS.. 91

III.3.1. Introduction... 91

III.3.2. Mechanical properties from bilayer coating system 92

III.3.3. Discussion... 102

III.3.4. Conclusions.. 111

General Conclusions.. 113

References 117

Figure Index

Figure I.2-1. Load-unload cycle from a standard instrumented indentation test. 6

Figure I.2-3. SEM micrograph from the residual impression left by a Berkovich indenter on a Hydroxyapatite coating sample. 7

Figure I.2-4. Profile from load-displacement curve recorded froma standadrd instrumented indentation test. 7

Figure I.2-5. Profile of the load-displacement curve from a indentation test running a multicycle procol. 11

Figure I.2-6. Representative scheme of the continuous stiffness measurements (CSM) mode. 12

Figure I.3-1. Rigid cone with a vertical semi-angle ψ and a spherical cap of radius R modelling the blunt defect of the indenter tip. 14

Figure I.4-1. Total compliance (CT) versus the reciprocal of the square root of the contact area ($1/AC$) from the data acquired by IIT over a carbon steel sample. 17

Figure I.4-2. Deformed surface considering it as the same that a rigid cone or sligtly curved instead. 19

Figure I.5-1. Shematic representation of sink-in and pile-up phenomenon around the indenter. 20

Figure I.8-1. Multilayer coating system sheme to analyze the contribution of each layer to the composite elastic modulus by means of the models advanced by Rahmoun *et al.* [68] and modified by Puchi-Cabrera *et al.* [69] 33

Figure I.8-2. Composite hardness variation of a multilayer coatings from a galvanized steel as a function of the indenter displacement into surface for the for a bath immersion of 7 min. 37

Figure I.8-3. Contribution of each layer from the multilayer coating from galvanized steel specimen to the composite hardness. 38

Figure II.2-1. SEM images of sample using a low solution concentration of CA/P. Sample surface is showed (left) and its corresponding cross-section (right) 43

Figure II.2-2. SEM micrograph of sample using a high concentration solution of Ca/P. The surface of the sample is exhibit (left) and its corresponding cross-section (right) 43

Figure II.3-1. SEM image from the bilayer electroless Ni-P coating deposited on SAE 10210 carbon steel plate. 45

Figure II.3-2. EDS analysis performed to identify the possible diffusion process between the coating and hardness. Fe element is absent in the electroless Ni-P coating (left), Ni element inattentive in the substrate (center) and existence of P element in both substrate and coating but more important in the electroless Ni-P coating (right). 46

Figure II.3-3. Scheme of the heat treatment of every single electroless Ni-P deposited on substrate plates. 46

Figure II.6-1. Microhardness indenter CSM 2–107 manufactured by CSM instruments used to perform the instrumented indentation tests at the microscale range. 48

Figure II.6-2. Schematic of instrumented indentation test at both nanoscale and microscale. 48

Figure III.1-1. Load-displacement curve registered by standard indentation tests accomplished on a SAE 1020 carbon steel specimen at maximum loads of 1, 3, 4, 6 and 10 N. 55

Figure III.1-2. Load-displacement curve performed by a continuous multicycle indentation test on a steel sample. 56

Figure III.1-3. Ratio of hf to hm $(\Delta = hf/hm)$ representation as function of the maximum indentation depth (hm) derived from every single cycle. 57

Figure III.1-4. Estimation of the tip defect dimension for the utilized Berkovich indenter by means of an emission field SEM analysis. 57

Figure III.1-5. Total compliance (CT), or reciprocal of the experimental contact stiffness (1/S), as function of the reciprocal square root of contact area $(1/AC)$. 58

Figure III.1-6. Elastic modulus of a SAE 1020 carbon steel sample computed from a continuous multicycle indentation test. 59

Figure III.1-7. Martens hardness (HM) versus the reciprocal of the maximum indentation depth $(1/h\max)$ for the SAE 1045 carbon steel sample by the proportional specimen resistance model applied to hardness computed from multicycle indentation data. 60

Figure III.1-8. Square of Martens hardness $(HM2)$ versus the reciprocal of the maximum indentation depth $(1/h\mathrm{m})$ for the SAE 1045 carbon steel sample by applying the strain gradient plasticity model to hardness from multicycle indentation data. 61

Figure III.1-9. Comparison of the experimental contact stiffness computed from the contact area functions advanced by Oliver and Pharr [1] and Chicot *et al.* [27] considering $100 < h\mathrm{max} < 1900$ nm 65

Figure III.1-10. Fraction difference between the experimental contact stiffness and the predicted one evaluated from the Oliver and Pharr' contact area function [1] and the one proposed by Chicot *et al.* [27] considering $100 < h\mathrm{max} < 1900$ nm. 66

Figure III.1-11. Comparison of the contact stiffness by replacing the contact area function defined by Oliver and Pharr [20] and Chicot et al. [21] in Eq. (III.1-2) and considering $4 < h\max < 50$ nm. 67

Figure III.1-12. Fraction difference between the experimental contact stiffness and the contact stiffness evaluated from the contact area functions of Oliver and Pharr [20] and Chicot *et al.* [21] considering $4 < h\max < 50$ nm. Contact stiffness models work better at depths greater than 10 nm. 67

Figure III.2-1. SEM micrographs of sample H-2 (high solution concentration) at the surface of the hydroxyapatite coating sample. 73

Figure III.2-2. SEM micrographs of sample H-2 (prepared with a high solution concentration) at the cross-section of the hydroxyapatite coating sample. 74

Figure III.2-3. SEM micrographs of sample L-3 (prepared with a low solution concentration) at the surface of the hydroxyapatite coating sample. 74

Figure III.2-4. SEM micrographs of sample L-3 (prepared with a low solution concentration) at the cross-section of the hydroxyapatite coating sample. 75

Figure III.2-5. XRD diagram of selected coatings prepared using high concentration (H-2) and low concentration (L-3) of solution precursors indexed to standard diffraction file of HA. 75

Figure III.4-1. Load-displacement curve from a continuous multicycle indentation tests between 1 N and 20 N performed on a SPPS-HA coating sample. 76

Figure III.4-2. Ratio of the residual depth to maximum indentation depth ($hf/h\max$) from a SPPS-HA coating sample at each cycle evaluated by a continuous multicycle indentation test. 77

Figure III.4-3. Martens hardness computed from SPPS-HA coating samples by continuous instrumented indentation tests. 78

Figure III.4-4. Martens Hardness and the non-linear least square analysis using the advanced model described by Eqs. (III.2-3) and (III.2-4). 79

Figure III.4-5. SEM micrograph after multicycle indentation test of the hydroxyapatite coating sample H-2 (high solution concentration) showing the indenter print into surface. 81

Figure III.4-6. SEM images after multicycle indentation experiment of sample L-3 (low solution concentration) showing the residual indenter print into surface. 82

Figure III.4-7. Reciprocal of contact stiffness as a function of the reciprocal of the square root of contact area for representative samples H-2 and L-3. 83

Figure III.4-8. Elastic modulus versus the maximum indentation depth for representative samples H-2 and L-3. 84

Figure III.5-1. Models describing the elastic modulus of the hydroxyapatite coating samples (specimens prepared with high solution concentration) as function of the crystallinity volume fraction. 89

Figure III.5-2. Models describing the hardness of the hydroxyapatite coating specimens (samples produced using high solution concentration) versus the crystallinity volume fraction. 89

Figure III.8-1. Load-displacement curve from a continuous multicycle indentation test performed on a bilayer electroless Ni-P coating deposited on a carbon steel plate. 93

Figure III.8-2. Load-displacement curve from a CSM test performed on electroless Ni-P bilayer coating deposited on a carbon steel substrate. 93

Figure III.8-3. Load-displacement curve from multicycle indentation test performed on a electroless Ni-P bilayer coating deposited on a carbon steel substrate. The pile-up effect is noticeable around the indenter impression. 94

Figure III.8-4. SEM micrograph of the residual impression from a Berkovich indenter on the sample labeled as 1020-B submitted to a continuous multicycle indentation test. 94

Figure III.8-5. SEM images from a residual impression from a Berkovich indenter on the sample labeled as 1020-B after standard indentation test is accomplished. 95

Figure III.8-6. Load-displacement curve from multicycle indentation test performed on a electroless Ni-P bilayer coating deposited on a carbon steel substrate. The crack on corners of the indenter impression is related to the large horizontal displacement on the load-displacement curve. 95

Figure III.8-7. Load-displacement curve from multicycle indentation test performed on a electroless Ni-P bilayer coating deposited on a carbon steel substrate. The chipping remarked on the indenter impression is related to the hysteresis loop observed in the load-displacement curve. 96

Figure III.8-8. SEM micrograph from the residual impression from a Berkovich indenter on the sample labeled as 1020-I after a continuous multicycle indentation test of 100 cycles is accomplished. 97

Figure III.8-9. SEM micrograph from the residual impression from a Berkovich indenter on the sample labeled as 1020-I after standard indentation test with a maximum applied load 1 N is accomplished. 97

Figure III.8-10. SEM micrograph from the residual impression from a Berkovich indenter on the sample labeled as 1020-I after standard indentation test with a maximum applied load 18 N is accomplished. 98

Figure III.8-11. Calibration curve of Berkovih indenter to be employed in CSM tests on NI-P coatings. Fused silica specimen was used as the standard sample. The elastic modulus of fused silica remains constant from about 10 nm. 99

Figure III.8-12. Elastic modulus recorded by CSM test from a bilayer Ni-P coating system performed up to a depth penetration of 2000 nm. 99

Figure III.8-13. Elastic modulus from CSM tests and continuous multicycle tests performed on a bilayer NI-P coating system. 100

Figure III.8-14. Calibration curve of the Berkovih indenter used in tests. It was performed on a fused silica sample. A constant value of hardness is remarkable from approximately 100 nm. 101

Figure III.8-15. Hardness continuously recorded from CSM test implemented on a bilayer Ni-P coating system performed up to a depth penetration of 2000 nm. 102

Figure III.8-16. Hardness computation from CSM tests and continuous multicycle test performed on a bilayer NI-P coating deposited on a steel plate. 102

Figure III.9-1. Hardness from multicycle indentation tests, described by the modified Jönsson and Hogmark ‘s model. 103

Figure III.9-2. Hardness modeling from multicycle indentation tests by the modified Jönsson and Hogmark ‘s model (sample 1020-I) 103

Figure III.9-3. Modified Jönsson and Hogmark ‘s model describing the hardness behavior of sample 1020-O from multicycle indentation tests. 104

Figure III.9-4. SEM micrograph illustrating the dimension of each single layer of the bilayer electroless Ni-P coating (sample named 1020-B). 105

Figure III.9-5. SEM images of sample labeled 1020-B showing the dimension of each layer of the bilayer electroless Ni-P coating. 106

Figure III.9-6. Contact Stiffness from multicycle indentation tests performed on a bilayer No-P coating system, described by the model presented in the Eqs. (III.3-6) through (III.3-11) 109

Figure III.9-7.Composite elastic modulus from multicycle indentation tests performed on a bilayer Ni-P coating system, predicted on the basis of the model presented in this section. 110

Table Index

Table I.8-1. Developed models to evaluate the contribution factor of film and substrate to composite modulus. 29
Table II.2-1. Film thickness from sprayed hydroxyapatite coatings 43
Table III.1-1. Elastic modulus computed from continuous multicycle indentation test from SAE 1020, SAE 1045, and SAE P20 carbon steel samples. 59
Table III.1-2. Hardness of carbon steel samples (mean values) described by the models of Li et Bradt [103] and Chicot [104] describing the indentation size effect from the continuous multicycle indentation test data. 62
Table III.1-3. Contact area functions advanced by Oliver and Pharr [1] and Chicot *et al*. [27]. 63
Table III.1-4. Elastic modulus and reduced elastic modulus of fused silica by replacing the models of contact area proposed by Oliver and Pharr [1] and Chicot et al. [27] into Eq. (III.1-3) between $100 < h\max < 1900$ nm. 68
Table III.1-5. Elastic modulus and reduced elastic modulus of fused silica by replacing the models of contact area proposed by Oliver and Pharr [1] and Chicot *et al.* [27] into Eq. (III.1-3) considering $4 < h\max < 50$ nm. 69
Table III.1-6. Elastic modulus and reduced elastic modulus of SAE 1020 by replacing the contact area models proposed by Oliver and Pharr [1] and Chicot et al. [27] into Eq. (III.1-3) 69
Table III.1-7. Elastic modulus and reduced elastic modulus of SAE 1045 using the contact area approches proposed by Oliver and Pharr [1] and Chicot et al. [27] into Eq. (III.1-3) 70
Table III.1-8. Elastic modulus and reduced elastic modulus of SAE P20 replacing the contact area functions proposed by Oliver and Pharr [20] and Chicot et al. [21] into Eq. (III.1-3) 70
Table III.2-1. Surface roughness and thickness of the sprayed Hydroxyapatite coating samples. 76
Table III.2-2. Hardness of porous and dense layer from the sprayed hydroxyapatite coatings. 80
Table III.2-3. Elastic moduli from the sprayed hydroxyapatite coatings. 82
Table III.2-4. Fitting parameters from the models describing the elastic modulus and hardness as function of the crystallinity volume fraction used ($\mathrm{X}Cr$) for all the SPPS-HAP coatings. 87
Table III.3-1. Elastic moduli and hardnesses of the sprayed coatings and of the substrates. 105
Table III.3-2. Reduced elastic modulus and fitting parameter values by applying the model proposed in this work. 110

Abstract

Title: Development of multicycle indentation to study solid, coated and heterogeneous materials.

Abstract: The assessment of mechanical properties of materials by instrumented indentation tests (IIT) have been widely performed in last years. The objective of this work is to develop a methodology to analyze the mechanical behavior of materials from the data obtained by a continuous multicycle indentation test at the microscale of loads so as to limit the problems associated with the heterogeneity of the materials and to increase the amount of data for the study of thick coatings that only nanoscale analysis does not provide in the case of heterogeneous coatings. To validate our approach, it was study the hardness and the elastic modulus of homogeneous bulk materials (carbon steels), heterogeneous dense coating (hydroxyapatite), and a two-layers coating material (Nickel-Phosphorus). The study of homogeneous bulk materials allowed us, first, to validate the methodology. It is also proposed a model to estimate the hardness and elastic modulus of hydroxyapatite coatings considering the compaction of the material during the indentation process. Second, it is proposed to associate the hardness and elastic modulus to the volume fraction of crystallinity. Finally, from the multicycle indentation tests performed on the electroless Ni-P bilayer coating, a new approach is advanced to assess the elastic modulus of each layer from the expression of the reciprocal of the experimental contact stiffness as function of the contact area originally proposed by Tricoteaux for a monolayer system, but now linked to a multilayer model based on the weight function suggested by Korsunsky.

Keywords: multicycle indentation test, mechanical properties, heterogeneous and coated materials.

Résumé

Titre : Développement de l'indentation multicyclique à l'étude des matériaux massifs, revêtus et hétérogènes.

Résumé : L'évaluation des propriétés mécaniques des matériaux par essais d'indentation instrumentée (IIT) a été largement étudiée ces dernières années. L'objectif de ce travail est de développer une méthodologie pour analyser le comportement mécanique des matériaux à partir des données obtenues par indentation multicyclique à une échelle microscopique de manière à limiter les problèmes liés à l'hétérogénéité des matériaux et à augmenter le nombre de données pour l'étude des revêtements épais que seule l'analyse nanométrique ne permet pas de fournir dans le cas de revêtements hétérogènes. Pour valider notre approche, nous étudions la dureté et le module d'élasticité de matériaux massifs homogènes (aciers au carbone), de revêtement épais hétérogène (hydroxyapatite), et de revêtement bicouche (Nickel-Phosphore). L'étude des matériaux massifs homogènes nous a permis, tout d'abord, de valider la méthodologie. Nous proposons également un modèle pour estimer la dureté et le module d'élasticité des revêtements d'hydroxyapatite en considérant la compaction du matériau pendant l'indentation. D'autre part, nous proposons de relier la dureté et le module d'élasticité à la fraction volumique de cristallinité. Enfin, à partir de l'indentation multicyclique effectuée sur le revêtement Ni-P bicouche, nous proposons un modèle pour évaluer le module d'élasticité de chaque couche à partir de l'expression de l'inverse de la raideur expérimentale de contact en fonction de l'aire de contact proposée initialement pour un monocouche par Tricoteaux que nous couplons également à une approche multicouche basée sur le modèle de Korsunsky.

Mots Clés : essais multicycliques, propriétés mécaniques, matériaux hétérogènes et revêtus

Nomenclature

a, contact radius between the indenter and surface during indentation

a_1, parameter of the proportional specimen resistance model

a_2, parameter of the proportional specimen resistance model

α, geometric correction factor of the contact area suggested by Bec *et al.*

α_1, fitting parameter from the Antunes *et al.*'s model

α_2, fitting parameter from the Doerner and Nix 's model

α_3, fitting parameter from the Menčík *et al.*'s model

α_4, fitting parameter from the second Menčík *et al.*'s model

A, theoretical contact area

A_{C}, projected contact area

A_{m}, true contact area

a_{F}, film volume fraction contributing with composite hardness or elastic modulus

a_{P}, volume fraction of the porous zone contributing with the composite hardness

β, geometric correction factor

B, geometric coefficient from the contact area function advanced by Troyon and Huang

C, compliance of the sample

C_{f}, frame compliance of the instrument

C_{i}, fitting parameters from the contact area function advanced by Oliver and Pharr ($i = 1, \cdots, 8$)

C_{T}, total compliance of the system

Δ, ratio of the final depth and the maximum indentation depth

$\mathit{\Delta}_{\mathrm{L-B}}$, Li and Bradt's parameter to quantify the indentation size effect

δ, indentation depth (h) to film thickness ratio (t)

d, indenter diagonal from a Vickers's impression

E, elastic modulus of sample

E_a, elastic modulus from the amorphous phase of the material

E_{Cr}, elastic modulus from the crystalline phase of the material

E_C, composite elastic modulus from a substrate-film system

E_F, elastic modulus of a film

E_{i}, elastic modulus of a diamond indenter

E_{R}, reduced modulus of the sample

E_{RF}, reduced modulus of the film on a coated material

E_{RC}, reduced composite modulus from film-substrate material

E_{RS}, reduced modulus of the substrate from a coated material

E_S, elastic modulus of a substrate

ε, geometric factor depending on the indenter shape

f_1, weight function from Antunes *et al.* 's model

f_2, weight function from Doerner and Nix's model

f_3, weight function from Menčík *et al.* 's model

f_4, weight function from the second model by Menčík *et al.*

f_n, weight function from the model by Korsunsky *et al.*

Φ, weight function from Gao *et al.*'s model

γ, correction factor depending on material proposed by Hay *et al.*

φ, parameter of the model advanced by Janzen

φ_1, factor contribution from phase 1 to the mechanical property of the material

φ_2, factor contribution from phase 2 to the mechanical property of the material

H, hardness of sample

H_0, macrohardness

H_a, amorphous phase hardness

H_C, composite hardness from a substrate-film system

H_{Cr}, crystalline phase hardness

H_{D}, hardness of densified layer coating

H_F, hardness of a film from a coated material

H_{LSF}, hardness length-scale factor

HIT, hardness from instrumented indentation test

HM, Martens hardness

HM_0, Martens macrohardness

H_{P}, hardness of porous layer coating

H_S, hardness of a substrate from a coated material

h, actual indentation depth

h_0, indentation depth corrected by the blunt defect of the indenter tip

h^*, characteristic scale-length which characterizes the indentation size effect

h_{b}, tip defect dimension

h_C, contact indentation depth

h_{f}, final indentation depth

h_{i}, translation in depth to replace the zero shift of the load from Chicot *et al.*'s model

h_{max}, maximum indentation depth

h_{meas}, indentation depth registered by the instrument

h_{T}, theoretical plastic penetration depth from Bec *et al.*'s model

λ, parameter from the models advanced by Hill, Budianski and Mossotti-Clausius

K, factor depending on material in the power law advanced by Oliver and Pharr

k_H, adjustable parameter from the Humbert *et al.*'s model

k_k, fitting parameter from the Korkunsky *et al.*'s model

k_{JH}, fitting parameter Jönsson and Hogmark's model

k_P, fitting parameter from Puchi-Cabrera's model

κ, fitting parameter from the model presented in this work

m, exponent depending on material in the power law advanced by Oliver and Pharr

m_p, exponent from advanced by Puchi-Cabrera's model

ψ, semi-angle of the conical indenter equivalent to a pyramidal one

P, load on sample

P_0, deviation load from Chicot *et al.* 's model

P_{max}, maximum load applied on sample

S, experimental contact stiffness

S_C, composite contact stiffness

S_S, contact stiffness from the substrate

S_{F}, contact stiffness from the film

t_F, thickness of the film

υ, Poisson's coefficient of the material specimen

υ_{i}, Poisson's coefficient of the diamond indenter

ξ, the semi-angle between the two opposite faces of a pyramidal indenter

χ, mixing parameter from Halpin–Tsai's model

X_{Cr}, crystallinity volume fraction

Y_1, mechanical property of phase 1 of a composite material

Y_2, mechanical property of phase 2 of a composite material

Y_C, mechanical property of a composite material

General Introduction

Instrumented indentation tests have been extensively implemented in the assessment of several mechanical properties of materials. Many difficulties have been overcome in the assessment of mechanical properties by using this technique. As result of the increasing interest in this field, the development of models to describe the variations of mechanical properties by instrumented indentation have been proposed in last decades. From microscale to nanoscale, and more recently ultra-nanoscale, these tests have been implemented to compute the mechanical response of bulk and coating materials to evaluate its application in different industrial fields. With the aim of contribute to this important field of the science the objective of this work is to develop a methodology to analyze and to interpret the data provided from a continuous multicycle indentation tests at the microscale of loads to overcome the difficulties inherent to the heterogeneities of materials or the thickness measurement of coated systems where the indentation tests at a nanoscale range of loads could not provide enough information to describe the variations of mechanical properties, *i.e.* hardness and elastic modulus, as function of an increasing loading or deeper displacement of the indenter. With this objective, this work has been divided in three chapters, the first one concerns the literature summary supporting the present developed research, the second indicates the materials and experiments executed into this investigation, and finally, the third chapter where the results of the applied methodology are shown and discussed according with the considered materials under analysis.

The chapter I is presented to the reader to establish the state of the art into the indentation field, this first chapter is dedicated to explain the basis of the data analysis acquired and recorded by the indentation instruments at microscale and nanoscale ranges. A review of relations between the applied load on sample and the displacements of the indenter into the surface obtained by the instrument is presented. Moreover, concerning the data treatment, the notion of the frame compliance is developed to take into account the deflection occurring into the specimen-instrument system. The load-displacement curve acquired by the instrumented indentation tests is presented and described. Additionally, the possible mechanical responses of the material surface beneath the indenter are expounded to be taken into account on the estimation of the contact area. Considering this contact area between the indenter and the specimen surface, one of the most important parameters to evaluate, some models to estimate it are explained and physically interpreted. Then, previous investigations to compute hardness and elastic modulus are detailed. The data treatment regarding the phenomena occurring throughout the indentation test are showed and explained. The continuous multicycle protocol and continuous stiffness measurement mode are presented to use them in the determination of mechanical properties from more complex systems and test settings such as film-substrate or heterogeneous systems.

The second chapter presents to the reader the material specimens and the characteristic of indentation experimentations developed in this research. Concerning the materials, three general sort are analyzed such as homogeneous, heterogeneous, and coated materials. The description of surface preparation or condition of samples surfaces is detailed to be after considered into the data analysis from the load-displacement curves. The general functionality of the instrument is explained and the differences between the two scales of measurement is point out. The presented experimental design is based on the available material specimens so as to evaluate their mechanical properties by submitting them to a continuous multicycle test at microscale range to estimate the influence of load-unload sequences into the mechanical response of the material.

Finally, in chapter III, the results and discussion are presented to the reader. With the aim to contribute to the progress of this important field a different methodology by using a continuous multicycle indentation test is developed and analyzed to be implemented in different sorts of materials, from homogenous to heterogeneous materials, and from bulk to coated materials. The results of the present work are divided in three parts: the first part stands for a homogenous material, in this case represented by the carbon steel samples; the second, by considering the analysis over heterogeneous materials exemplified by the hydroxyapatite coatings; and, the third one, which involves the analysis performed on film-substrate systems typified by Ni-P electroless coatings specimens. Along this chapter, the results are displayed and discussed to ponder the influence of the load-unloading sequences into the assessment of their mechanical properties, *i.e.* hardness and elastic modulus, when this samples are submitted to continuous multicycle tests. The analysis of the results commences for the carbon steel samples (first part) to be extend after to examine a heterogeneous material represented by the hydroxyapatite coatings samples (second part), and afterwards, to be implemented to bilayer Ni-P coatings specimens (third part). The acquired data is submitted to corrections due to the compliance frame of the instrument, blunt defect of the indenter tip, and the deformation of the material beneath the indenter governed by the Poisson's coefficient of the material. According with the existing background, the response of the material around the indenter is computed to describe the contact area between the indenter and the surface of the sample. The obtained data from carbon steel samples is computed to evaluate the comportment of the elastic modulus as function of the maximum indentation depth reaches at each cycle of the loading-unloading sequences. Afterwards, the second part pretends to ponder the methodology applied to heterogeneous materials, mechanical properties of solution precursor plasma sprayed hydroxyapatite (SPPS-HA) coatings are studied using the

© 2016 Tous droits réservés. lilliad.univ-lille.fr

continuous multicycle indentation test. The mechanical properties are determined by means of indentation experiments in the microscale range of loads to limit the influence of the heterogeneities of the microstructure as well as the roughness over the surface of the coating for which the effects are predominant at the nanoscale range of loads. The third part is developed with the aim of extend the analysis of multicycle indentation tests beyond bulk materials, and they are also implemented to a coated system. A bilayer Ni-P coating system is evaluated when it is submitted to CSM at a nanoindentation range and continuous multicycle indentation at a microindentation range. Physical models to study multilayer systems are applied to calculate the hardness and elastic modulus behavior of each layer from the electroless Ni-P coatings deposited on carbon steel plates.

It should be point out that this work has been developed as results of the continuous research in the instrumented indentation field which is sustained by previous publications in reviews and congress.

Publications at international reviews of Rank A:

1. Mejias A, Candidato RT, Chicot D, Pawlowski L. Mechanical properties by instrumented indentation of solution precursor plasma sprayed hydroxyapatite coatings: Analysis of microstructural effect, Surface and Coatings Technology, Volume 298, 25 July 2016, Pages 93-102
2. Benarioua Y, Mejias A, Roudet F, Iost A, Chicot D, Hardness-load modelling applied to multilayer galvanized coatings. Surface Engineering, Volume 32, Issue 3, Pages 194-200, 2016.
3. Nogning Kamta P, Mejias A, Roudet F, Louis G, Touzin M, Chicot D, Creep indentation analysis of T22 and T91 chromium based steels. Materials Science and engineering A, Volume 652, Pages 315-324, 15 January 2016.
4. Yetna Njock M, Chicot D, Ndjaka JM, Lesage J, Decoopman X, Roudet F, Mejias A. A criterion to identify sinking-in and piling-up in indentation of materials. International Journal of Mechanical Sciences, Volume 90, Pages 145-150, January 2015.

Publication at National review:

1. Yetna N'Jock M, Chicot D, Ndjaka JM, Lesage J, Decoopman X, Roudet F, Mejias A, A simple criterion to identify the deformation mode in indentation. Matériaux & Techniques, Volume 103, 603 - 8 pages, 2015

Congress communications:

1. Sokołowski P, Mejias A, Chicot D, Musalek R, Nylen P, Pawłowski L. The evaluation of mechanical properties of suspension plasma sprayed zirconia coatings having various

microstructures. International Thermal Spraying Conference and Exposition, ITSC 2016, Shanghai, China, (10-12 May 2016).

2. Mejias A, Chicot D, Decoopman X, Montagne A, Roudet F, Iost A. Multi-scale approach of the instrumented indentation technique on the fracture toughness estimation. Indentation 2014, 10-12 décembre 2014, INSTITUT CHARLES SADRON, Strasbourg -France.

Chapter I: LITERATURE SUMMARY

I.1. INTRODUCTION

By means of instrumented indentation tests (IIT) the mechanical properties of materials, such as elastic modulus [1, 2] , hardness [1, 3], fracture toughness [4, 5], among others can be assessed [6, 7, 8, 9]. The development of models to describe the mechanical behavior and variations of mechanical properties of materials have been studied in last decades [1, 2, 10, 11]. In order to establish the state of the art in this field, this first chapter is devoted to explain the basis of the analysis of the data acquired and recorded by microindentation and nanoindentation instruments. As it will be explained, the examination of the relation between loads and displacements obtained by the instrumented indentation tests is not so obvious, and the selection of the path to evaluate this data will depend of numerous variables and concerns, starting from the compliance of the specimen-instrument system passing through the examination of the mechanical response of the material surface beneath the indenter, until mechanical phenomena such as diffusion, porosity or microcracks present in the material. First all, the description of the load-displacement curve is carried out with the purpose of settle into the source of the data to be analyzed. The contact area between the indenter and the specimen surface, one of the most important parameters to evaluate, is defined and some of the models to estimate it are explained and physically interpreted. Immediately, the approaches advanced in earlier investigations to obtain the hardness and elastic modulus are explained. Afterwards, the improvements to take into account for the data treatment are explained in detail with the view to understand and consider all phenomena taking place in the surface of the sample during the course of the indentation test. To extent the evaluation of mechanical properties to complex systems and test settings, the continuous multicycle protocol and continuous stiffness measurement mode are described to use them in the determination of properties from film-substrate or heterogeneous systems by considering the phenomena occurring in the indentation test under this kind of condition. Among these phenomena, the concept of the indentation size effect is developed to realize that hardness value depends on multiples factors, and above all on the magnitude of loads applied on its computation. Additionally, models to calculate the contribution of every single layer or substrate from a multilayer coating system to the composite hardness or composite elastic modulus are carefully explained to be applied to multilayer coating systems.

I.2. THE LOAD-DISPLACEMENT CURVE

I.2.1. Classical instrumented indentation test

From instrumented indentation tests (IIT) mechanical properties of material, such as hardness and elastic modulus, can be assessed from small specimens using the experimental data acquired of loads and depths of penetration from tests [1, 2, 3]. From an overall point of view, a representative test consists in initiate an increasing loading on a material surface from zero to a maximum predefined force and then from the latest back to zero, as it is illustrated in Figure I.2-1.

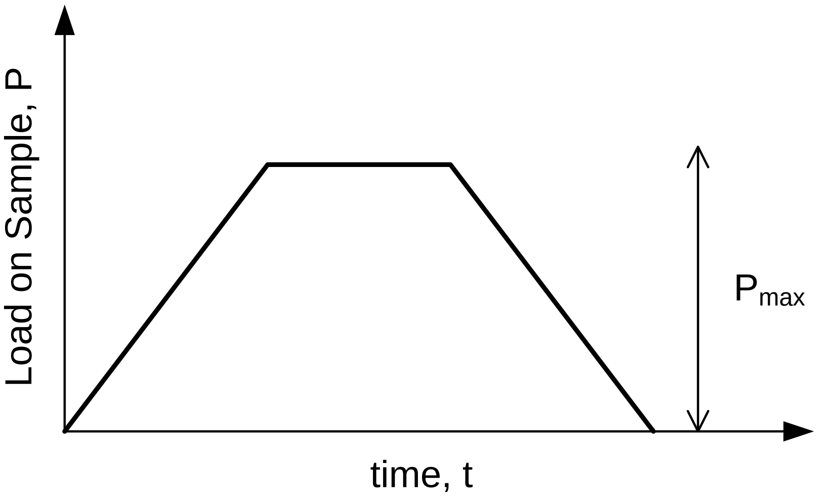

Figure I.2-1. Load-unload cycle from a standard instrumented indentation test.

Depending on the testing material a plastic deformation can take place and, at the time, a residual impression from the indenter is left into the surface of the specimen, for example, as it can be observed in Figure I.2-2. Using optical techniques, it is possible to estimate the size of the residual impression of the indenter, or, also called the projected contact area, marked by the indenter into the surface. However, well-knowing the geometry of the indenter and the maximum depth of penetration, it is possible to estimate the contact area between the indenter and the surface at the maximum load, from which the hardness of the material can be computed. Following with the experimentation enlightenment, afterwards the maximum load is applied on surface, immediately, the load on the indenter is withdrawn and the surface of the material tries to recover to its initial position but it is not usually allowed owing to the plastic deformation occurring in the course of the indentation test [12]. Considering the estimation of the elastic modulus of the material under study, normally, the initial portion of the unloading part of the curve is analyzed where a small portion of this elastic recovery is registered as a result of the relaxation of the elastic strain occurring within the material [12]. Figure

I.2-3 illustrates the profile of load-displacement curve obtained by a standard instrumented indentation test.

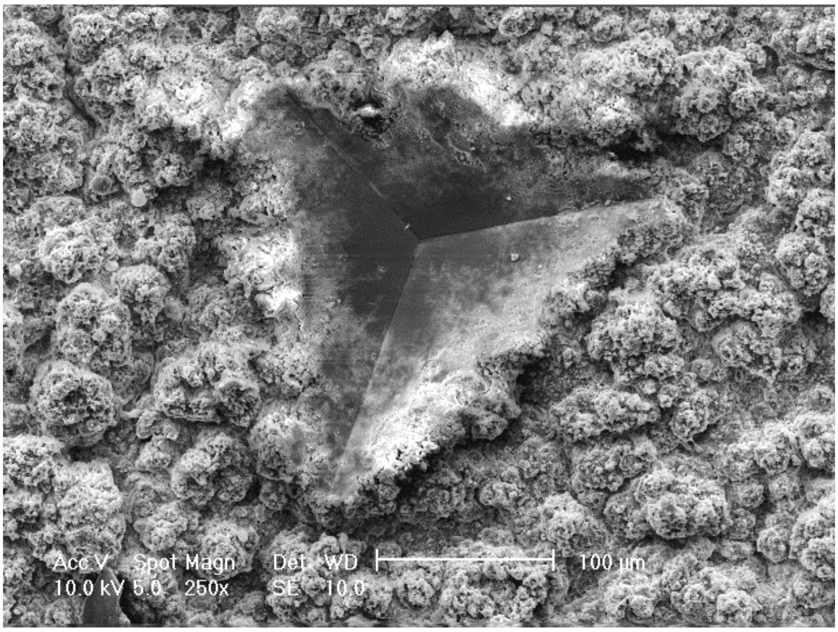

Figure I.2-2. SEM micrograph from the residual impression left by a Berkovich indenter on a hydroxyapatite coating sample.

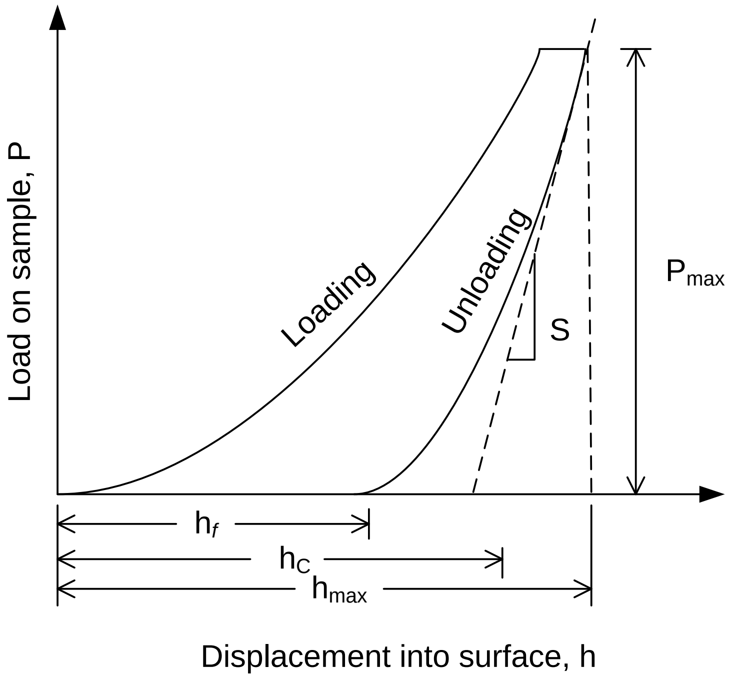

Figure I.2-3. Profile from load-displacement curve recorded from a standard instrumented indentation test.

In next sections, the methodology to analyze the data acquired by the instrumented indentation test to compute the elastic modulus and hardness will be explained taking into account and applying the corrections terms and factors to the experimental values obtained from these tests. It is important to realize that the methodology to be described ahead relies on the hypothesis that an elastic-plastic loading is followed by an elastic unloading with no plastic deformation taking place on the unloading part of the indentation process [12]. Normally, the reduced elastic modulus (E_R) estimated by indentation test is related directly proportional to the slope of the unloading curve at the maximum load, *i.e.* the slope at maximum indentation depth $\left(\frac{dP}{dh}\right)\Big|_{h=h_{\max}}$, and inversely proportional to the projected contact area (A_{C}), as it is expressed in the following relation:

$$E_R = \frac{1}{2}\frac{\sqrt{\pi}}{\sqrt{A_{\mathrm{C}}}}\left(\frac{dP}{dh}\right)\Big|_{h=h_{\max}} \tag{I.2-1}$$

Meanwhile, the hardness HIT (which stands for instrument hardness) can be assessed from the maximum indentation load ($P_{\max}$) divided by the projected contact area (A_{C}), mathematically denoted by:

$$HIT = \frac{P_{\max}}{A_{\mathrm{C}}} \tag{I.2-2}$$

Oliver and Pharr [1] proposed from Eq. (I.2-1) the evaluation of the reduced elastic modulus of a material calculated from the unloading part of the load-displacement curve rewriting it into the resulting equation:

$$E_{\mathrm{R}} = \frac{\sqrt{\pi}}{2}\frac{1}{\sqrt{A_{\mathrm{C}}}}\frac{1}{C} \tag{I.2-3}$$

Where the parameter C denotes the compliance of the sample to be examined. The reduced elastic modulus (E_{R}) comprises the elastic properties from the specimen and the indenter as function of their elastic moduli and Poisson's coefficients defined by:

$$\frac{1}{E_{\mathrm{R}}} = \frac{1-\upsilon^2}{E} + \frac{1-\upsilon_{\mathrm{i}}^2}{E_{\mathrm{i}}} \tag{I.2-4}$$

Where the elastic modulus for a diamond indenter (E_{i}) and the Poisson's coefficient (υ_{i}) are equal to 1140 GPa and 0.07, respectively [13]. The contact area (A_{C}) is then calculated as a function of the experimental indentation contact depth (h_{C}), and the geometric shape of the indenter, *e.g.* when a perfect Berkovich indenter is used, it can be expressed in the subsequent equation:

$$A_C = 24.5h_{\mathrm{C}}^2 \tag{I.2-5}$$

Where the experimental indentation contact depth (h_{C}) is evaluated as function of the maximum force applied ($P_{\max}$) on the surface, the maximal indentation depth ($h_{\max}$) and the experimental contact stiffness (S) as it showing next [1]:

$$h_c = h_{\max} - \varepsilon \frac{P_{\max}}{S} \tag{I.2-6}$$

The coefficient ε is a geometric factor depending on the geometric nature of the indenter. In the event that a flat punch indenter is used then $\varepsilon = 1$, for a conical indenter is utilized $\varepsilon = 0.72$ and if a spherical or paraboloid indenter is adopted for the study then $\varepsilon = 0.75$ instead [1]. The compliance factor (C) in Eq. (I.2-3) derives from the reciprocal of the experimental contact stiffness ($1/S$) determined from the slope of the upper portion of the unloading data at the maximum load from the load-displacement curve at the maximum indentation depth (illustrated in Figure I.2-3) as it is expressed in the next relation:

$$C = \frac{1}{S} = \left(\frac{dh}{dP}\right)\bigg|_{h=h_{\max}} \tag{I.2-7}$$

From the work realized by Oliver and Pharr [1], the unloading part of the curve can be modelled by means of a power law represented by:

$$P = K(h - h_{\mathrm{f}})^m \tag{I.2-8}$$

where K and m are material depending constants estimated by a regression of a least square analysis, and h_{f} is the residual or final indentation depth left by the indenter into the surface after the total withdrawal of the indenter.

For the fitting procedure corresponding to the unloading data from the load-displacement curve to the Eq. (I.2-8), only the data ranging between 40% and 98% of the maximum load is recommended to use in order to avoid possible incidence of the data at the unstable beginning of the unloading part at the maximum load and just before the unloading process be completed [1, 14]; according to this consideration, from Eqs. (I.2-7) and (I.2-8), it is possible to write the compliance factor as coming:

$$C = \frac{1}{S} = \frac{1}{mK\left(h_{\max} - h_f\right)^{m-1}} \tag{I.2-9}$$

By regarding the Eq. (I.2-3), the estimation of the reduced elastic modulus (E_{R}) relies on the accuracy of the definition and assessment of the projected contact area (A_C). The evaluation of this one will depend above all on the mechanical response of the surface around the indenter.

Some deviations from the classic load-unload test can be performed by instrumented indentation tests. In this way, partial unloadings, multicycle loading-unloading sequences, superimpose a harmonic frequency to the nominal value of the force, and change the dwell time at the maximum load can be set to study the behavior of the mechanical properties of the material. Moreover, the form of the load-displacement curve can indicate additional information about the phenomena related to the mechanical response of the material under indentation that permits the identification of non-linear occurrences such as cracking, chipping, delamination of films or phase transformations [12].

I.2.2. Multicycle protocol tests.

Concerning the instrumented indentation tests, there are many possibilities to study the mechanical behavior under different conditions. One of them, it is the possibility to establish a continuous multicycle protocol. In this case, the test involves sequences of loading and unloading into the surface of the sample. Normally, the increasing loading can be done continuously or by little increments as illustrated in Figure I.2-4. If the study implicates the measurement of changes in elastic modulus and hardness with the indentation depth, then partials unloading could be set contributing to the acquisition of the measurement of the contact stiffness ($\frac{dP}{dh} = S$) at one and all the cycles of the continuous multicycle test.

When the continuous multicycle protocol has to be defined, the instrument could be framed into load or depth control depending on the aim of the analysis. In the same way, the software controlling the instrument generally allows to customize the dwell time at each load increasing cycle at the maximum load preset. This period of holding at each cycle permits to become stable the couple instrument-sample before the unloading takes place. In other cases, the dwell time could be set with the purpose to measure creep within the material or the thermal drift of the instrument. The number of cycles, the load increase ($\Delta \mathrm{P}$), and the dwell time at the maximum and minimum load of every cycle could be defined by means of the indentation software. Additionally, in some instruments the acquirement of the stiffness of the contact, between the indenter and the surface, can be done superimposing a harmonic load signal that is added to the nominally increasing load [1, 12], and it is named as a continuous measurements of the contact stiffness.

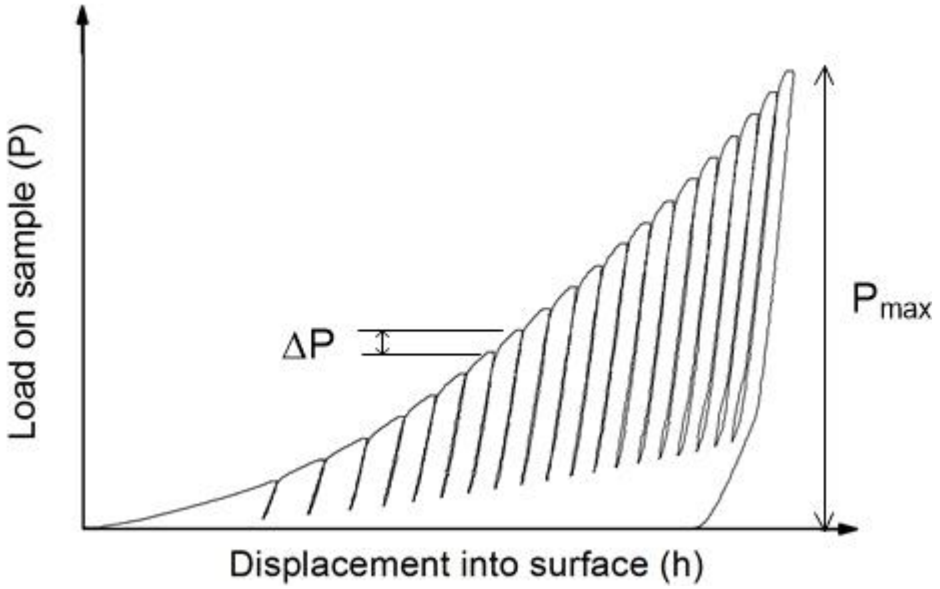

Figure I.2-4. Profile of the load-displacement curve from an indentation test running a multicycle procol.

I.2.3. Continuous stiffness measurement (CSM) test.

The continuous stiffness measurement (CSM) mode lets to measure the contact stiffness during the loading path of a standard indentation test. To achieve this objective, a harmonic load signal is superimposed and added to the nominally increasing load, as can be observed in Figure I.2-5. The displacement response of the indenter on the material at the excitation frequency and the phase angle between the two are measured continuously as a function of depth. Solving for the in-phase and out-of-phase portions of the response results in an explicit determination of the contact stiffness (S) as a continuous function of the depth [1, 15, 16].

Oliver and Pharr [1] showed that a continuous and immediate change in the contact stiffness throughout unloading its correlated to a change in the contact area, this affirmation was based on the fact that carrying out an indentation experiment using a Berkovich indenter over a sample of an electropolished tungsten at very low loads, *e.g.* 0.5 mN and less, it was shown that a purely elastic deformation occurred, it means, that the impression into the surface fully recovers afterward the complete unloading of the indenter, and furthermore, there was a superposition on the plot of the loading and unloading parts of the curves. Consequently, both contact area and contact stiffness were directly correlated and their increase or/and decrease were proportionally according to relationships that depend on the geometric shape of the indenter. As a primary conclusion of this fact, it was settle that changes in values of the stiffness of the contact are associated with variations in values of contact area when an instrumented indentation test is performed.

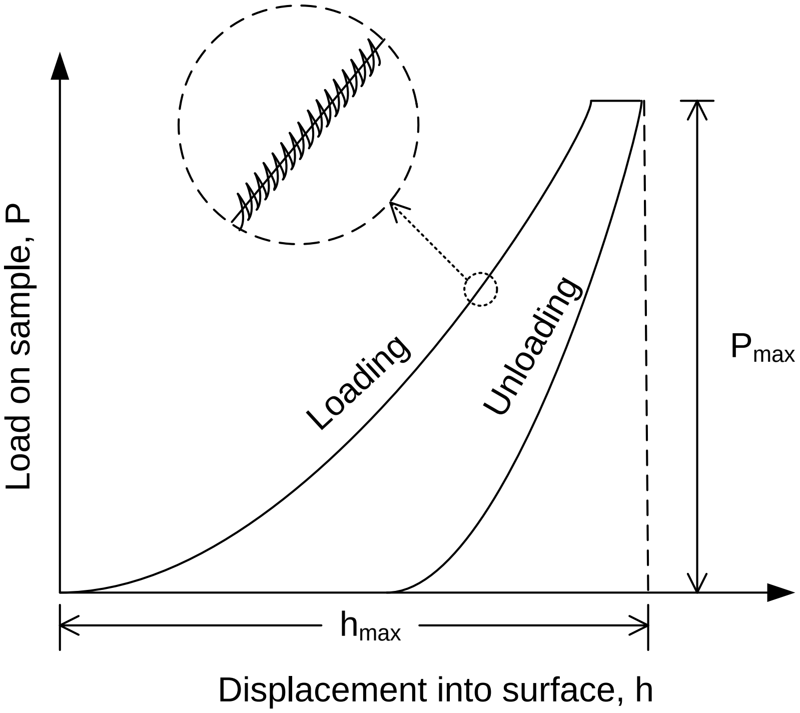

Figure I.2-5. Representative scheme of the continuous stiffness measurements (CSM) mode.

According with the Eqs. (I.2-1) a relationship between the contact stiffness and the indentation depth can be established for homogeneous and heterogeneous materials, if the non-uniformity of the material change with the depth. When a perfect Berkovich indenter is used, for example, the projected contact area (A_C) can be expressed as a function of the indentation contact depth (h_C) as it was shown in Eq. (I.2-5). By replacing Eqs. (I.2-5) and (I.2-7) into Eq. (I.2-1), it is obtained the subsequent relation:

$$S = 2\sqrt{\frac{24.5}{\pi}}E_R h_c \tag{I.2-10}$$

It can be concluded from Eq. (I.2-10), that for a homogeneous material with a constant elastic modulus (E), the reduced modulus (E_R) is also constant, and according with the Eq. (I.2-10) the contact stiffness (S) is directly proportional to the contact depth (h_C). For a heterogeneous material, if its elastic modulus (E) varies with the penetration depth, the reduced modulus (E_R) will vary with the indentation depth too, and consequently, there will not be a linear relation between the contact stiffness (S) and the contact indentation depth (h_C).

To calculate the projected contact area (A_C), it is necessary to estimate the value of the contact indentation depth (h_C) and to well-know the dimensions of the indenter. The value of h_C is computed by the analysis of the load-displacement curve, and this analysis takes into account the deformation of the material around the indenter and the blunt defect at the tip of the indenter as it will be detailed in the subsequent sections.

I.3. CONTACT AREA FUNCTION

I.3.1. Oliver and Pharr's contact area function [1]

Normally, the diamond indenters are not perfect pyramidal or conical solids, indeed a blunt at the indenter tip is present on them and this blunt defect must take it into account on the estimation of the contact area between the indenter and the material surface. The contact area function $A_C = \mathrm{f}(h_C)$ proposed by Oliver and Pharr [1, 17] is estimated using a function obtained from experimental contact depths (h_C) of several indentation tests at different loads with the intention to capture different residual impression sizes from the indenter. Then, the contact area function is described by the succeeding expression

$$A_C = C_0{h_c}^2 + C_1h_c + C_2{h_c}^{\frac{1}{2}} + \cdots + C_8{h_c}^{\frac{1}{128}} \qquad \text{(I.3-1)}$$

Where the coefficients C_1 trhough C_8 are constants to be determined by a non-linear regression analysis from the experimental data of the contact area (A_C) as a function of the indentation contact depth (h_C). Eq. (I.3-1) was suggested in the investigation carry out by their authors [1] owing to its ability to fit the data over the range of depths but not for any physical meaning of each term of the defined expression [17]. It was demonstrated that this function describes a large number of indenter geometries [17]. Regarding this contact area function, the first term is used to describe a perfect pyramidal or cone indenter only (*e.g.*, $C_0 = 24.5$ for a Berkovich indenter) and by using the first two terms could also define a hyperboloid of revolution, a tip-rounded cone or a pyramidal indenter with a vertical constant semi-angle at a large distance from the tip of the indenter [17] . Moreover, the last terms describe the deviations from a perfect shape above all due to the blunt defect of the indenter tip. Nevertheless, it must be careful about the data range where the contact area is defined, in others words, it is recommended to apply the function in the same range of contact depths used into the non-linear regression analysis, in order to avoid to extrapolate data due to such function may be highly inaccurate out of the experimental depth range set to fit the data to the Eq. (I.3-1).

On the other hand, some other researchers have proposed functions to model the contact area between the indenter and the surface of the sample, including fitting parameters with physical meanings [18, 19] as the indenter tip radius and the slope of the indenter equivalent cone. Among these functions, there are the ones developed by Gong *et al.* [20] and Troyon and Huang [21]. In these approaches, the distance between the ideal indenter shape and the rounded tip of the blunted indenter (h_{b}) is simply added to the measured indentation depth which will correspond to the corrected indentation depth.

I.3.2. Troyon et Huang's contact area description [21]

Troyon and Huang [22] demonstrated that the contact area function is not constant for a given material and an indenter type, however it depends on the size of the blunt defect (h_{b}) of the indenter tip and also on the deformation of the surface of the material around the indenter during the indentation test.

The description of the contact area as a function of the contact indentation depth (h_C), and taking into account the defect of the blunted indenter tip (h_{b}), is based on the assumption that the indenter can be model by a rigid cone with a vertical semi-angle ψ and a spherical cap of radius R, also described by others authors [20, 23, 24], as it is exhibit in Figure I.3-1.

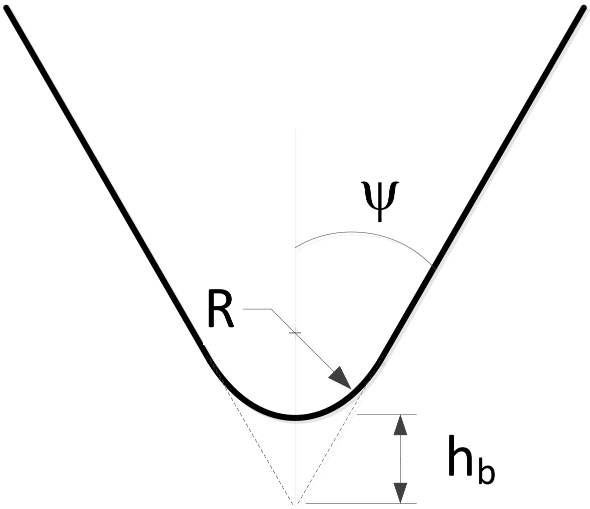

Figure I.3-1. Rigid cone with a vertical semi-angle ψ and a spherical cap of radius R modelling the blunt defect of the indenter tip.

Troyon and Huang proposed a contact area function defined by the next expression:

$$A_{\mathrm{C}} = \pi \tan^2(\psi)\,(h_{\mathrm{C}} + h_{\mathrm{b}})^2 = B(h_{\mathrm{C}} + h_{\mathrm{b}})^2 \tag{I.3-2}$$

Where B is a geometric factor equals to $\pi \tan^2(\psi)$, and h_b represents the blunt tip defect and its physical meaning has been illustrated in Figure I.3-1. This contact area function relies on the work previously developed of Shih *et al.* [25] who demonstrated that experimental data could fit very well the analytical expression of the cross-section area of the triangular-base pyramidal indenter trimmed with a spherical crown. Indeed, by means of a finite element analysis, was verified that an axisymmetric punch with a spherical cap and with a vertical semi-angle ψ giving the same cross-section area as the pyramidal indenter permits also to fit the experimental data. For the case of the Berkovich indenter, the contact area function proposed by Troyon and Huang [22] models it as a cone truncated by a sphere cap, as long as the indentation depth is larger than the depth at which the spherical crown touches the edge of the pyramid.

Based in the work of Troyon and Huang [21], Chicot *et al.* [26] by using a scanning electronic microscope at very high level of enlargement to visualize the indenter tip determined accurately the tip defect dimension h_b. As a consequence, the actual indentation depth (h_0) is calculated by adding the blunt tip defect to the measured depth given by the instrument as it follows:

$$h_0 = h_\mathrm{meas} + h_\mathrm{b} \tag{I.3-3}$$

where h_meas is the measured depth given by the instrument and h_0 stands for the displacement corrected by the defect of the indenter tip.

I.3.3. Chicot *et al.*'s contact area function [27]

In order to assess the contact area between the indenter and the specimen surface, Chicot *et al.* [27] proposed a model that permits to determine the contact area function related to the representative truncation length (h_b) of the indenter tip defect. The principal advantage of this model is that avoid the calibration procedure from the data obtained by indentation test in CSM mode (described in foregoing section) that is related to the estimation of some fitting parameters included in the contact area function proposed by Oliver and Pharr [1] and also for others authors as Hermann *et al.* [28, 29], Thurn and Cook [18], Troyon and Huang [21], Franco *et al.* [30], Bei *et al.* [31], and Antunes *et al.* [32].

Following the reasoning of the work advanced by Antunes *et al.* [32] and Berla *et al.* [19], the contact area function proposed by Chicot *et al.* [27] is given by:

$$A_\mathrm{C} = \left(\sqrt{\pi}\tan\psi\right)^2 \left[h_\mathrm{C} + h_\mathrm{b}\left(1 - \exp\left(-2\frac{h_\mathrm{C}}{h_\mathrm{b}}\right)\right)^{3/2}\right]^2 \tag{I.3-4}$$

Where ψ represents the effective vertical semi-angle of a conical indenter equivalent to a pyramidal one, h_C is the contact indentation depth and h_b is the effective truncation length or blunt defect of the indenter tip which can be determined by a non-linear regression analysis or with the assistance of microscopic observations.

According to the results obtained from the test over a fused silica sample to estimate the contact area, and afterwards tested on a TiHfCN thin film, the computation of the contact area and the mechanical properties of the thin film agreed with those obtained using Oliver and Pharr's contact area function (Eq. (I.3-1)), and even much better than applying other existing models, by employing merely the same indenter tip defect parameter (h_b). Furthermore, the authors advanced that the contact area can be easily calibrated for large-depth data, from CSM mode indentation tests and also in the range of microindentation tests, by neglecting the displacements lower than 200 nm, which overcomes the restraint of the range of contact depths. Nevertheless, for smallest depth, around less than 50 nm, the contact area function produces a deviation in the assessment of the elastic modulus nearby 5%, that was reported by the authors.

The analysis of the mechanical properties, *i.e.* hardness and elastic modulus, rests principally on the computation of the projected contact area A_C, however, the estimation of the properties will also depend on others physical phenomena related to the indentation process, and they must be taken into account to describe the mechanical response of the tested material.

I.4. DATA CORRECTION FROM INSTRUMENTED INDENTATION TESTS

I.4.1. Frame compliance of the instrument

Bearing in mind the Eq. (I.2-3), the compliance factor C of the sample is obtained from the expression $C_\mathrm{T} = C + C_\mathrm{f}$, where C_T is the total compliance and C_f is the frame compliance of the instrument. The assessment of the total compliance term, C_T, which is the reciprocal of the experimental contact stiffness ($1/S$), is determined from the slope of the unloading part of the load-displacement curve at the maximum indentation depth, as it was pointed out in the previous section in Eq. (I.2-9). To estimate the value of C_f, generally, well-known calibration samples are used. Nevertheless, the frame compliance of the instrument does not have a constant value, as it has been demonstrated by Chicot *et al.* [33] and Fischer-Cripps [14], this value depends on material and mounting system. With the aim of evaluate the frame compliance of the instrument, it has been proposed [1, 14, 33] that C_f should be calculated for each indentation test series from the graphic representation of the total compliance (C_T) versus the square root of the reciprocal contact area ($1/\sqrt{A_\mathrm{C}}$) related by the equation given below:

$$C_\mathrm{T} = C_\mathrm{f} + \frac{\sqrt{\pi}}{2E_\mathrm{R}}\sqrt{\frac{1}{A_\mathrm{C}}} \tag{I.4-1}$$

According to this equation, the relation between C_T and $\sqrt{1/A_C}$ should be normally linear as it is illustrated in Figure I.4-1, where the intercept of the plot with the axis of ordinates corresponds to the frame compliance of the instrument (C_f) and the reduced modulus (E_R) can be calculated from the slope term.

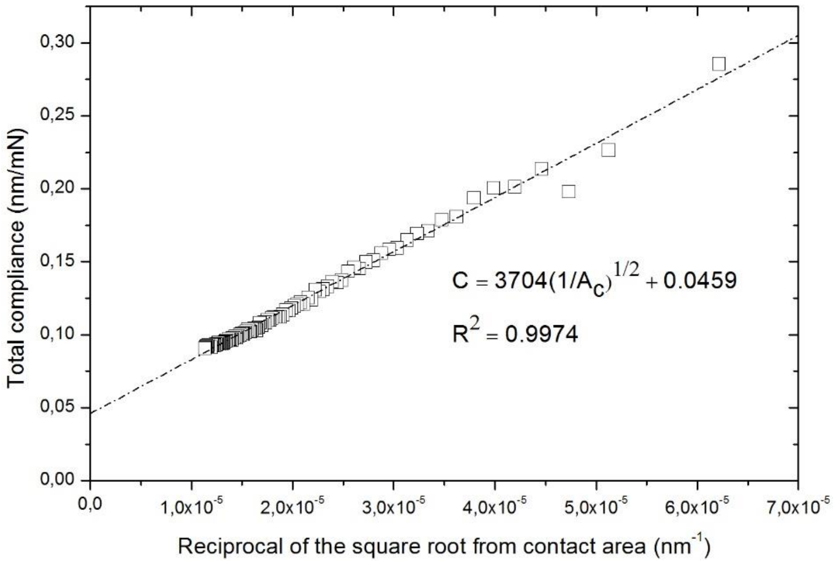

Figure I.4-1. Total compliance (C_T) versus the reciprocal of the square root of the contact area ($1/\sqrt{A_\mathrm{C}}$) from the data acquired by IIT over a carbon steel sample.

Regarding the indentation data depths obtained from the instrument, they should be corrected due to the elastic deflection of the instrument that occurs through the indentation test and, hereafter, the measured indentation depth has incorporated this deflection. The deflection can be generally characterized as a function of an applied load over a spring by modelling a linear relation between them [1]. Afterwards, to compute this correction, the product of the compliance term (C_f) deduce from

Eq. (I.4-1) and the load (P) is calculated. Lastly, the equation to express the corrected indentation depth (h) from the instrumented indentation tests can be written in the following form:

$$h = h_0 - C_{\mathrm{f}} \cdot P = h_{\mathrm{meas}} + h_{\mathrm{b}} - C_{\mathrm{f}} \cdot P \tag{I.4-2}$$

where the h_{meas} is the indentation depth registered by the instrument, C_{f} is the frame compliance term, P is the load applied on sample and h_{b} represents the blunt defect of the indenter tip. All correction factors and terms defined along this and in the succeeding section must be taken into account, to obtain a computation more refined of the mechanical properties to be estimated from the tested material samples.

I.4.2. Geometric correction factor

Regarding the fact that the elastic modulus is overestimated using Eq. (I.2-3), additionally, a geometric correction factor β is introduced into it by taking into account that the instrumented indentation tests are performed with non-axisymmetric indenters and comprising large plastic deformation owing to the pyramidal geometry of indenters [34, 17, 35, 36, 37]. Considering this approach, the Eq. (I.2-3) is rewritten as follows:

$$E_{\mathrm{R}} = \frac{1}{\beta} \frac{\sqrt{\pi}}{2} \frac{1}{\sqrt{A_{\mathrm{C}}}} \frac{1}{C} \tag{I.4-3}$$

Reviewing into the literature, several values have been proposed for the correction factor β. Oliver and Pharr [17] proposed values between 1.0226 and 1.085 for a Berkovich indenter. Moreover, according with the assumption of each one, King [38] proposed a value $\beta = 1.012$ for a Vickers indenter, while Dao *et al.* [39] suggested a value of 1.07, and others previous investigations that stated a value for indenters with circular geometries based on 2D simulations without considering the friction phenomenon [17, 35, 36, 37]. Lately, using a 3D simulation and considering the friction between the specimen and the indenter for a large number of materials with different elastic moduli and work hardening coefficients, Antunes *et al.* [34] demonstrated that a mean value of 1.05 can be replaced in Eq. (I.4-3) to estimate correctly the elastic modulus independently of the material to be inspected.

I.4.3. Material correction factor

In the same order and regarding the estimation of the contact area, Hay *et al.* [40] suggested a correction factor γ to explain the overestimation of the elastic modulus obtained by the Eq. (I.2-3) on the basis that the assumptions on the boundary conditions in Sneddon's solution ignored the radial displacement occurring into the material surface during the indentation process, assuming that the deformed surface within the region of contact between the indenter and surface has consequently the same shape of a rigid indenter, following this proposal Eq. (I.2-3) is rewritten below:

$$E_{\mathrm{R}} = \frac{1}{\beta\gamma}\frac{\sqrt{\pi}}{2}\frac{1}{\sqrt{A_{\mathrm{C}}}}\frac{1}{C} \tag{I.4-4}$$

Taking into account the correction factor γ proposed by Hay *et al.* [40] the profile of the deformed surface is considered slightly curved, differing from a perfect rigid cone, and it only depends on the material Poisson's ratio (υ). Figure I.4-2 shows the difference between the two considerations. When using a conical indenter, the correction factor γ suggested by Hay *et al.* is defined by:

$$\gamma = \pi\frac{\frac{\pi}{4} + 0.1548\cot(\psi)\frac{1-2\upsilon}{4(1-\upsilon)}}{\frac{\pi}{2} - 0.8312\cot(\psi)\frac{1-2\upsilon}{4(1-\upsilon)}} \tag{I.4-5}$$

where $\psi = 70.3°$ corresponds to the vertical semi-angle of a conical indenter with an equivalent area of a pyramidal one, *i.e.* $\pi\tan^2(\psi) = 4\tan^2(\xi)$, where ξ is the vertical semi-angle between the two opposite faces of a pyramidal indenter.

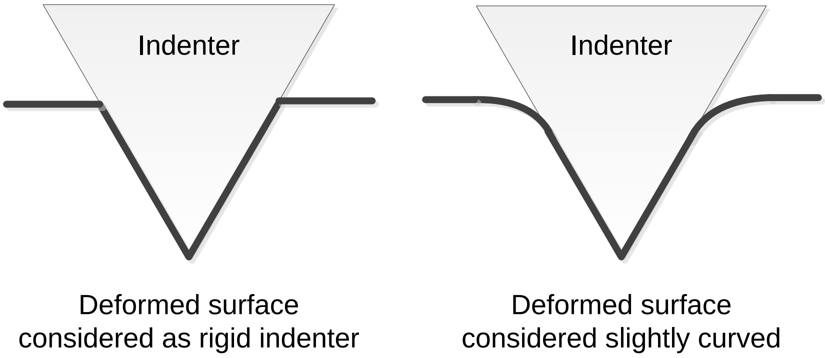
Indenter
Indenter
Deformed surface considered as rigid indenter
Deformed surface considered slightly curved

Figure I.4-2. Deformed surface considering it as the same that a rigid cone (left) or sligtly curved instead (right).

© 2016 Tous droits réservés. lilliad.univ-lille.fr

I.5. DEFORMATION MODE AROUND THE RESIDUAL IMPRESSION

The definition of the contact depth (h_C) will depend of the assumption of the behavior on the periphery of the indenter, *i.e.* phenomena of sink-in or pile-up. According to the methodology proposed by Oliver and Pharr [1] the suggested contact area describes a sink-in phenomenon on the residual impression of the indenter that can model the indentation imprint of a flat elastic half-space by rigid punches [17]. Nevertheless, when the pile-up phenomenon is present below the indenter in some elastic-plastic materials, the Oliver and Pharr’s model is not able to estimate the mechanical properties of the material, because in this case the influence of pile-up is neglected in the analysis and the computed contact area is underestimated, thus the elastic modulus and hardness could be overestimated. Figure I.5-1 illustrates the difference between the estimation on the indentation contact depth (h_C) considering the sink-in instead of the pile-up phenomenon, and consequently on the computation of the contact area between the indenter and the material surface.

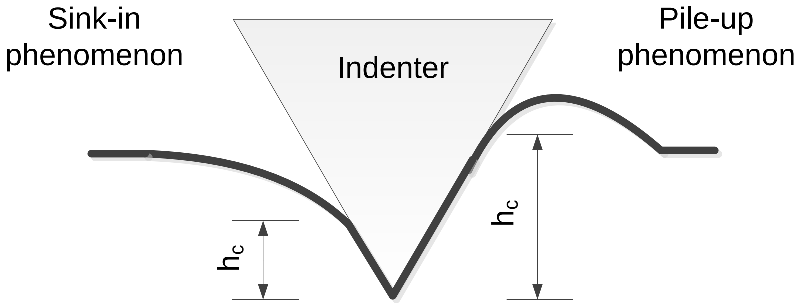

Figure I.5-1. Shematic representation of sink-in and pile-up phenomena around the indenter.

Considering the influence of pile-up occurring in some materials and also the blunting of the indenter tip, Bec *et al.* [11] proposed a method to estimate the actual contact area that takes into account the tip defect of the indenter and the plastic deformation around it. According with its reasoning, the theoretical contact area A is recalculated by a geometric correction factor α^2. In this way, the correction was applied by the authors to all depths considering the coefficient α as a constant, it means, that the coefficient remains constant in spite of the increasing of the plastic penetration depth. For a Berkovich indenter, the contact area A and its projection A_C are related to the theoretical plastic penetration depth, *i.e.* $A = 26{,}99{h_\mathrm{T}}^2$ and $A_C = 24{,}5{h_\mathrm{T}}^2$, in both cases h_T is defined as the theoretical plastic penetration depth, and it is obtained as the intersect to the axis of the abscises of the tangent to the upper unloading part at the maximum load of the load-displacement curve, expressed by the following expression:

$$h_{\mathrm{T}} = h_{\mathrm{max}} - \frac{P_{\mathrm{max}}}{S} \tag{I.5-1}$$

Based on topographic images obtained from a surface force instrument showing a plastic pile-up phenomenon around the indenter, and verifying that the true projected area was bigger than the theoretical or geometric area, the coefficient α was proposed to model the increase of the contact area owing this physical phenomenon. Considering this proposal, when pile-up phenomenon is present on the material the projected contact area between a perfect Berkovich indenter and the material is expressed by:

$$A_{\mathrm{C}} = 24.5\alpha^2(h_{\mathrm{T}} + h_{\mathrm{b}})^2 \tag{I.5-2}$$

Where h_{b} represents the dimension of the tip defect. According to Bec *et al.* [11] the value of the constant α equals to 1.2. This correction factor of the contact area allows to consider the pile-up effect and thus improve the estimation of the projected contact area to avoid the overestimation of mechanical properties, *i.e.* hardness and elastic modulus of materials. Depending on the range of measurements the tip round defect have a significant influence in the calculation of the contact area, above all for the smaller indentation depths.

Accordingly, Yetna *et al.* [41] proposed a criterion defined as the ratio of residual indentation depth to the maximum indentation depth at maximum load, which is able to identify the mode of deformation around the indenter. Based on the work realized by Giannakopoulos and Suresh [42], Yetna *et al.*'s approach defines the parameter Δ as the ratio of the final indentation depth (h_{f}) to the corrected maximum indentation depth (h_{max}) ratio calculated using Eq. (I.4-2), as it follows:

$$\Delta = \frac{h_{\mathrm{f}}}{h_{\mathrm{max}}} \tag{I.5-3}$$

where h_{f} is one of the fitting parameters obtained from the Eq. (I.2-8):

$$P = K(h - h_{\mathrm{f}})^m$$

After testing several types of materials apparently with pile-up and sink-in phenomena using Vickers and Berkovich indenters, it was concluded that for materials for which this ratio Δ was higher than 0.83 the pile-up phenomenon prevailed while it was the presence of sink-in more important when this ratio was lower than 0.83. The criterion Δ was proposed with the aim of identify the deformation mode of

© 2016 Tous droits réservés. lilliad.univ-lille.fr

the material beneath the indenter, *i.e.* sink-in or pile-up phenomenon, without any other additional observation techniques or measurements than the indentation data from the instrumented indentation tests.

I.6. INDENTATION SIZE EFFECT

When indentation tests are analyzed, it is well-known that computed hardness values will depend on the applied load (it means that hardness increases or decreases as a function of the load), it could be independent of the load or it could present complex fluctuations as function of the applied loads [3]. The description of hardness as function of the load scale has been studied for more than one hundred years, and a lot of relationships have been proposed to represent this load dependency of hardness. The influence of the charge is noticeable above all when low loads are applied on surface layers with different material properties between them. Nevertheless, as soon as the indentation depth increases on coating samples, the substrate dominates the hardness response and eventually there will not be change in hardness values when load increases. The load dependency of microhardness is known as the Indentation Size Effect (ISE). Cheng and Cheng [43] have discussed this phenomenon relating it with several causes such as work hardening, roughness, pile-up or sink-in phenomena, shape of the indenter, surface energy, dissimilarities in composition and crystal anisotropy. Among the models describing the indentation size effect (ISE), the Li and Bradt's model [44] and Nix and Gao's [45] model are probably the most applied ones.

I.6.1. Li and Bradt's Model [44]

According to the literature relative to microhardness values [44, 46, 47, 48, 49], it can be stated that the indentation size effect could be described commencing the modeling of the loading part of the load-displacement curve by the next relation between the applied load and the diagonal of the indent when a Vickers indenter is implemented:

$$P = a_1 d + a_2 d^2 \tag{I.6-1}$$

This mathematical model outlines the load as a function of the diagonal of the impression of a Vickers indenter. In Eq. (I.6-1) the constant a_1 symbolizes the load dependence of hardness. Previous investigations attributed the term $a_1 d$ to the specimen surface energy, the deformed surface layer, and indenter edges acting as plastic hinges [48, 49, 50, 51]. The Proportional Specimen Resistance (PSR) model developed by Li and Bradt [44] relates the constants a_1 and a_2 of Eq. (I.6-1) to the elastic and plastic properties of the material, respectively. Indeed, they submitted that constant a_1 is a composition of the elastic resistances of the sample and the friction resistance occurring in the interface indenter-specimen. By rearranging Eq. (I.6-1) in the following form:

$$\frac{P}{d} = a_1 + a_2 d \tag{I.6-2}$$

Allows to estimate the values of the constants a_1 and a_2 from the plot of $\frac{P}{d}$ versus d. Sangwal *et al.* [52] additionally demonstrated a linear relationship between a_1 and a_2, particularly, for some cobalt-based alloys specimens, but this depends on the nature of the material.

Based in the Proportional Specimen Resistance (PSR) model suggested by Li and Bradt [44], the model proposed by Sheng *et al.* [53] attempts to separate the influence of the roughness of the indentation size effect. According with this suggestion, the applied load is written as a function of the indentation depth according to the polynomial representing the Proportional Specimen Resistance (PSR) model defined by:

$$P = C_0 h + C_1 h^2 \tag{I.6-3}$$

Where the two constant C_0 and C_1 depend on the material properties and h represents the indentation depth. From this polynomial, the corresponding plot of $\frac{P}{h}$ versus h must be characterized by a straight line, where C_0 is the intercept with the axis of ordinate and C_1 is its slope.

Alternatively, the Martens Hardness (HM) according to its definition can be written as it is indicated below:

$$HM = \frac{P_{\mathrm{m}}}{26.43 {h_{\mathrm{m}}}^2} \tag{I.6-4}$$

Afterwards, by taking into account the Eq. (I.6-3), this expression can be defined as a function of two constants, C_0 and C_1, as it follows:

$$HM = HM_0 + \frac{\Delta_{\mathrm{L-B}}}{h} \tag{I.6-5}$$

© 2016 Tous droits réservés. lilliad.univ-lille.fr

where HM_0 is called the Martens macrohardness, and its equals to $C_1/26.43$ and, $\varDelta_{\mathrm{L-B}}$ quantifies the indentation size effect and can be assessed as the ratio $C_0/26.43$, relating the proportional specimen resistance to the Martens hardness defined to describe the hardness by means of the instrumented indentation tests.

I.6.2. Nix and Gao's Model [45]

Conversely, to explain the indentation size effect, Ma and Clarke [46] and Nix and Gao [45] introduced the Strain Gradient Plasticity (SGP) concept based on Taylor's dislocation theory [54]. Furthermore, the Geometrically Necessary Dislocations (GND) concept suggested by Nix and Gao [45] models accurately the ISE behavior of crystalline materials according with the experimental law needed to advance a mechanism-based theory of the Strain Gradient Plasticity (SGP). Lam and Chong [55] following a similar reasoning, using a glassy polymer, modelled hardness-depth dependency using the SGP theory, differing from the one of Nix and Gao [45] in how the dislocations of the global plastic deformation process were separated. A similar relation to estimate a material length-scale using microhardness experimentations was proposed by Abu Al-Rub and Voyiadjis [56]. The advanced relationship relating microindentation hardness, indentation depth, macrohardness and length-scale parameters involves the assessment of an exponent linked to the model, which varies between 1 and 2 correspondingly to the suggested relations submitted by Lam and Chong [55] and Nix and Gao [45], respectively.

Concerning the models developed to described the ISE, the model proposed by Nix and Gao [45] based on the Geometrically Necessary Dislocations underneath of the sharp indenter is well-known and widely employed to describe the behavior of microindentation hardness data. This relation advanced by Nix and Gao between the macroindentation hardness, denoted by H_0, the microindentation hardness, noted by H, and the indentation depth, represented by h, is expressed below:

$$\left(\frac{H}{H_0}\right)^2 = 1 + \left(\frac{h^*}{h}\right) \qquad \text{(I.6-6)}$$

where H_0 is, generally, called the macrohardness and corresponds to the hardness that would arise from the statistically stored dislocations alone, in absence of any Geometrically Necessary Dislocations. The displacement, h^*, is the characteristic scale-length which describes the depth dependency of the hardness.

Based on the Geometrically Necessary Dislocations beneath a sharp indenter and following the same reasoning of the work developed by Nix and Gao [45], in the approach suggested by Chicot [10], it was demonstrated that the Strain Gradient Plasticity (SGP) theory represented well the nano and microindentation hardness data if the uniformity of the dislocation distance is taken into account. Description of the plastic deformation process can be given by the parameter entitled as the hardness length-scale factor (H_{LSF}) equals to $H_0 \cdot \sqrt{h^*}$, where H_0 is the macrohardness and h^* the characteristic scale-displacement deduced from the hardness-depth relation of the Strain Gradient Plasticity theory showed in Eq. (I.6-6). Theoretically, the H_{LSF} factor is proportional to both shear modulus and Burger's vector, depending on the dislocation distance. In order to agree the results obtained in the two scales of measurement, *i.e.* nano and microindentation, the hardness length-scale factor (H_{LSF}) suggested by Chicot [10], corresponds to the square root of the slope of the straight line resulting when the square of the nano or microhardness is plotted versus the reciprocal of the indentation depth, where both are related as it follows:

$$H^2 = H_0^2 + \frac{{H_{LSF}}^2}{h} \qquad \text{(I.6-7)}$$

where H_0 is the macrohardness, H_{LSF} is the hardness length-scale factor, H is the nano or microhardness, and h represents the indentation depth. The value of H_{LSF} provides a description of the plastic deformation resistance of the material analyzed.

On the other hand, the Strain Gradient Plasticity (SGP) model of the Nix and Gao's proposal [45] to analyze the indentation size effect, is extended by Chicot [10] who suggested that the Martens hardness (HM) could be written as function of indentation depth (h) by the following expression:

$$HM^2 = {HM_0}^2 + \frac{{H_{LSF}}^2}{h} \qquad \text{(I.6-8)}$$

where H_{LSF} is the same hardness length-scale factor already defined by Chicot [10].

It is important to point out that the hardness length-scale factor (H_{LSF}) is noted in MPa·m$^{1/2}$, and it is comparable to toughness. Regarding the surroundings where the analysis relies on, it could be interpreted as the plastic deformation resistance to the indentation process. In order to estimate the parameters mentioned earlier in Eq.(I.6-8), the experimental data obtained from the loading curve can be used. Based in the previous works of Bucaille *et al.* [57] and Cao *et al.* [58], Chicot *et al.* [59]

proposed a mathematical model to describe the load-displacement curve from experimentations of massive material defined in the following expression:

$$P = P_0 + 26.43\left({HM_0}^2 + \frac{{H_{LSF}}^2}{h}\right)^{1/2} h^2 \tag{I.6-9}$$

Where P_0 denotes the deviation load, HM_0 describes the dynamic Martens macrohardness and H_{LSF} represents the indention size effect of the material. More recently, Chicot *et al.* [60] proposed a model to circumvent the influence of roughness and porosity on the hardness at low loads, and by readjusting Eq. (I.6-9) as it follows:

$$P = 26.43\left({HM_0}^2 + \frac{{H_{LSF}}^2}{h - h_{\mathrm{i}}}\right)^{1/2} (h - h_{\mathrm{i}})^2 \tag{I.6-10}$$

Where a translation in depth (h_{i}) has been introduced to replace the zero shift of the load (P_0). This model was applied on yttria-stabilized zirconia coatings, and the authors demonstrated that the macrohardness value found was the same by applying the Proportional Specimen Resistance (PSR) model or the Strain Gradient of Plasticity (SGP) model [60]. Nevertheless, the parameter related with the indentation size effect could not be represented accurately as a consequence of the influence of roughness on the indentation tests.

I.7. ANALYSIS OF HETEROGENEOUS MATERIALS

Nowadays various engineering materials are widely used owing to their geometrical and microstructural configuration including presence of different phases, roughness profile, thickness or porosity which could be present in these bulk or coating materials. Indeed, it should be stated that presence of these characteristics influence considerably the mechanical properties of the material under analysis.

For studying the mechanical properties of such as materials, instrumented indentation tests could be performed at macro, micro or nanoscales. Nevertheless, when macroindentation is employed the heterogeneities of the material are no so obvious in the analysis of the acquired data due to that the heterogeneous material beneath the indenter behave as a homogeneous one considering the magnitude of the applied loads. On the other hand, if nanoindentation is used as an alternative to characterize heterogeneous materials some difficulties must be initially overcome owing to the evidence of high roughness and/or porosity on the surface of the material.

When discussing about heterogeneities of materials, for example, the presences of pores into this one, it is possible to affirm that a large dispersion on the indentation data should be expected in the analysis of results. Considering the appearance of the load-displacement curve, there is no doubt that it will depend of the relative position of the pores in the path of the displacement of the indenter, it means, if the porous milieu is on the top of the surface then the values of hardness will be lower than if the pores are at the bottom of the path of the indenter during the indentation test, which leads to be careful in the interpretation of the data acquired.

Other interesting aspect that could arise is the condition of the surface of the studied material. Normally, instrumented indentation tests are performed on samples that have been polished until obtain a like mirror surface, nevertheless, it is certain that when this procedure is accomplished in advance to indentation tests, it could produce modifications on the original state of the material like alterations of the residual stress state, filling or plugins pores or even nucleation of cracks and work-hardening on the surface that could modify the load-displacement curve and subsequently the computed values of the mechanical properties.

It is important to mention that hardness values obtained by means of the load-displacement curve analysis could increase or decrease with respect to the variation of the microstructure through the thickness of the material and/or the nucleation of cracks, the densification or compression of porous zones, or by the collapsed voids in the surrounding of the indenter. The different microstructures that can be present in a material can led to composite zones due to the existence of hard phases mixed with soft phases.

Some investigations [12, 60] have demonstrated the influence of defects located in the vicinity of the indenter on the estimation of mechanical properties. Thus, the presence of any kinds of defect beneath the indenter lead to a different profiles in the load-displacement curves that traduce them in different computed values of hardness or elastic modulus, for example, if the harder phase is in the beginning of the displacement of the indenter then the apparent hardness value determined by the standard load-displacement curve analysis will be greater than if the soft phase is in the outer surface of the material. Accordingly, the behavior of hardness values as function of displacement should be analyzed, and it should not be interpreted as a single number but a value related with the heterogeneities of the material correlated with the displacement of the indenter.

Depending on the behavior of the hardness or the elastic modulus as function of indentation depths, a lower bound (linear mixture law) and an upper bound (harmonic mixture law) proposed by Reuss and Voigt, respectively, could allow to delimit the experimental values. With the aim of describe the elastic modulus or hardness as a function of the depth, a macroscopic model can be defined from the point of view of the mechanical coupling, setting a physical meaning for the adjustable parameter for the system. The general expression of a linear mixture law is expressed in Eq. (I.7-1) and a harmonic mixture law in Eq. (I.7-2):

$$Y_C = \varphi_1 Y_1 + \varphi_2 Y_2 \tag{I.7-1}$$

$$\frac{1}{Y_C} = \frac{\varphi_1}{Y_1} + \frac{\varphi_2}{Y_2} \tag{I.7-2}$$

Where Y_C is the composite property, Y_n represents the property of material ($n = 1{,}2$), φ_1 and φ_2 stand for the contribution factor to the composite mechanical property from phase 1 and 2, respectively, by considering that $\varphi_1 + \varphi_2 = 1$.

The models revised until now to analyze the data from the load-displacement curve show all the consideration to take into account in the evaluation of the elastic modulus and hardness, if a bulk material is under study. Nonetheless, if a coated material is examined, others physical models have to be applied to inspect the contribution of every single part of the system, *i.e.* coating layers and substrate, to the total composite hardness or elastic modulus values obtained in the assessment of mechanical properties.

I.8. ANALYSIS OF FILM-SUBSTRATE SYSTEMS

I.8.1. Elastic modulus from thin films

When considering a coating system, *i.e.* a substrate coated with a film, it can be held that the computation of the hardness and elastic modulus is a function of the applied load on sample. Normally, it is noted that for lower loads, the influence on the deformation of the substrate is slight and the film-substrate system performs more like the film, whereas for higher loads the system responds as the substrate instead. By studying a film-substrate system, the computed composite modulus (E_C) will be located between two limits according as the indentation depth increases, *i.e.* the elastic modulus of the film (E_F), for the lower loads, and the elastic modulus of the substrate (E_S), for higher loads. Recent investigations [2, 61, 62, 63] developed mathematical models to differentiate the contributions of the elastic modulus of substrate (E_{S}) from the elastic modulus of the film (E_{F}) to the composite elastic modulus (E_{C}).

The relation proposed by different authors are collected in the Table I.8-1. To express the composite modulus these equations are based on the contribution of the elastic modulus of the film and the substrate, in a series or parallel model, as a function of the indentation depth (h), film thickness (t_{F}) and the corresponding empirical parameters. In the considered models, it is important to highlight that the computation of the composite elastic modulus (E_{C}) is done without considering any modification of the frame compliance of the instrument, and this is a very important parameter to take into account in order to analyze correctly the results. The approaches advanced by Antunes *et al.* [2] (Eq. (I.8-1)), Menčík *et al.* [62] (Eq.(I.8-3)), and Gao *et al.* [63] are in the basis of a linear mixture law, whereas the proposal suggested by Doerner and Nix [61], Menčík *et al.* [62] (Eq. (I.8-4)) and Antunes *et al.* [2] (Eq. (I.8-6)) are constructed from a harmonic mixture law, where the expression denoted by f_n ($n = 1, \cdots, 4$) represents the corresponding weight function to estimate the volume fraction of film and substrate contributing with the composite elastic modulus.

Table I.8-1. Developed models to evaluate the contribution factor of film and substrate to composite modulus.

$\left\|\frac{E_{\mathrm{C}}-E_{\mathrm{F}}}{E_{\mathrm{S}}-E_{\mathrm{F}}}\right\| = f_1 = \exp\left(-\alpha_1 \frac{t_{\mathrm{F}}}{h}\right)$ (I.8-1) Antunes *et al.* [2]	$\left\|\frac{\frac{1}{E_{\mathrm{C}}}-\frac{1}{E_{\mathrm{F}}}}{\frac{1}{E_{\mathrm{S}}}-\frac{1}{E_{\mathrm{F}}}}\right\| = f_2 = \exp\left(-\alpha_2 \frac{t_{\mathrm{F}}}{h}\right)$ (I.8-2) Doerner and Nix [61]
$\left\|\frac{E_{\mathrm{C}}-E_{\mathrm{S}}}{E_{\mathrm{F}}-E_{\mathrm{S}}}\right\| = f_3 = \exp\left(-\alpha_3 \frac{h}{t_{\mathrm{F}}}\right)$ (I.8-3) Menčík *et al.* [62]	$\left\|\frac{\frac{1}{E_{\mathrm{C}}}-\frac{1}{E_{\mathrm{S}}}}{\frac{1}{E_{\mathrm{F}}}-\frac{1}{E_{\mathrm{S}}}}\right\| = f_4 = \exp\left(-\alpha_4 \frac{h}{t_{\mathrm{F}}}\right)$ (I.8-4) Menčík *et al.* [62]
$\left\|\frac{E_{\mathrm{C}}-E_{\mathrm{S}}}{E_{\mathrm{F}}-E_{\mathrm{S}}}\right\| = \Phi$ (I.8-5) Gao *et al.* [63]	$\left\|\frac{\frac{1}{E_{\mathrm{C}}}-\frac{1}{E_{\mathrm{S}}}}{\frac{1}{E_{\mathrm{F}}}-\frac{1}{E_{\mathrm{S}}}}\right\| = \Phi$ (I.8-6) Antunes *et al.* [2]

Above in Table I.8-1, Φ is the weight function coming from the Gao *et al.*'s model [63] and it is defined as it follows:

$$\Phi = \frac{2}{\pi}\arctan\left(\frac{t}{a}\right) + \frac{1}{2\pi(1-\upsilon)}\left[(1-2\upsilon)\frac{t}{a}\mathrm{Ln}\left(1+\left(\frac{a}{t}\right)^2\right) - \frac{\frac{a}{t}}{1+\left(\frac{a}{t}\right)^2}\right] \tag{I.8-7}$$

where $a = h\tan(\psi)$, is the contact radius of an equivalent conical indenter at the maximum load and $\psi = 70.3°$, corresponding to the vertical semi-angle of the conical indenter.

I.8.2. Hardness from thin films

Evaluation of hardness values of a film-substrate system by monotonic instrumented indentation tests is not so obvious. On the one hand, by using nanoindentation tests it would be possible to obtain the data to compute only the hardness behavior of the film owing to the limited indentation depth reached by this type of instrument. On the other hand, as well as the indenter reach profounder depths performing microindentation tests, the data acquired is a response involving the contribution of the film hardness and the hardness variation taking place within the film and substrate surroundings. Based on these hypotheses, the models developed to analyze film hardness have to be carried out very carefully, in order to be able to analyze correctly the acquired data, principally due to the assumption that substrate hardness is independent of the indentation depth. Models to characterize multilayer coatings could be used too to improve the analysis and interpretation of these results.

The assessment of the hardness profile from a coated material should take into account the change in hardness as function of indentation depth owing to the existence of diffusion or porous layers, for example. Following this reasoning, a model to evaluate the hardness behavior from the multicycle load-displacement curve using the instrumented indentation at the microscale range could be established.

The advanced models to study the contribution of the film to the hardness measurement have been developed base on different approaches [64, 65, 66, 67]. Jönsson and Hogmark [67] proposed from a geometric area consideration that the film volume fraction (a_{F}) could be expressed as a function of the indentation depth (h) – originally depending on the diagonal of a Vickers indenter (d) –, the coating thickness (t_{F}) and a constant (k_{JH}) linked to the indentation behavior of coating material and the indenter geometry [67]:

$$a_{\mathrm{F}} = 2\frac{k_{\mathrm{JH}}t_{\mathrm{F}}}{h} - \frac{{k_{\mathrm{JH}}}^2 t_{\mathrm{F}}^2}{h^2} = 1 - \left(1 - \frac{k_{\mathrm{JH}}t_{\mathrm{F}}}{h}\right)^2 \tag{I.8-8}$$

When the indentation test is performed by using a Vickers indenter, the displacement of the indenter into surface can be directly connected to the indenter diagonal (d) based on simple geometrical considerations of the Vickers indenter tip angles, *i.e.* $h = d/7$. Additionally, for a Vickers indenter, the value of k_{JH} equals to 0.0728 when the coating fractures, whereas k_{JH} equals 0.1403 when the coating deforms plastically. When using a Berkovich indenter instead, according with the indenter geometry the value of k_{JH} is 0.0915 if the coating goes to fracture, whereas k_{JH} is 0.1746 if the coating deforms plastically.

Alternately, the proposal suggested by Korsunsky *et al.* [64] is based on the indentation work related to the deformation energy of the two materials and involving its interface beneath the indenter, that it was expressed in a relation to describe the composite hardness as the sum of the contribution of the film and substrate hardness as follows:

$$H_{\mathrm{C}} = H_{\mathrm{S}} + \frac{H_{\mathrm{F}} - H_{\mathrm{S}}}{1 + k_k \delta^2} \tag{I.8-9}$$

where H_{S} is the substrate hardness and H_{F} is the film hardness. The parameter δ denotes the relative indentation depth defined as the indentation depth (h) to film thickness ratio (t), *i.e.* h/t, and the parameter k_k is a fitting parameter of the implemented weight function. Additionally, on the basis of geometric considerations about the dimensions of the indenter Puchi-Cabrera [65] developed an expression to model the composite hardness by the following expression:

$$H_{\mathrm{C}} = H_{\mathrm{S}} + (H_{\mathrm{F}} - H_{\mathrm{S}}) \exp\left[-\left(\frac{\delta}{k_P}\right)^{m_p}\right] \tag{I.8-10}$$

Where k_P and m_p are fitting parameters correlated to the capability of the film-substrate system to bear indentation loads.

One point to highlight is that when the indentation size effect is incorporated in the analysis of the film-substrate system then the computed macrohardness value (H_0) cannot be directly comparable with those obtained from the direct measurements from the film using the instrumented nanoindentation or when it has been determined performing instrumented microindentation on the film-substrate system. The difference between the values could have supported in several initial assumptions. In the first place, the computation of hardness will be based on the definition adopted, it means that it could be calculated using the projected or the actual contact area. Additionally, the assessment of hardness values could be different depending if the maximum indentation depth (h_{max}) or the contact indentation depth (h_C) is assumed from the methodology proposed by Oliver and Pharr [1] to be taken into account in the evaluation, and furthermore, the indentation size effect could be comprised or not in the calculation of hardness, as it was explained in the earlier section.

Nonetheless, whatever be the assumption to evaluate the hardness behavior of a material, the data acquired by the instrumented indentation tests should be corrected before applying the model, first, to take into account the frame compliance of the instrument to define the appropriate indentation depth data and after, consider the round defect at the indenter tip in the computation of the contact area for the assessment of hardness values.

I.8.3. Elastic modulus from multilayer coating systems

The assessment of the elastic modulus of composite materials is one of the properties that can be obtained by instrumented indentation tests. Moreover, when studying complex system like multilayer coatings on a bulk substrate, illustrated in Figure I.8-1, some mathematical models can be applied to separate the contribution of each layer of the film-substrate system to the composite elastic modulus evaluated from data acquired by instrumented indentation tests. As it was pointed out in previous section I.8.1 (see page 28) numerous models have been developed to describe the variations of the composite elastic modulus of a coated material to estimate the influence of the coating and substrate to the computed elastic modulus value by using the load-displacement curve data. For describing the composite elastic modulus of a coated sample with one layer, the composite elastic modulus (E_{C}) can be expressed, for example, as function of the elastic modulus of the film (E_{F}) and substrate (E_{S}) by a simple linear mixture law as it follows:

$$E_{\mathrm{C}} = a_{\mathrm{F}} E_{\mathrm{F}} + (1 - a_{\mathrm{F}}) E_{\mathrm{S}} \qquad \text{(I.8-11)}$$

Where a_{F} is the volume fraction of film contributing to the composite elastic modulus.

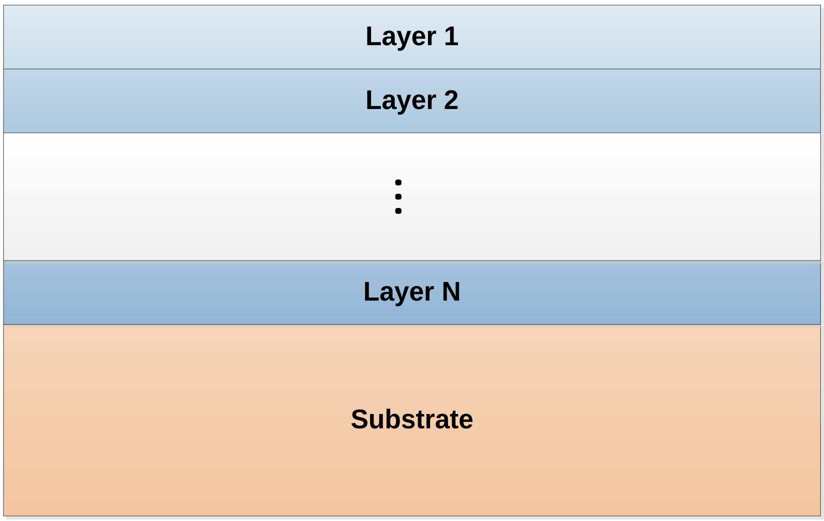

Figure I.8-1. Multilayer coating system sheme to analyze the contribution of each layer to the composite elastic modulus by means of the various models advanced by Puchi-Cabrera *et al*. [68]

Puchi-Cabrera *et al.* [68] proposed a description of the composite elastic modulus of multilayer coated systems. Taking the basis of the reasoning developed by Rahmoun *et al.* [69], it was established the extension of models describing monolayer systems to multilayer systems. Puchi-Cabrera *et al.* [68] state that the contribution of the jth layer to the composite hardness can be calculated as function of the effective volume fraction to discriminate the influence of every single layer of the involved coating in the load-displacement curve acquired by the instrumented indentation test. In first place, the effective volume fraction (a_F) of the first layer (outermost layer) should be defined. Regarding the Table I.8-1, it can be observed the different models and their weight function (f_n) to compute the effective volume fraction of the coating contributing to the composite elastic modulus. Additionally, the analysis of the composite elastic modulus must incorporate the fact that the influence of the substrate into the composite elastic modulus when the indentation depth reach approximately 1% of the film thickness when a monolayer system is under consideration [70]. Extrapolating this concern to multilayer coating systems, it could be state that the influence of the jth layer or the substrate will take place when the sum of the previous layer thicknesses be greater than approximatively 1% of the indentation depth. To describe the variation of the composite elastic modulus on the basis of Puchi-Cabrera *et al.*'s proposal [68], the weight function suggested by Antunes *et al.* [2] is taken as an example to develop the computation of the effective volume fraction of the first and subsequent layers. Accordingly, the general expression to compute the effective volume fraction for the first layer, if a linear mixture law is implemented, is given by:

$$a_{\mathrm{F}}{}^{(1)} = \begin{cases} 1 & \text{if } h < \dfrac{t_{\mathrm{F}}{}^{(1)}}{100} \\ 1 - f_n & \text{otherwise} \end{cases} \tag{I.8-12}$$

Or,

$$a_{\mathrm{F}}{}^{(1)} = \begin{cases} 1 & \text{if } h < \dfrac{t_{\mathrm{F}}{}^{(1)}}{100} \\ f_n & \text{otherwise} \end{cases} \tag{I.8-13}$$

If a harmonic mixture law is applied, where f_n is the weight function depending on the model selected to perform the description of the composite elastic modulus fluctuation. As it was mentioned before, by taking the Antunes *et al.*'s model (Eq. (I.8-1)), the effective volume fraction will be established by the following expression:

$$a_{\mathrm{F}}{}^{(1)} = \begin{cases} 1 & \text{if } h < \dfrac{t_{\mathrm{F}}{}^{(1)}}{100} \\ 1 - \exp\left(-\alpha_3{}^{(1)} \dfrac{t_{\mathrm{F}}{}^{(1)}}{h - \dfrac{t_{\mathrm{F}}{}^{(1)}}{100}} \right) & \text{otherwise} \end{cases} \tag{I.8-14}$$

And, considering the same model, for the j^th^ layer the expression to evaluate the volume fraction contributing with the computed value of the composite elastic modulus is assessed by:

$$a_{\mathrm{F}}{}^{(j)} = \begin{cases} 1 - \sum_{i=1}^{j-1} a_{\mathrm{F}}{}^{(i)} & \text{if } h < \dfrac{1}{100} \sum_{i=1}^{j} t_{\mathrm{F}}{}^{(i)} \\ 1 - \exp\left(-\alpha_3{}^{(j)} \dfrac{\sum_{i=1}^{j} t_{\mathrm{F}}{}^{(i)}}{h - \frac{1}{100} \sum_{i=1}^{j} t_{\mathrm{F}}{}^{(i)}} \right) - \left[1 - \exp\left(-\alpha_3{}^{(j-1)} \dfrac{\sum_{i=1}^{j-1} t_{\mathrm{F}}{}^{(i)}}{h - \frac{1}{100} \sum_{i=1}^{j-1} t_{\mathrm{F}}{}^{(i)}} \right) \right] & \text{otherwise} \end{cases} \tag{I.8-15}$$

Where the film volume fraction $a_{\mathrm{F}}{}^{(i)}$ $(i = 1, \cdots, N)$ of each layer is determined to assess its contribution to the composite elastic modulus; for the j^th^ layer, the parameter $\alpha_3{}^{(j)}$ denotes a fitting parameter to estimate by a non-linear least square regression analysis, and $t_{\mathrm{F}}{}^{(j)}$ represents its thickness. In a multilayer coating system with N layers, the volume fraction of the substrate material $a_{\mathrm{F}}{}^{(S)}$ contributing with the composite elastic modulus is evaluated by:

$$a_{\mathrm{F}}{}^{(S)} = 1 - \sum_{i=1}^{N} a_{\mathrm{F}}{}^{(i)} \tag{I.8-16}$$

In this manner the composite elastic modulus expressed in the Eq. (I.8-11) for a monolayer coated material can be rewritten for a multilayer coating system as follows:

$$E_{\mathrm{C}} = a_{\mathrm{F}}{}^{(S)} E_{\mathrm{S}} + \sum_{i=1}^{N} a_{\mathrm{F}}{}^{(i)} E_{\mathrm{F}}{}^{(i)} \tag{I.8-17}$$

Implementing the Eq. (I.8-12) through (I.8-17), the composite elastic modulus as function of indentation depths for a multilayer coating system can be described and computed. The value of the elastic modulus of each coating layer, $E_{\mathrm{F}}{}^{(i)}$, is estimated by means of a non-linear least square fitting analysis, well-knowing the elastic modulus of the substrate.

I.8.4. Hardness from multilayer coating systems

To study the hardness of multilayer coating systems, and on the basis of the physical meaning of the indented area discussed by Rahmoun *et al.* [69], Puchi-Cabrera *et al.* [71] proposed to extend various hardness models [64, 65, 67] in order to be able to separate the contribution of each layer to the total composite hardness measurement. One of these models is based on the geometrical proposal advanced by Jönsson and Hogmark [14] which expresses the composite hardness (H_{C}) as a function of the film hardness (H_{F}) and the substrate hardness (H_{S}) as it follows:

$$H_{\mathrm{C}} = a_{\mathrm{F}} H_{\mathrm{F}} + (1 - a_{\mathrm{F}}) H_{\mathrm{S}} \tag{I.8-18}$$

Where a_{F} is the volume fraction of the coating contributing on the composite hardness.

Considering that the effective volume fraction of the coating material must fulfill that: $0 \le a_{\mathrm{F}} \le 1$, it can be stated that Eq. (I.8-8) is ill-defined, since when $k_{\mathrm{JH}} \cdot t_{\mathrm{F}} > h$ then a_{F} does not accomplish the condition that it should reach the unit, as it must do it. Accordingly, Rahmoun *et al.* [69] proposed that a_{F} is equal to 1 when the product ($k_{\mathrm{JH}} \cdot t_F$) is higher than the indentation displacement h. Puchi-Cabrera *et al.* [71] advanced that for a multilayer coating system formed by *N* layers, the contribution of the volume fraction from the first coating layer ($a_{\mathrm{F}}{}^{(1)}$) to the composite hardness is defined by:

$$a_{\mathrm{F}}{}^{(1)} = \begin{cases} 1 & \text{if } k_{\mathrm{JH}}{}^{(1)} t_{\mathrm{F}}{}^{(1)} > h \\ 1 - \left(1 - \dfrac{k_{\mathrm{JH}}{}^{(1)} t_{\mathrm{F}}{}^{(1)}}{h}\right)^2 & \text{otherwise} \end{cases} \tag{I.8-19}$$

And, for the j^{th} layer of the multilayer coating system:

$$a_{\mathrm{F}}{}^{(j)} = \begin{cases} 1-\sum_{i=1}^{j-1} a_{\mathrm{F}}{}^{(i)} & \text{if } \sum_{i=1}^{j} k_{\mathrm{JH}}{}^{(i)} t_{\mathrm{F}}{}^{(i)} > h \\ 1-\left(1-\dfrac{\sum_{i=1}^{j} k_{\mathrm{JH}}{}^{(i)} t_{\mathrm{F}}{}^{(i)}}{h}\right)^2 - \left[1-\left(1-\dfrac{\sum_{i=1}^{j-1} k_{\mathrm{JH}}{}^{(i)} t_{\mathrm{F}}{}^{(i)}}{h}\right)^2\right] & \text{otherwise} \end{cases} \tag{I.8-20}$$

In the Eq. (I.8-20) is observed that the contribution from the volume fraction of j^{th} coating layer ($a_{\mathrm{F}}{}^{(j)}$) to the composite hardness is computed from the difference between the volume fraction of such layer and the preceding one. The fraction volume of each layer is calculated on the basis of Eq. (I.8-8), meaning that the volume fraction of the j^{th} layer by means of Eq. (I.8-8) is assessed by subtracting the volume fractions of the previous layers. The volume fraction of the substrate material ($a_{\mathrm{F}}{}^{(S)}$) contributing with the composite hardness can be evaluated by:

$$a_{\mathrm{F}}{}^{(S)} = 1 - \sum_{i=1}^{N} a_{\mathrm{F}}{}^{(i)} \tag{I.8-21}$$

In this manner the composite hardness expressed in the linear mixture law presented in Eq. (I.8-18) can be rewritten for a multilayer coating system as it follows:

$$H_{\mathrm{C}} = a_{\mathrm{F}}{}^{(S)} H_{\mathrm{S}} + \sum_{i=1}^{N} a_{\mathrm{F}}{}^{(i)} H_{\mathrm{F}}{}^{(i)} \tag{I.8-22}$$

By implementing from Eq. (I.8-19) through (I.8-22), the composite hardness as a function of indentation depths for a multilayer coating system can be modeled and computing. The hardness value from each coating layer, $H_{\mathrm{F}}{}^{(i)}$, is estimated by means of a non-linear least square regression analysis, and considering well-known the substrate hardness. Analogically, the film volume fraction $a_{\mathrm{F}}{}^{(j)}$ is computed to evaluate the contribution of the volume fraction of each layer to the composite hardness. Additionally, for the j^{th} layer, $k_{\mathrm{JH}}{}^{(i)}$ denotes a value depending on the indentation behavior of the material and on the geometry of the indenter, $t_{\mathrm{F}}{}^{(j)}$represents its thickness, and $H_{\mathrm{F}}{}^{(j)}$ stands for its hardness.

To apply this model, the constant k_{JH} must be known. $k_{\mathrm{JH}}{}^{(i)}$ $(i = 1, \cdots, N)$ in Eqs. (I.8-19) and (I.8-20) is a parameter only depending on the film nature, and it rests as a constant for whole film thickness.

In an indentation test with a Berkovich diamond indenter this constant is 0.1746 [69] when a hard film is plastically deformed on a soft substrate. This means that the contribution of the substrate to the composite hardness begins at around 17% of the normalized indentation depth instead of the 10% rule suggested by Bückle [72, 73]. If this value is greater, it means that substrate hardness commences to influence hardness computation at higher indentation depths, as it has been observed in other film-substrate systems [74, 75]. Normally, this phenomenon occurs when the film is softer than substrate and thus plastic deformation can occur entirely into the soft film before the indenter tip reaches the film-substrate interface [69]. Chen *et al.* [76] demonstrated that even if the indentation depths reach around 50% of a soft film thickness, the composite hardness is not influenced by a harder substrate. On the other hand, k_{JH} is equal to 0.0915 when indentation test is effected with a Berkovich diamond indenter and the coating fractures [69].

From the work presented by Benarioua *et al.* [77], an application of this model to the hardness of intermetallic compounds from galvanized steel samples were determined by applying the multilayer hardness model described above on classical Vickers microindentation data obtained at different indentation loads as it can be observed in Figure I.8-2. This figure illustrates how the model is able to describe and predict the hardness of each layer of the coating as function of the displacement into surface of the galvanized steel specimen.

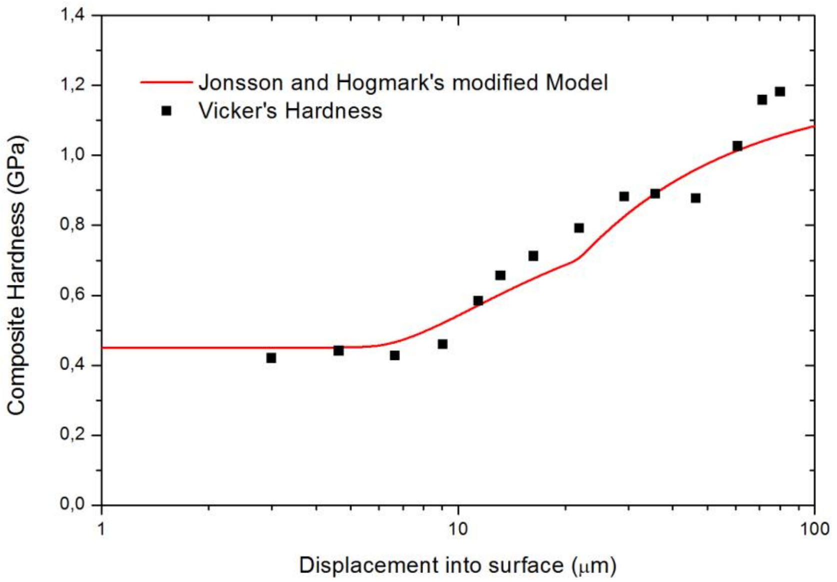

Figure I.8-2. Composite hardness variation of a multilayer coatings from a galvanized steel as a function of the indenter displacement into surface (for a bath immersion of 7 min).

Moreover, Figure I.8-3 shows the volume fraction of each layer from the multilayer coating system to the composite hardness assessed by standard indentation test implemented with a Vickers indenter.

It can be noted from this figure that the volume fraction to contribute from the first (outermost) layer to the composite hardness is dominant until the displacement of the indenter into surface reaches approximately 20 µm when it equals to the volume fraction of the second layer contributing to the composite hardness. The influence of the volume fraction of substrate governs the composite hardness when this is greater than 65 µm.

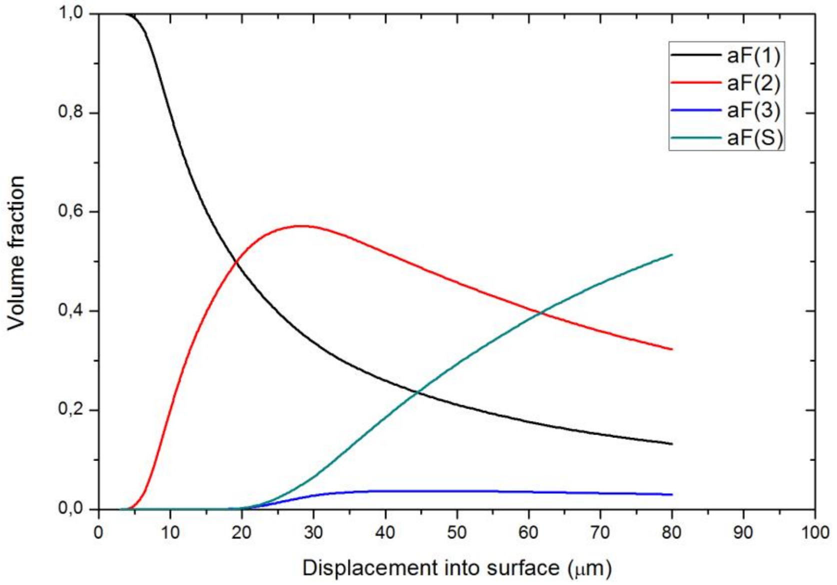

Figure I.8-3. Contribution of each layer and substrate to the composite hardness from the multilayer coating of a galvanized steel specimen.

I.9. CONCLUSIONS

The determination of mechanical properties, such as the elastic modulus and hardness, requires the treatment of a selected data derived from the load-displacement curve resulting from instrumented indentation tests. After the raw data is acquired, the methodology proposed by Oliver and Pharr [1] is widely accepted and used to assess the elastic modulus and hardness of a material by means of the instrumented indentation test. Following their proposal, the experimental contact stiffness (S) and the contact indentation depth (h_C) can be estimated to compute the elastic modulus (E) and the hardness (H) of the material, especially when sink-in phenomenon occurs at the surface around the indenter. One of the most important variables to estimate is the contact area A_C, depending on the mechanical response of the surface beneath the indenter. The contact area could be defined by the expression suggested by Oliver and Pharr [1] if the sink-in phenomenon is predominant, by the relation developed by Bec *et al.* [11] if the pile-up phenomenon is evident, or by using the contact area function proposed by Chicot *et al.* [27]. At the same time, corrections related to the material and to the geometric dimensions of the indenter have to be considered. Additionally, the elastic deflection of the instrument in the recorded indentation depth has to be excluded by calculating the frame compliance of the instrument (C_{f}) in order to obtain a corrected displacement of the indenter into the surface material. The defect of the rounded tip should be estimated too, particularly when analysis is achieved at low loads, *i.e.* at low displacements into surface. When material hardness is evaluated the indentation size effect (ISE) must to be take into account to agree the obtained values in different scales of measurement. Regarding the models to analyze film-substrate systems it can be noted that in these models it must be calculated the contributions of substrate and film to the composite elastic modulus and hardness values which are defined by the weight function, and consequently by the film and substrate volume fraction, generally expressed as the ratio of film thickness to the indentation depth or vice versa.

© 2016 Tous droits réservés. lilliad.univ-lille.fr

Chapter II: MATERIALS AND EXPERIMENTS

II.1. INTRODUCTION

Specimens and framework of experimentations are described in detail in this chapter. Some of the examined materials are considered as homogenous in microstructure and composition whereas others are considered as heterogeneous considering its intrinsic nature. The conditions for preparing the surface of samples are described for each material to be considered in the subsequent analysis of the data from the load-displacement curves. Then, fundaments of the instrumented indentation test are expounded in order to understand the later analysis to carry out with the data acquired by this instrument. The general functionality of the microindentation and nanoindentation instruments is illustrated and clarified to differentiate the two scales of measurements. And finally, the experimental design is presented based on the available specimens so as to evaluate their mechanical behavior by applying a continuous multicycle protocol to ponder the influence of the load-unload sequences into the properties of the material. The conditions of the continuous stiffness measurement (CSM) test and the continuous multicycle protocol are also exposed in this chapter.

II.2. MATERIALS

To achieve the aim of this work, various materials are tested and afterward analyzed. Firstly, carbon steel samples with dissimilar composition are utilized to determine their mechanical properties, *i.e.* elastic modulus and hardness. Secondly, mechanical behavior of hydroxyapatite coating samples (a heterogeneous material) are examined from load-displacement curve data obtained by instrumented indentation tests at microscale range running a continuous multicycle protocol, and lastly, bilayer coating samples of electroless Ni-P deposited on carbon steels are used to study their behavior under the continuous multicycle microindentation tests.

II.2.1. Carbon steel samples

The samples of carbon steel are adopted to estimate the elastic modulus and hardness on these materials by applying the continuous multicycle instrumented indentation test. The mentioned samples are a SAE 1020, SAE 1045 and SAE P20 carbon steels. The SAE 1020 steel (composition in wt. %: 0.18-0.23 C, 0.04 (max.) S, 0.04 (max.) P, 0.15-0.35 Si and 0.30-0.60 Mn) is a low carbon steel used commonly as structural steel. After some chemical process, it can also be employed in steel machinery to manufacture rivets, screws, tubes and metallic structures. The SAE 1045 steel (composition in wt. %: 0.43-0.50 C, 0.04 (max.) S, 0.04 (max.) P, 0.15-0.35 Si and 0.60-0.90 Mn) is a middle carbon steel used to manufacture mechanical components as crankshafts, studs, bolts, clamps, agricultural elements and chains. The SAE P20 steel (composition in wt. %: 0.28-0.40 C, 0.05 (max.) S, 0.03 (max.) P, 0.20-0.80 Si, 0.60-1.50 Mn, 1.40-2.00 Cr and 0.30-1.20 Mo) is a carbon steel alloyed with chromium and molybdenum implemented usually in tools for plastic molds and injection machineries, tools for casting of non-ferrous alloys lead, tin and zinc based, and also in others machinery elements.

II.2.2. Hydroxyapatite coating specimens

Samples of hydroxyapatite coatings were used to study the mechanical properties of this material well-known for its high roughness and its porous conditions, and also for their possibility to replace bone tissues. Regarding their applications, porous hydroxyapatite has been developed to emulate the porous structure of trabecular bone. Among the advantages of the porous condition are the light in weight and also that pores offer a faster replacement of material by bonne tissue owing to appropriate spaces for the ingrowth this one [78, 79]. The increasing interest to characterize the mechanical properties of hydroxyapatite relies on the significance of its mechanical behavior like bone and moreover on the vast application in biomaterials, hard tissue regeneration, and in the medicine field in general [80, 81, 82].

In this experimentation, the solution precursor plasma spraying of hydroxyapatite coatings was realized using SG-100 torch *(Praxair S.T., Indianapolis, IN, USA)* mounted on 5-axis ABB IRB-6 robot *(Zürich, Switzerland)*. The experiments were designed following a two-level, 2^{4-1} plan, by varying solution concentrations (0.1 and 0.3 M) and their injection pressure (0.2 and 0.3 bars), spray distance (50 and 60 mm) and electrical power input to plasma torch (36 and 40 kW), other details are shown in an incoming study [83]. The calcium-phosphate solutions were injected into the plasma jet using a continuous stream injector. The calcium-phosphate (Ca/P) solution was prepared using calcium nitrate tetrahydrate ($Ca(NO_3)_2 \cdot 4H_2O$) and triethyl phosphite ($P(OEt)_3$) as precursors. Triethyl phosphite was hydrolyzed initially using deionized water and appropriate amount of calcium nitrate solution was added dropwise to reach the 1.67 Ca/P stoichiometric ratio. Two different concentrations of solutions were used, namely high solution concentration having Ca/P ratio of [0.5 M/0.3 M] and low solution concentration of [0.167 M/0.100 M] Ca/P ratio. The detailed explanation of the chemistry of the solution and of the plasma spraying parameters used in this work is shown elsewhere [83]. In Figure II.2-1 SEM images illustrate the surface and the cross section of a Hydroxyapatite coating sample realized with a low solution concentration of [0.167 M/0.100 M] Ca/P ratio, and Figure II.2-2 shows a

SEM micrographics from a hydroxyapatite coating sample produced by implementing a high solution concentration of [0.5 M/0.3 M] Ca/P ratio.

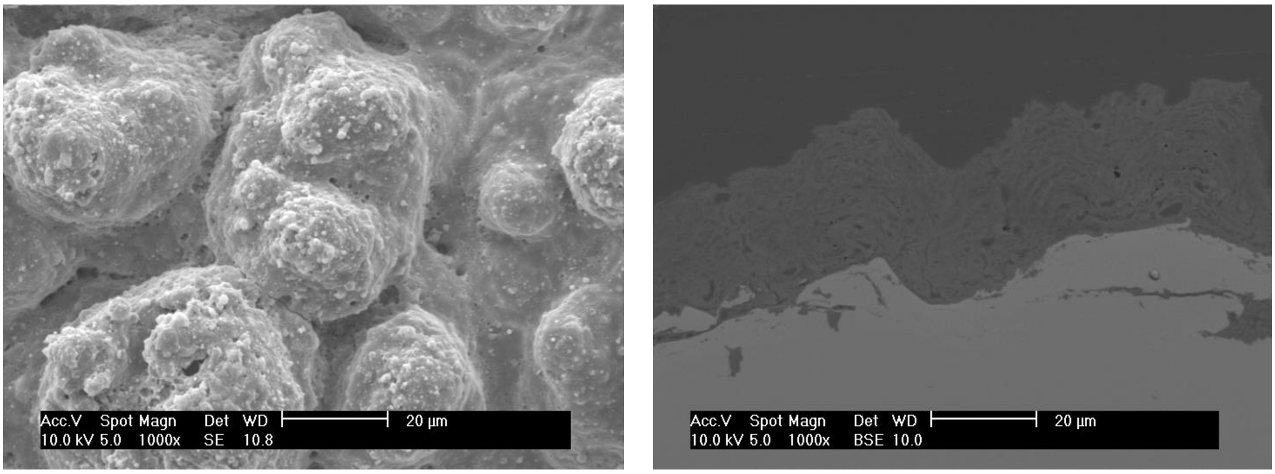
Acc.V Spot Magn Det WD 20 µm
10.0 kV 5.0 1000x SE 10.8
Acc.V Spot Magn Det WD 20 µm
10.0 kV 5.0 1000x BSE 10.0

Figure II.2-1. SEM images of sample using a low solution concentration of Ca/P. Sample surface is showed (left) and its corresponding cross-section (right).

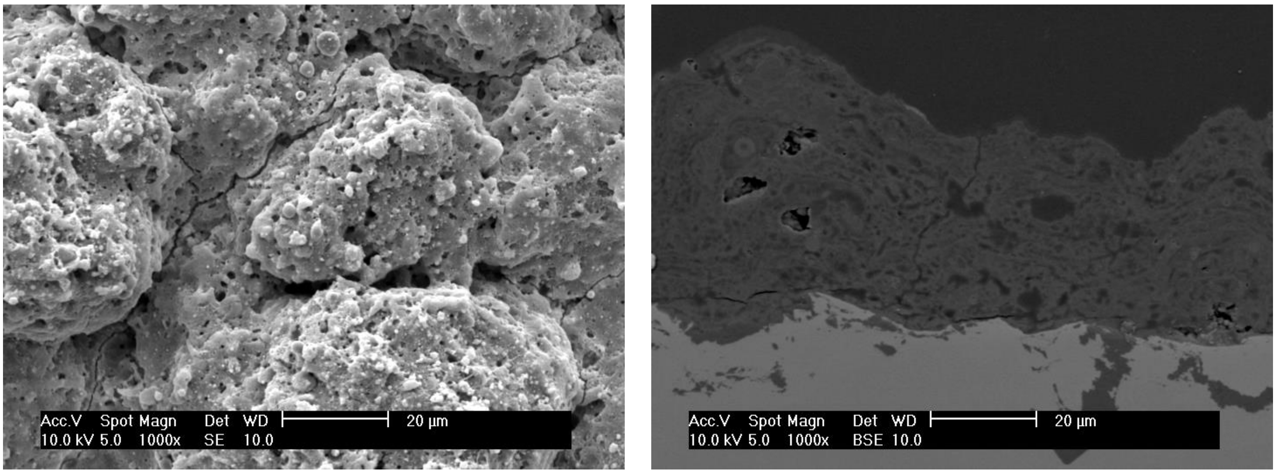
Acc.V Spot Magn Det WD 20 µm
10.0 kV 5.0 1000x SE 10.0
Acc.V Spot Magn Det WD 20 µm
10.0 kV 5.0 1000x BSE 10.0

Figure II.2-2. SEM micrographs of sample using a high concentration solution of Ca/P. The surface of the sample is exhibit (left) and its corresponding cross-section (right).

Additionally, the thickness of coating was measured by means of SEM techniques. Table II.2-1 collects the mean value and the standard deviation of thickness for all samples.

Table II.2-1. Film thickness from sprayed hydroxyapatite coating samples.

	High initial solution concentration				Low initial solution concentration			
Sample code	H-1	H-2	H-3	H-4	L-1	L-2	L-3	L-4
Thickness (µm)	51	48	45	47	41	43	53	49
Standard deviation (µm)	8	7	4	5	3	5	3	4

II.2.3. Carbon steels coated with a bilayer electroless Ni-P deposits

The electroless nickel based coatings are extensively used to improve the surface properties of a base material, such as electrochemical behavior and hardness [84], and also it is utilized as a good catalytic electrode material in hydrogen evolution reaction, although it has a low electrocatalytic performance [85, 86]. This type of coating is used above all in electroless engineering technologies owing to its low cost and malleability [87, 88, 89, 90]. Recently, Shibli *et al.* [91] developed electroless Ni-P coatings reinforced with nano NiO to improve the electrocatalytic performance of this kind of coatings. On the one hand, the loss of the electrocatalytic activity with time suffered by the nickel coatings is overcame, and on the other hand, it would be an alternative material to be applied in hydrogen processes considered as the fuel of the future [92, 93, 94]. High performance in corrosion and wear resistance and electromagnetic characteristics are some others benefits showed by the electroless Ni-P alloy coatings, whereby the scientific researchers are interested into them [95, 96, 97].

The samples of electroless Ni-P coatings were deposited in two layers on carbon steel plates with the aim of analyze the behavior of the film-substrate system under continuous multicycle indentation tests. The electroless Ni-P deposition was effectuated by an industrial process employing a bath with a formulation such as 30 g/l of nickel sulphate, 30 g/l of sodium hypophosphite, 35 g/l of malic acid, 1.5 ppm of lead sulphate, 10 g/l of succinic acid and a stabilizer. During deposition the pH was maintained at approximately between 4.6 and 4.8, at a mean temperature from 85 to 89°C. The deposition rate oscillated between 5 and 10 µm/h and the process for the two layers was carried out in two phases: (*i*) a first coating deposition applied over the substrate, afterward it was heat treated at 400 °C for 1 h, and (*ii*) a second coating effected on top of the first coating, and then it was heat treated for 2 h at 200 °C. The two thermal treatments provide different coating properties; first coating (innermost) offers a high hardness value (in the order of 900 to 1000 Vickers) with a crystalline metallographic structure (usually with 0% to 2% microcracks) which is highly wear resistant; while the second coating (outermost) of lower hardness (in the order of 550 to 650 Vickers) offers high corrosion resistance due to its amorphous metallographic structure (with no microcracks) which has the property of penetrate into microcracks of the first coating. This bilayer coating system offers simultaneously high wear and corrosion resistance, since once the outermost corrosion resistant coating wears off, the innermost coating starts to work but now with its microcracks filled with the amorphous coating, thus it does not allow to corrosive environment to reaches the substrate. The applied deposit had a phosphorous content in the order of 9 to 12% wt. and for this project, a thickness of approximately 10 µm at each layer of the bilayer film system was expected. Nevertheless, by means of a scanning electron microscopy, the total thickness of the bilayer coating system appears to be greater than 50 µm, as it can be appreciated in Figure II.2-3.

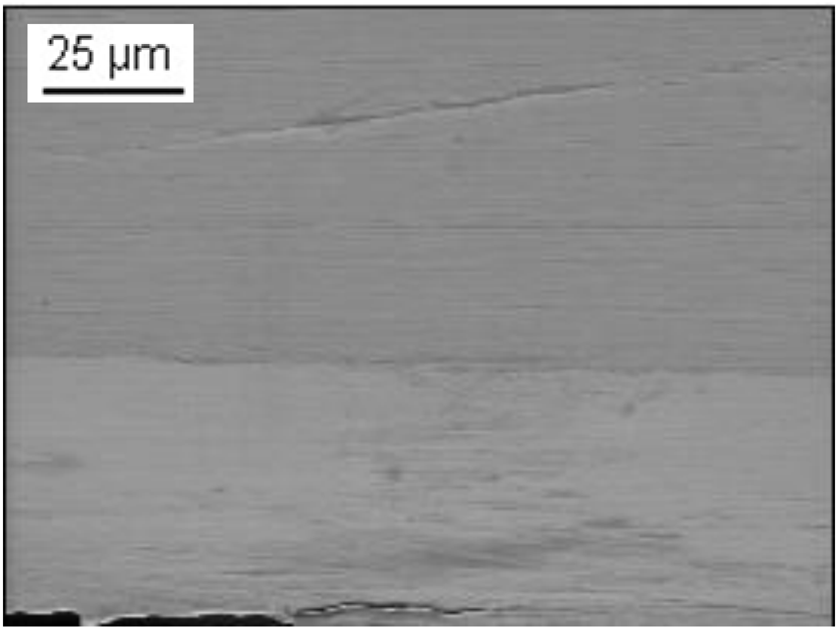

Figure II.2-3. SEM image from the bilayer electroless Ni-P coating deposited on a SAE 10210 carbon steel plate.

Additionally, an analysis by EDS was performed with the aim of verify the presence of a diffusion layer between the coating and the substrate. The 2-D distribution of the elements recorded with the assistance of the EDS such as Fe, Ni, and P is illustrated in Figure II.2-4. The elements Ni and P are distributed homogeneously in the zone delimited by the coating. Additionally, Figure II.2-4 shows without any doubt the interface well delimited between the substrate (carbon steel) and the bilayer Ni-P coating. From this figure, it can be noted the absent of the Ni element into the substrate, and in the same way the Fe element is not present into the bilayer Ni-P electroless coating. The phosphorus is present into the both materials of the film-coating system. On the one hand, the high presence of this element in the coating is obviously expected due to its nature, and on the other hand, the manifestation of the P element was expected in the substrate according with the 0.04 wt. (%) of this element existing in its chemical composition. Furthermore, the percentage in weight of P in the bilayer coating was corroborated to be between 9 and 12% wt.

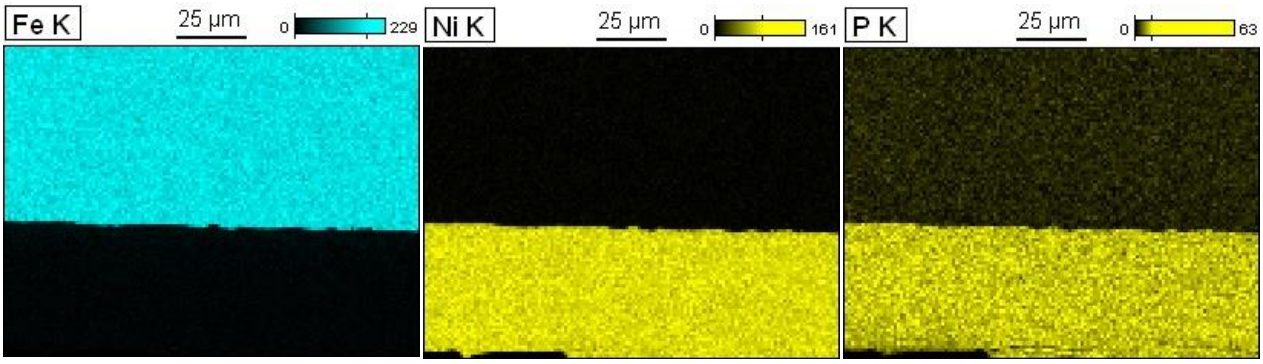
Fe K
25 µm
0
229
Ni K
25 µm
0
161
P K
25 µm
0
63

Figure II.2-4. EDS analysis performed to identify the possible diffusion process between the coating and hardness. Fe element is absent in the electroless Ni-P coating (left), Ni element inattentive in the substrate (center) and existence of P element in both substrate and coating but more important in the electroless Ni-P coating (right).

Figure II.2-5 illustrate the scheme of the heat treatment condition of the electroless Ni-P coatings deposited on carbon steel plates. The carbon steel used as substrate were the SEA 1020, 1045 and P20 described above. The bilayer electroless Ni-P coating described earlier was deposited on the three carbon steel samples, and additionally, electroless Ni-P monolayer coatings were deposited (in same conditions described earlier) on same substrates, but only submitted to one of the two heat treatment effected to the bilayer electroless Ni-P coating system, that were expounded previously. The bilayer coating system is named as “B”, the monolayer coating heat treated at 400 °C is called “I”, and the monolayer coating heat treated at 200 °C is labeled “O”.

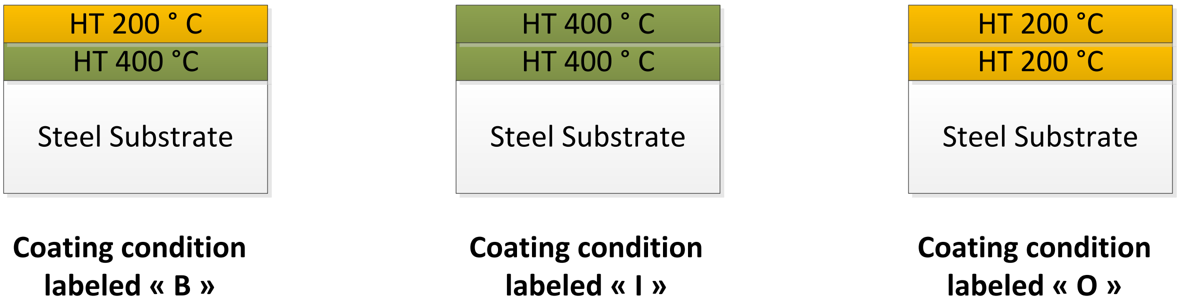
HT 200 ° C
HT 400 °C
Steel Substrate
Coating condition labeled « B »
HT 400 ° C
HT 400 ° C
Steel Substrate
Coating condition labeled « I »
HT 200 °C
HT 200 °C
Steel Substrate
Coating condition labeled « O »

Figure II.2-5. Scheme of the heat treatment of every single electroless Ni-P coatings deposited on the steel substrate plates.

II.2.4. Metallography preparation and polishing

The carbon steel specimens were metallography prepared starting with successive abrasive silica carbon papers N° 180, 220, 380, 500, 800 and 1200, and after polished mechanically by a sequential diamond polishing from 9, 6, 3 µm to, finally, 1 µm obtaining a final polished surface like a mirror.

The hydroxyapatite coating samples and the electroless Ni-P coating deposited on carbon steel plates were studied as received in order to not vary the original condition of the material surface, in other words, to avoid any modification on the remaining stresses, thickness of coatings, or residual stresses among others.

II.3. INDENTATION EXPERIMENTS

II.3.1. Fundaments of the Instrumented Indentation Test (IIT)

The instrumented indentation test consists to drive in an indenter with a well-known geometric shape into the surface of a material to be analyzed with the aim of evaluate its mechanical properties such as the hardness and elastic modulus, among others. Concerning the assessment of the hardness, it can be done by classical tests where this one is computed by the measures obtained from the left impressions of the indenter into the material surface and the applied load for this purpose. In contrast, by means of the instrumented indentation test the analysis from load-displacement curves allows to compute other mechanical properties besides the hardness. To carry out the instrumented indentation tests, one of the variables to select is the shape of the indenter to be implemented. The geometry of the indenter could be spherical, conical and pyramidal which differs not only in its profile but also in the size of their principal characteristic dimension. The present study was performed using micrometric pyramidal indenters (Berkovich type) in the domain of the nanoscale and microscale range in order to study and evaluate the mechanical properties of materials to take into account the variations on their surface and on their microstructure.

II.3.2. Description of instruments

II.3.2.1. Microindentation Instrument CSM 2-107

The microindentation instrument employed was a CSM 2–107 developed by the CSM Instrument manufacturer showed in Figure II.3-1. The schematic of the instrument is illustrated in Figure II.3-2. In this instrument, the load range varies from 0.05 to 30 N. The load resolution of the instrument equals to 100 µN and the maximum displacement permits by the machine is up to 100 µm, and for this measurement the resolution is 0.3 nm. The positioning of the loading column is established by a displacement sensor. The load in the loading shaft is imposed by the electromagnetic coil placed in the upper part of the instrument.

© 2016 Tous droits réservés. lilliad.univ-lille.fr

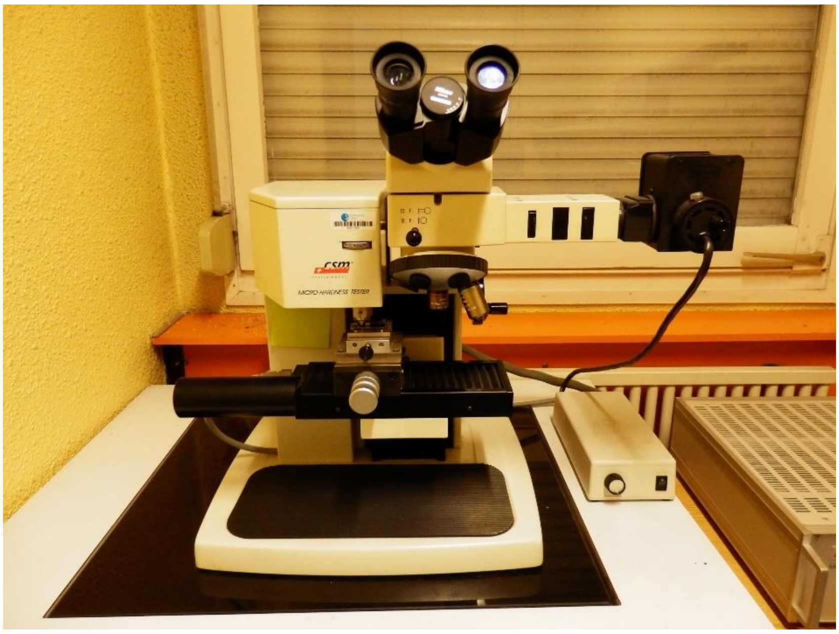

Figure II.3-1. Microhardness indenter CSM 2–107 manufactured by CSM instruments used to perform the instrumented indentation tests at the microscale range.

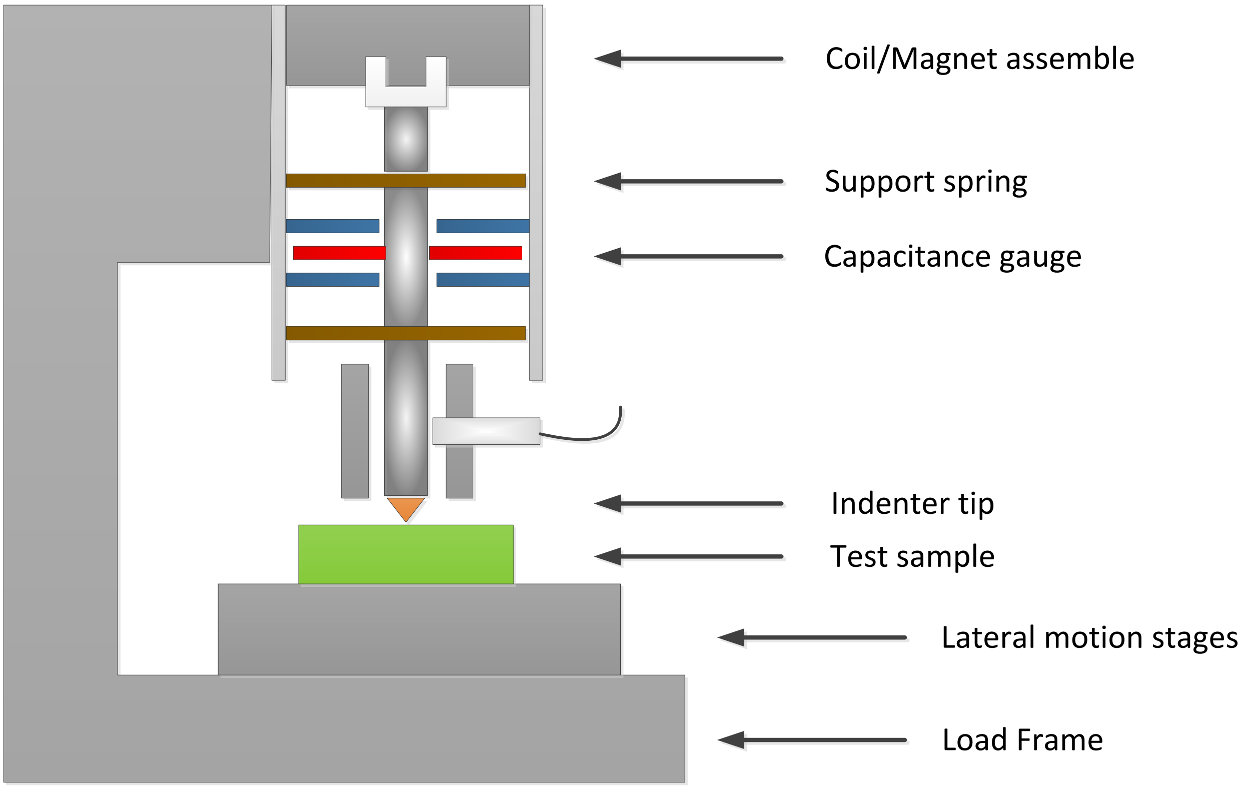
Coil/Magnet assemble
Support spring
Capacitance gauge
Indenter tip
Test sample
Lateral motion stages
Load Frame

Figure II.3-2. Schematic of indentation instrument test at both nanoscale and microscale range.

The adjustment of the load imposed on the loading column is performed by the variation of the current circulating through the magnetic coil. In this case, the loading column is supported by springs with a very low stiffness in the vertical direction and very high stiffness in the horizontal direction. A stage motorized following the Y-axe permits the positioning of the sample beneath the indenter. The test sample is fixed in the stage in order to immobilize the sample when the test is running. By means of an optical microscope coupled with the instrument, the residual impression can be observed or/and the positioning of the sample can be fixed. The test framework, in other words, the charge and discharge rates, the dwell time and data acquisition rate is accomplished by using the software installed in the computer developed by CSM. Nevertheless, the analysis and interpretation of the data acquired is realized using the theoretical background explained in the preceding chapter 1.

II.3.3. Nanoindentation Instrument MTS XP

The nanoindentation instrument utilized was a Nano Indenter XP™ developed by MTS Nano Instruments. The nanoindentation instrument, as well as the microindentation instrument, executes indentation tests by conducting a diamond indenter into the surface of a material and continuously recording the applied force on sample and displacement into surface data. Owing to the working range, this instrument is in a specially designed enclosure insulated against temperature variations, vibrations and acoustic noise that could be present in the laboratory.

In the same way that the microindentation instrument, the loading column transmits the load to the indenter by passing current through an electromagnetic coil that sits within a circular magnet as illustrated in Figure II.3-2. Consequently, the load applied on the indenter shaft is directly proportional to the current passed through the electromagnetic coil. The loading shaft and the hardware of the nanoindentation instrument is designed as a heavy construction in order to reduce the transmission of mechanical vibrations and also have a very high compliance to diminish the influence of the reaction forces in the displacement data. The calibration of the force signal is carried out at the factory by balancing a series of standard weights with the indenter. For the implemented Nano Indenter XP™, the theoretical load resolution equals to 50 nN [98]. This instrument is operated normally as load controlled system, although it may be operated as a displacement-controlled system by using the software controlled feedback.

The displacement sensing system consists of the three-plate capacitive arrangement showed in Figure II.3-2. All three plates are circular disks. On the one hand, the loading column is placed in the holes in the center of the two outside plates fixed to the head. On the other hand, the center plate is fixed to the indenter shaft and this one can move vertically between the others two outside plates. The position of the loading column within the gap is established as a function of the difference in voltage between the center plate and either of the two outside plates. The calibration of the displacement sensor is carried out by means of laser interferometry at the manufacturer. For the used Nano Indenter XP™, the theoretical displacement resolution is less than 0.01 nm [98].

Concerning the sample mounting, the specimens are fixed normally with wax or mounting adhesive. The motion stage where is placed the specimen holder has a fine resolution of positioning following the X and Y axes in order to allow indentations to be made in very small features such grains, interfaces or conductive pads in an integrated circuit [98]. To place specimens in the instrument, they should be relatively smooth and flat.

II.3.4. The experimental design of the instrumented indentation test

From a general point of view, to estimate the value of the Young's modulus and hardness from samples, the microindentation experiments were carried out using the microhardness tester CSM 2-107, described above. In this work, tests were performed using a continuous multicycle protocol, moreover, specific loading-unloading conditions were applied accordingly to the tested sample.

A) Carbon steel samples. The carbon steel samples were tested with the microindentation instrument with a Berkovich indenter. The maximum loads set in the experimentation were equals to 100, 200, 300, 400, 500, 600, 700, 800, 900 mN and 1, 2, 3, 4, 5, 6, 7, 8, 9, 10 N. The dwell time configured at the maximum load of each test was equal to 15 s. At least, three indentations tests were executed for each load applied and the data of the load-displacement curve were collected to calculate the mechanical properties of the material. And after, by following a continuous multicycle protocol. The parameters employed to set up the tests were 100 cycles per test, and the loading and unloading rates (expressed in mN/min) as twice the value of the maximum load applied, to guarantee that all cycles last same time. Additionally, the applied maximum load at the first cycle was 1 N and the last one was 20 N, load to unloading was set as 20% of the maximum load at each cycle, and a dwell-time of 15 s was imposed at the maximum and minimum load, according to the standard indentation test procedure ASTM E92-82 [99].

The steel samples were also tested with the Nano Indenter XP™ by using a Berkovich indenter. The instrument was operated on the Continuous Stiffness Measurement mode (CSM) allowing the determination of the hardness at each data point during the indentation loading. 25 indentation tests were conducted randomly at the surface of the polished surface by applying the same indentation testing conditions. The maximum indentation depth reached by the indenter was fixed at 2000 nm and the strain rate was equal to 0.05 s^{-1}. The harmonic displacement was set to be 2 nm and the frequency was equal to 45 Hz. The sample was fixed on a metallic support using the heat softening glue crystal bond.

B) Hydroxyapatite coating samples. In order to compute the value of the Young's modulus and hardness from the hydroxyapatite coating samples, only microindentation tests were performed using the continuous multicycle protocol. In this case, the parameters employed to set up the tests were 100 cycles per test, and loading and unloading rates (expressed in mN/min) as twice the value of the maximum load applied, to guarantee that all cycles last the same time. Moreover, the maximum load applied at first cycle was 200 mN and at the last one was 20 N, load to unloading was set as 20% of the maximum load at every single cycle, and a dwell-time of 15 s was imposed at the maximum and minimum load.

C) Electroless Ni-P coating samples. The electroless Ni-P coating deposited on carbon steel plates were tested in the microindentation instrument implementing a Berkovich indenter also by using a continuous multicycle indentation test. The parameter employed for these specimens to set the framework test were 100 cycles per experiment, and loading and unloading rates (expressed in mN/min) as twice the value of the maximum load applied, to guarantee that all cycles last same time. Moreover, the maximum load imposed at first cycle was 1 N and in the last one was 18 N, load to unloading was set as 20% of the maximum load in very single cycle, and a dwell-time of 15 s was implemented at the maximum and minimum loads.

These samples were also tested with the nanoindentation instrument with a Berkovich indenter. The instrument was operated on the Continuous Stiffness Measurement mode (CSM) allowing the determination of the hardness at each data point during the indentation loading. 25 indentation tests were conducted randomly at the surface of the polished surface by applying the same indentation testing conditions. The maximum indentation depth reached by the indenter was fixed at 2000 nm and the strain rate was equal to 0.05 s^{-1}. The harmonic displacement was 2 nm and the frequency is equal to 45 Hz. The sample was fixed on a metallic support using the heat softening glue crystal bond.

Chapter III: RESULTS AND DISCUSSION

Instrumented indentation tests have been widely used in last decades. Many difficulties have been overcome in the assessment of mechanical properties using this technique. From microindentation to nanoindentation, and more recently ultra nanoindentation, these tests have been applied to evaluate the mechanical response of bulk and coated materials to study its application on different industrial fields. Moreover, the estimation of mechanical properties has evolved from the evaluation of single crystal or homogenous materials to more complex system of composite materials. In order to contribute to the development of this important technique an original methodology using continuous multicycle indentation data is advanced and discussed to be applied in different types of materials, from homogenous to heterogeneous materials, and from bulk to coated materials. By applying this methodology, carbon steel samples (considered as a homogeneous material) are submitted to continuous multicycle tests at microscale range to evaluate its influence on the computation of their mechanical properties, *i.e.* hardness and elastic modulus. Additionally, with the assistance of CSM tests a new approach to compute the elastic modulus of materials from the experimental contact stiffness is advanced.

So as to evaluate the mechanical properties in heterogeneous materials in a continuous load-unload sequence, samples of Hydroxyapatite (HA) coatings are studied and analyzed. According to the literature, previous investigations have been made in order to characterize mechanically this coating material. Nevertheless, a vast quantity of research has been developed in the nanoindentation range, where the surface roughness plays an important contribution to the data acquired by nanoindentation instruments, and in somehow the response of the material at higher and continuous load have not been yet completely evaluated. Considering this condition, it is expected that the values obtained by means of nanoindentation instruments were not able to assess an overall evaluation of coated material as the indenter goes deeper into the coating and interact with the presence of microdefects like cracks or pores. In contrast, at microscale range by executing standard instrumented indentation tests, it could lead to neglect the influence of the surface roughness, thickness, microcracks or microdefects under the indenter when the loads are applied in different points of the sample surface. Conversely, at nanoscale range the heterogeneities of material will show a large dispersion among the acquired data at each point owing to the different mechanical response as function of the heterogeneities into the material. Accordingly, a continuous multicycle indentation test at microscale range overcomes these difficulties on heterogeneous materials to evaluate their mechanical properties as function of the indentation depth and a new model is advanced to evaluate the influence of the densification process of the porous structure of the hydroxyapatite coatings samples on hardness behavior.

Afterward, a bilayer electroless Ni-P coatings deposited on carbon steel plates are evaluated to ponder the mechanical behavior of the film-substrate system under a continuous multicycle indentation test, accomplishing this aim by applying multilayer models to discriminate the contribution of every element of the system (each single layer and the substrate) to the computed composite mechanical properties. Finally, a different approach to evaluate the contribution of each element of the bilayer coating system to the composite elastic modulus is suggested.

III.1. EVALUATION OF HARDNESS AND ELASTIC MODULUS OF CARBON STEEL SAMPLES BY CONTINUOUS MULTICYCLE INDENTATION TESTS AND CONTINUOUS STIFFNESS MEASUREMENT

III.1.1. Mechanical properties evaluated by continuous multicycle indentation tests

III.1.1.1. Introduction

The elastic modulus and hardness from carbon steel samples are computed from the data acquired by a continuous instrumented indentation test. To compute these mechanical properties from carbon steel samples, the registered data is submitted to corrections due to the compliance frame of the instrument, blunt defect of the indenter tip, deformation of the material beneath the indenter governed by the Poisson’s coefficient of the material and also by the mechanical response of material surface around the indenter depending on the occurrence of pile-up or sink-in phenomena. According with an earlier investigation, the response of the material around the indenter is examined to refine the computation of the contact area between the indenter and the sample surface. The information base collected by continuous multicycle indentation experiments on carbon steel samples are computed to investigate the comportment of the hardness and elastic modulus as function of the maximum indentation depth reached at each cycle of the loading-unloading sequence. Additionally, hardness behavior from this continuous multicycle indentation test at microscale range is modeled by two different approaches which describe the indentation size effect on the above mentioned samples. Furthermore, with the aid of CSM test at nanoscale range an innovative proposition is advanced in order to estimate the reduced elastic modulus of the samples from the experimental contact stiffness recorded by the instrument.

III.1.1.2. Results and treatment procedure of the raw data

The three carbon steel samples described in the previous chapter 2 were submitted to instrumented indentation tests using a continuous multicycle protocol. Figure III.1-1 and Figure III.1-2 illustrate the difference between a standard indentation test and a continuous multicycle indentation test. Figure III.1-1 illustrates standard instrumented indentation tests carried out at different maximum loads, from 1 N to 10 N. It can be noted from this illustration the reproducibility of tests when these ones are performed on the same sample and test conditions.

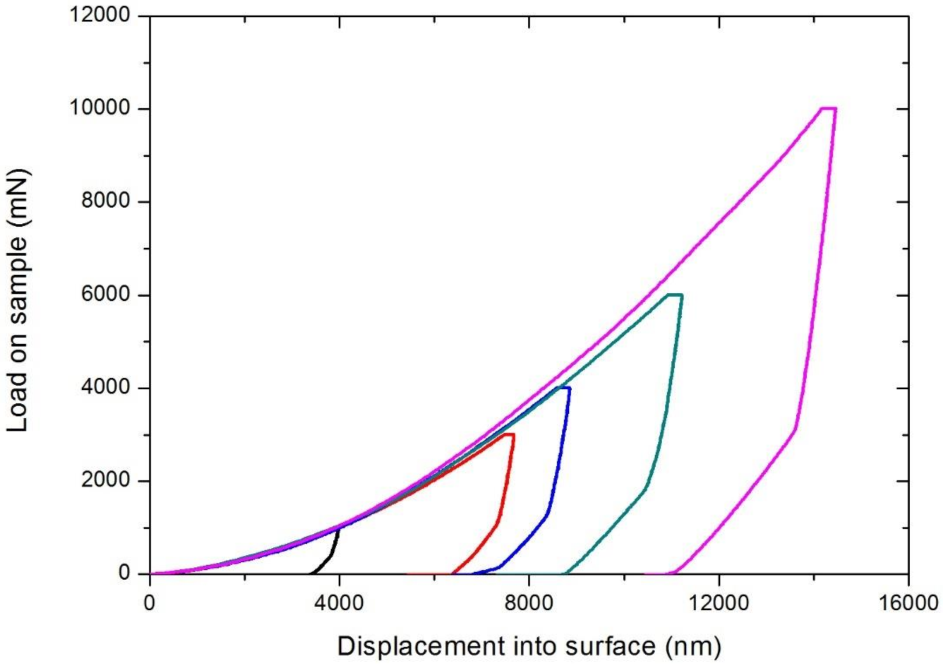

Figure III.1-1. Load-displacement curve registered by standard indentation tests accomplished on a SAE 1020 carbon steel specimen at maximum loads of 1, 3, 4, 6 and 10 N.

Alternatively, Figure III.1-2 shows a representative instrumented indentation test running a continuous multicycle protocol. As it can be seen in this graphic, the mechanical properties of the sample can be assessed at each cycle of the loading-unloading sequence. Moreover, the principal advantage using the multicycle indentation test appears when heterogeneous materials must be evaluated because it allows to derive the mechanical properties at each cycle at different maximum loads from one and all unloading segment in the same point of application from the recorded load-displacement curve. Also, it can be called the attention to the difference between the analysis of standard tests and the continuous multicycle indentation tests. Normally, the standard tests are accomplished at different points in the specimen surface and certainly at different maximum loads, it means, that differences in roughness, microstructure, microdefects or microcracks (in heterogeneous materials) and actual thickness (when coatings are involved) could interfere in computing the mechanical properties or in examining them when all these tests are used to determine them, for example, by applying the proposal described by Oliver and Pharr [1]. In contrast, a continuous multicycle indentation test allows the characterization of the material using the same point of application by obtaining multiple data that can be analyzed in order to evaluate the mechanical properties of materials under identical surface conditions. It must be verified that there is not an effect of the load-unload sequences on the inherent mechanical properties of the examined materials.

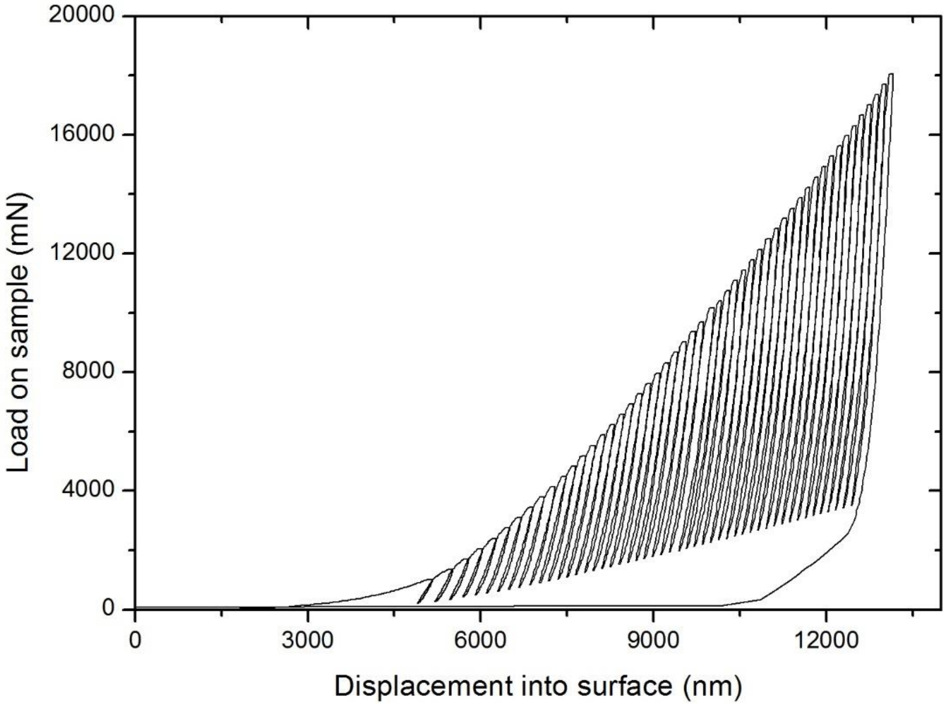

Figure III.1-2. Load-displacement curve performed by a continuous multicycle indentation test on a steel sample.

III.1.1.3. Assessment of the deformation mode around the indenter

According with the experimental design described in chapter 2, the unloading segment of each and every cycle was analyzed following the methodology described by Oliver and Pharr [1], and clarified previously in chapter 1. From the recorded information base, values of maximum loads ($P_{\max}$), maximum indentation depths ($h_{\max}$), contact stiffness (S) and the residual indentation depths (h_{f}) are computed and condensed in the interest of evaluate the mechanical properties of the material samples. With the figured values of maximum indentation depths and residual indentation depths, the proposal suggested by Yetna *et al.* [100] is applied to establish the deformation mode around the indenter. According with this method, the ratio from the residual contact depth (h_{f}) to maximum indentation depth ($h_{\max}$) is calculated. Figure III.1-3 illustrates this ratio for every single cycle and as it can be seen it remains greater than 0.83, independently of maximum indentation depth, *i.e.* this quotient does not depend on the applied load. Moreover, as it was advanced by the authors [100] this ratio depends intrinsically only on the material.

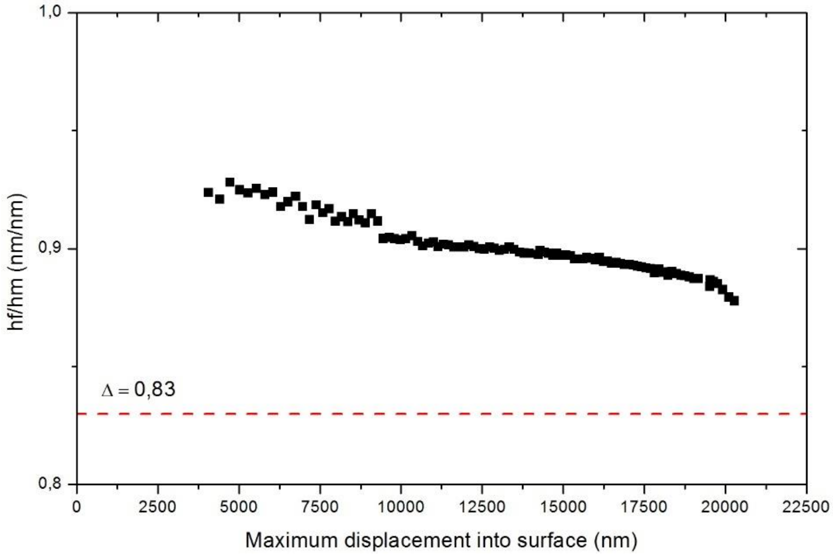

Figure III.1-3. Representation of the ratio of h_f to h_m ($\Delta = h_f/h_{max}$) as function of the maximum indentation depth (h_m) derived from every single cycle.

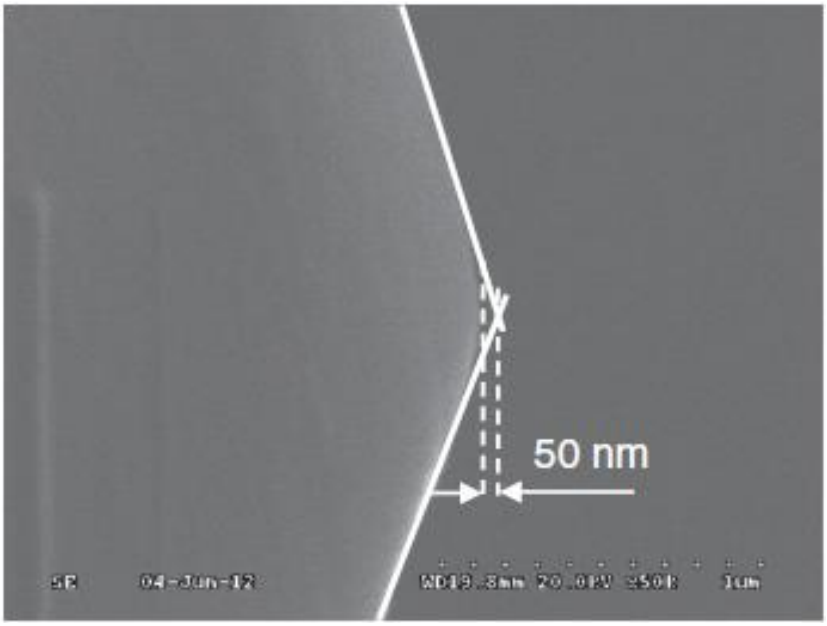

Figure III.1-4. Estimation of the tip defect dimension for the utilized Berkovich indenter by means of an emission field SEM analysis.

Once the raw data has been acquired, the correction of data must be applied. Among these corrections, the estimation of the blunt defect of the indenter tip is effectuated. The value of 50 nm is added to the recorded displacement (h_{meas}), and after it will be corrected by the frame compliance of the instrument (C_f). Figure III.1-4 shows the estimation of the blunt defect of the indenter tip from a SEM micrograph performed to the handled Berkovich indenter from a previous work [101].

Once that the tip defect has been quantify and the deformation mode around the indenter is defined to estimate the contact area, the compliance frame of the machine (C_f) must be determined in order to correct the load-displacement curve and recalculate the reduced elastic modulus from the slope of the plot from the reciprocal of the experimental contact stiffness ($1/S$) versus the reciprocal of the square root of contact area ($1/\sqrt{A_\mathrm{C}}$). Figure III.1-5 illustrates this plot from ($1/S$) as function of ($1/\sqrt{A_\mathrm{C}}$). It is noticeable that the corrected data can be adjusted to a straight line with intercept at zero. From the slope of this straight line, the reduced elastic modulus (E_R) can be assessed.

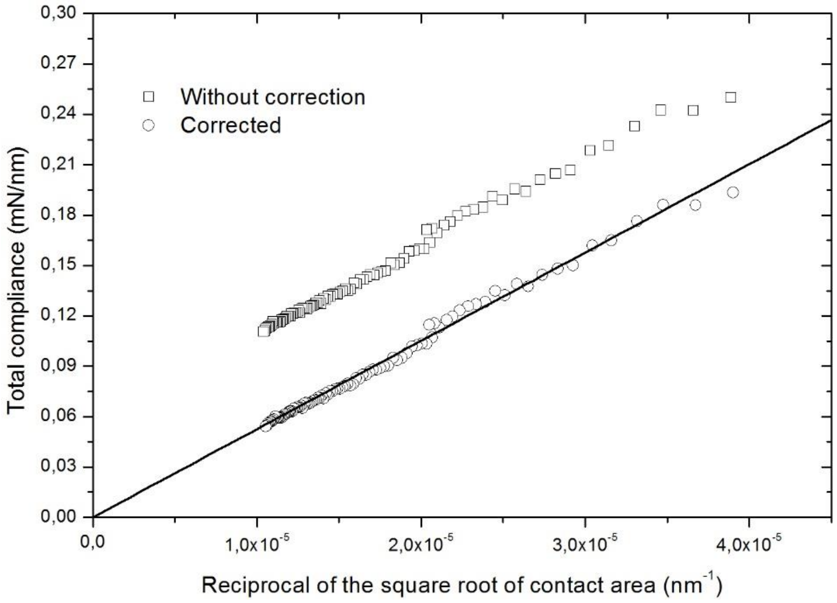

Figure III.1-5. Total compliance (C_T), or reciprocal of the experimental contact stiffness (1/S), as function of the reciprocal square root of contact area ($1/\sqrt{A_C}$).

The methodology computed and developed along this section will be extended to the analysis of heterogeneous and coated materials in the upcoming sections.

III.1.1.4. Study Case: Carbon steels samples

From the unloading part of the load-displacement curve the elastic modulus and hardness of the material is calculated. Figure III.1-6 shows the behavior of the elastic modulus as a function of the maximum contact depth h_max from one test performed on the SAE 1020 carbon steel sample. For this sample the elastic modulus was found to be 158 ± 4 GPa; the elastic modulus from the SAE 1045 specimen was equal to 179 ± 9 GPa, and from the SAE P20 sample it was obtained a value of 190 ± 9 GPa as the elastic modulus of the sample.

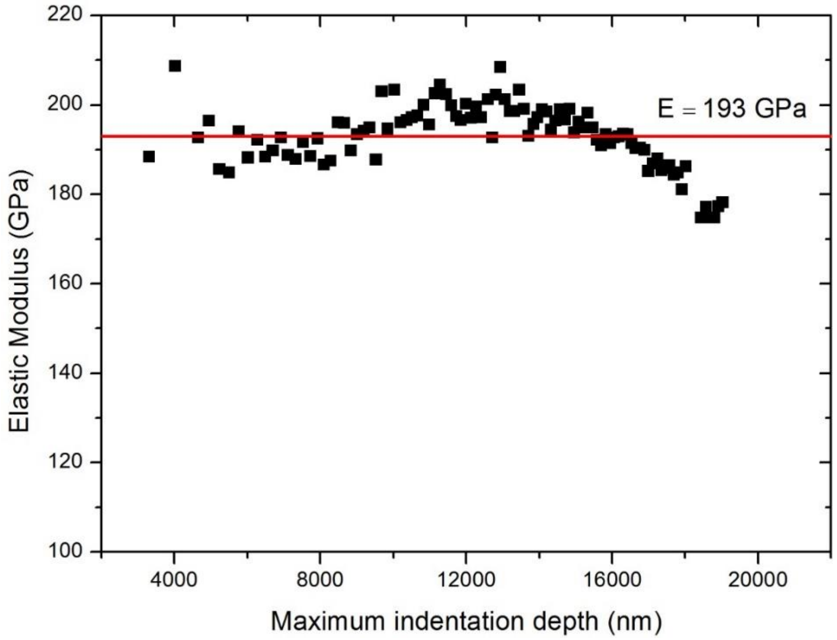

Figure III.1-6. Elastic modulus of a SAE 1020 carbon steel sample computed from a continuous multicycle indentation test.

It can be stated that the elastic modulus remains constant for the whole test and consequently any important damage on the material surface could be estimated from this ductile material from the continuous multicycle instrumented indentation tests. Table III.1-1 collects the values assessed by using the data acquired by continuous multicycle indentation tests. The figured elastic moduli for the three carbon steel samples agree with those reported in the literature for this kind of material [102]. It is interesting to observe that the standard deviation from the values obtained is around of 5% which can be interpreted as that the estimation for this evaluated property converges.

Table III.1-1. Elastic modulus computed from continuous multicycle indentation test from SAE 1020, SAE 1045, and SAE P20 carbon steel samples.

Sample	Elastic Modulus, E (GPa)
SAE 1020	158 ± 4
SAE 1045	179 ± 9
SAE P20	190 ± 7

It is important to mention that values in Table III.1-1 are estimated using the correction factor depending on material (γ) proposed by Hay *et al.* [40] that is normally applied in microindentation tests and it could diminish the actual elastic modulus in around 10%.

Another mechanical property to be valued is the material hardness. To study this property, the Martens hardness definition is adopted as a function of the maximum applied load (P_{max}) at each cycle and the true contact area (A_m), expressed bellow:

$$HM = \frac{P_{\mathrm{max}}}{A_m} = \frac{P_{\mathrm{max}}}{26.43(h_{\mathrm{max}} + h_{\mathrm{b}})^2} \tag{III.1-1}$$

Regarding in Figure III.1-7 the behavior of this mechanical property at each cycle, the comportment is associated to the influence of the indentation size effect (ISE). Figure III.1-7 also illustrates the description of the Martens hardness based in the proportional specimen resistance model proposed by Li and Bradt [103], as it is indicated below:

$$HM = HM_0 + \frac{\Delta_{\mathrm{L-B}}}{h} \tag{III.1-2}$$

From this model the Martens macrohardness (HM_0) was found to be between 1.60 and 2.84 GPa and $\Delta_{\mathrm{L-B}}$ (parameter that quantifies the indentation size effect) was valued from 2.35 to 2.70 MPa·m.

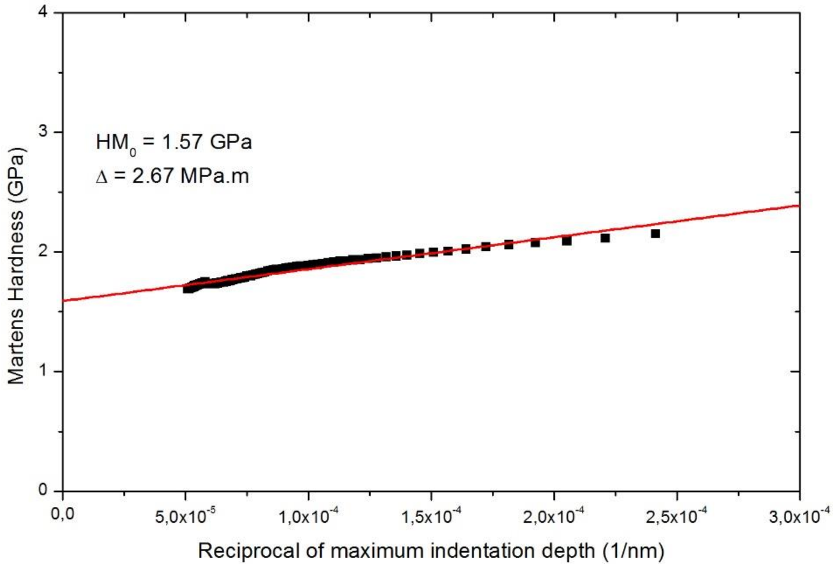

Figure III.1-7. Martens hardness (HM) versus the reciprocal of the maximum indentation depth ($1/h_{\mathrm{max}}$) for the SAE 1045 carbon steel sample by the proportional specimen resistance model [103] applied to hardness computed from multicycle indentation data.

Conversely, the hardness tendency is analyzed also by applying the Chicot's proposal [104] based in the strain gradient plasticity model suggested originally by Nix and Gao [45]. Figure III.1-8 shows the representation of the square of the Martens hardness (HM^2) as a function of the inverse of the maximum indentation depth ($1/h_{\max}$) and the estimation of data by applying the proposal developed in Chicot's work [104] by modifying the model of Nix and Gao [45]. It is observed in this case that values of the Martens macrohardness (HM_0) agrees with those ones computed by the model of Li and Bradt [103]. Additionally, the value of the hardness length-scale factor (H_{LSF}) was found to be 100 MPa.m$^{1/2}$. This value, as it was stated in previous researches, could be interpreted as a plastic deformation toughness of the material due to the strain gradients [104, 105, 106]. Moreover, it is possible to verify that the hardness length-scale factor and the depth-dependence parameter are related by the expression $H_{LSF} = HM_0\sqrt{h^*}$ as it was denoted by Chicot [104]. The difference between the Martens macrohardness computed by applying the two models is less than 1%. Moreover, the two models are related as function of the hardness length-scale factor, the Martens macrohardness and the depth-dependency parameter. The influence of each cycle on the test can be described by using the both model of Li et Bradt [103] or Nix and Gao [45] related by the hardness length-scale factor suggested by Chicot [104]. The value of the Martens macrohardness also agrees with those reported in the literature for this material [107, 108, 109]. Table III.1-2 collects the parameters from both models applied to the carbon steel samples.

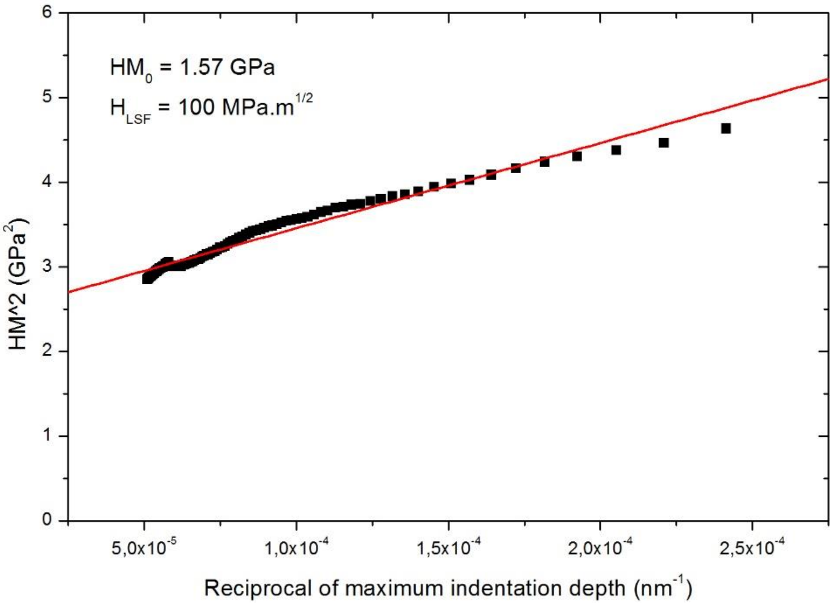

Figure III.1-8. Square of Martens hardness (HM^2) versus the reciprocal of the maximum indentation depth ($1/h_{\max}$) for the SAE 1045 carbon steel sample by applying the strain gradient plasticity model to hardness from multicycle indentation data.

Table III.1-2. Hardness of carbon steel samples (mean values) described by the models of Li et Bradt [103] and Chicot [104] describing the indentation size effect from the continuous multicycle indentation test data.

	Li et Bradt's model [103]		Chicot's Model [45]	
Sample	HM_0 (GPa)	$\Delta_{\mathrm{L-B}}$ (MPa·m)	HM_0 (GPa)	H_{LSF} (MPa·m$^{1/2}$)
SAE 1020	2.01	2.70	2.00	110
SAE 1045	1.60	2.35	1.58	93
SAE P20	2.84	2.40	2.82	118

III.1.2. Reduced elastic modulus from the nanoindentation experimental contact stiffness

III.1.2.1. Introduction

In the current section, the contact area functions proposed by Oliver and Pharr [1] and Chicot *et al.* [27] are analyzed with the aim of establish a method to improve the evaluation of the contact area between the material surface and the indenter by obtaining, additionally, the elastic property of the examined material. A non-linear least square analysis is advanced to estimate in the same computation process: the contact area (A_{C}) and the reduced elastic modulus of the material (E_{R}). The application of the advanced model is effectuated to the acquired data by nanoindentacion tests performed on fused silica and carbon steel samples.

III.1.2.2. Models representing the contact area

The contact area function is inspected for sake of establish an innovative method to assess it. To accomplish this objective, first, the experimental contact stiffness S from the upper part of the unloading curve is related according with previous researches [110, 111] with the reduced elastic modulus and the contact area by the following expression:

$$S = \frac{dP}{dh} = \frac{2}{\sqrt{\pi}} E_R \sqrt{A_{\mathrm{C}}} \qquad \text{(III.1-3)}$$

Where S is the experimentally measured contact stiffness by the instrument, E_R is the reduced modulus of the system (material-indenter), and A_{C} is the area of the contact between the indenter and the specimen surface. From Eq. (III.1-3), it can be stated that both contact area and reduced elastic modulus are directly proportional to the experimental contact stiffness, in others words, if elastic modulus of the material is considered independent of indentation contact depth (and, consequently the reduced elastic modulus too) then any change in the contact stiffness relies in some variation of the contact area, as it has been point out in previous works [1, 17, 12]. The analysis to suggest a novel proposal of computation of the contact area has been carried out on different materials: SAE 1020, SAE 1045, SAE P20 carbon steels and fused silica.

As mentioned above, a further analysis of relation (III.1-3) is carry out using the contact area functions proposed by Oliver and Pharr [1], Troyon and Huang [21] and more recently the one proposed by Chicot *et al.* [27], additionally, incorporating the contact indentation depth suggested by Bec *et al.* [11] in order to estimate the contact area regarding the pile-up effect occurring in some materials. Considering the measured contact stiffness acquired by the nanoindentation instrument, a non-linear least square regression analysis is effected with a view to estimate both the contact area and the reduced elastic modulus from the achieved test, where the value of the contact stiffness (S) is known and the reduced elastic modulus is taken as a fitting parameter as well as the different parameters of the contact area functions according to the following considerations: The Oliver and Pharr's contact area function with the alluded eight parameters and the contact indentation depth (h_C) defined as it was expressed in the Oliver and Pharr's proposition [1] where the sink-in is considered as the expected mechanical response of materials under analysis; afterwards, the eight-parameters-contact-area function is again implemented but changing the definition of the contact indentation depth (h_C) by the one proposed by Bec *et al.* [11] which considers the influence of the pile-up phenomenon on the underestimation of the contact area and, consequently, on the overestimation of the mechanical properties of the materials, *i.e.* the elastic modulus and hardness. Table III.1-3 collects the contact area functions to be implemented to as to perform the explained analysis above.

Table III.1-3. Contact area functions advanced by Oliver and Pharr [1] and Chicot *et al.* [27]

Contact area (A_C)	
$\sqrt{A_\mathrm{C}} = \sqrt{24.5{h_\mathrm{C}}^2 + C_1 h_\mathrm{C} + C_2 {h_\mathrm{C}}^{\frac{1}{2}} + \cdots + C_8 {h_\mathrm{C}}^{\frac{1}{128}}}$	(III.1-4)
Oliver and Pharr [1]	
$\sqrt{A_\mathrm{C}} = \left(\sqrt{\pi}\tan\psi\right)\left[h_\mathrm{C} + h_b\left(1 - \exp\left(-2\frac{h_\mathrm{C}}{h_b}\right)\right)^{3/2}\right]$	(III.1-5)
Chicot et al. [27]	
$\sqrt{A_\mathrm{C}} = \left(\sqrt{\pi}\tan\psi\right)\left(h_\mathrm{C} + h_b\right)$	(III.1-6)
Troyon and Huang [21]	

As it can see, the contact area functions are the one proposed by Oliver and Pharr [1], with eight fitting parameters ($C_1, \cdots, C_8$), the one suggested by Chicot *et al.* [27] and the one suggested by Troyon and Huang [21] with only one fitting parameter.

From Eq. (III.1-3), the contact stiffness is estimated using the three contact area functions, from Eqs. (III.1-4) to (III.1-6), presented in Table III.1-3 and for the assessment of this contact area, and therefore on the mechanical properties of materials, the corresponding indentation contact depth considering the effect of the sink-in (Eq. (III.1-7)) [1] and the pile-up (Eq. (III.1-8)) [11] phenomena:

$$h_{\mathrm{C}} = h_{\max} - \varepsilon \frac{P_{\max}}{S} \tag{III.1-7}$$

$$h_{\mathrm{C}} = 1.2\left(h_{\max} - \frac{P_{\max}}{S}\right) \tag{III.1-8}$$

III.1.2.3. Estimation of reduced modulus from the experimental contact stiffness

According with the scheme of analysis presented in the earlier section, the contact area functions are replaced into Eq. (III.1-3). After, a non-linear least square regression analysis is achieved in order to assess the corresponding fitting parameters. On the one hand, using the contact area function proposed by Oliver and Pharr, the fitting parameter are nine, eight from the contact area function ($C_1, \cdots, C_8$) and the other one is the reduced elastic modulus of the system under analysis (E_{R}). On the other hand, applying the contact area function suggested by Chicot *et al.* [27] or Troyon and Huang [21], the fitting parameter are only two: the blunt defect of the indenter tip (h_{b}) and the reduced elastic modulus of the system (E_{R}).

When the contact area function proposed by Oliver and Pharr [1] is implemented, the non-linear least square fitting analysis is setting to compute not negative values for the fitting parameters of the contact area and the reduced elastic modulus, additionally, the first coefficient (coefficient of ${h_C}^2$) of the contact area function is fixed to be equal to 24.5 to agree with the face angles defined by pyramidal indenter and to avoid local maxima or minima for a large depth range [17]. With this restriction the used fitting assures a smooth area function and a better extrapolation of data, if this last one is required. When the function proposed by Chicot *et al.* [27] and the one advanced by Troyon and Huang [21] are applied, the fitting parameters (the reduced modulus and the blunt defect of the indenter tip) are set to be not negative values.

III.1.2.4. Study Case: The silica

The data acquired from CSM tests performed over a fused silica sample are used to compare and validate the values of the estimated reduced elastic modulus by applying the analysis described in the above section.

Figure III.1-9 illustrated the comparison between the contact stiffness by replacing the models presented by Oliver and Pharr [1], Troyon and Huang [21], and more recently the model proposed by Chicot *et al*. [27]. It can be observed that the differences between the three models representing the experimental contact stiffness is not very large, indeed, the four plots are almost overlapped between them, considering that the computation of the contact stiffness using the Chicot *et al*.'s contact area function [27] agree with the estimation done by replacing the contact area model developed by Oliver and Pharr [1] or the one proposed by Troyon and Huang [21] in Eq. (III.1-3). As it can be seen, the Troyon and Huang's approach [21] could be applied to perform the analysis to estimate the experimental contact stiffness, nevertheless, as their authors proposed, this model is normally evaluated when the indentation contact depths are greater than approximately 200 nm. But, the model presented by Chicot *et al*. [27] is advantaged because it can be applied in the same range of the former and, moreover, for lower values of contact indentation depth.

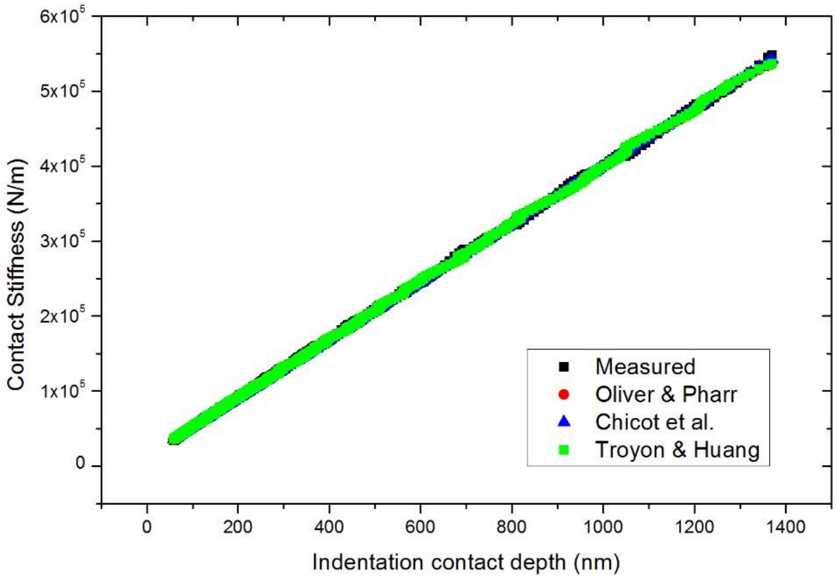

Figure III.1-9. Comparison of the experimental contact stiffness computed from the contact area functions advanced by Oliver and Pharr [1], Troyon and Huang [21] and Chicot *et al*. [27] considering $100 < h_{\max} < 1900$ nm

Moreover, Figure III.1-10 shows the fraction difference on the estimation of the contact stiffness by using the contact area function proposed by Oliver and Pharr, Troyon and Huang, and Chicot *et al*. It is noticeable that when using the contact area functions presented by Chicot *et al*. [27], Troyon and Huang [21], the fraction difference for low values is greater than using the contact area function proposed by Oliver and Pharr [1]. Nevertheless, when the indentation contact depth is greater than approximately 200 nm, the estimation of the contact stiffness differs in less of 3% with respect to the measured contact stiffness, a lower fraction difference than the values obtained when the analysis is based on the Oliver and Pharr's contact area function or in the one advanced by Troyon and Huang.

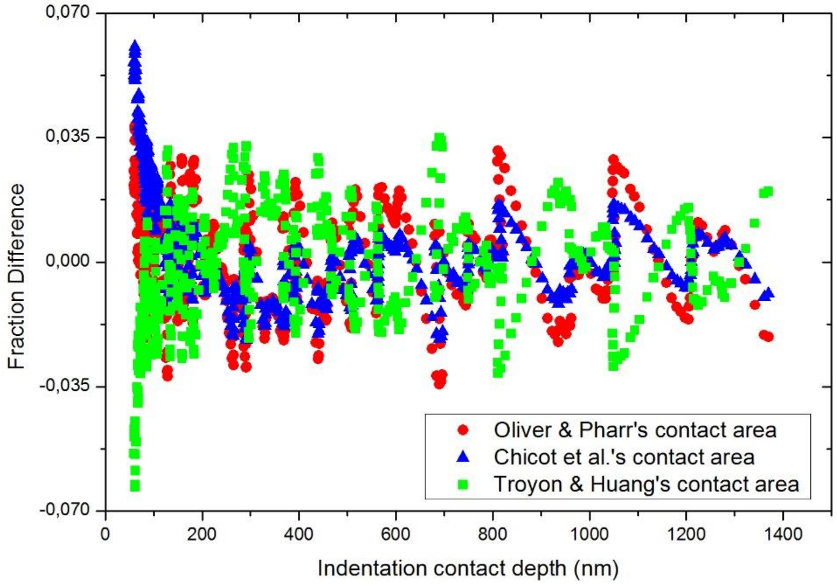

Figure III.1-10. Fraction difference between the experimental contact stiffness and the predicted one evaluated from the Oliver and Pharr' contact area function [1], the one advanced by Troyon and Huang [21] and the one proposed by Chicot *et al*. [27] considering $100 < h_{\max} < 1900$ nm.

However, as it can be noted in Figure III.1-11 at low loads, *i.e.* at low indentation depths, the dissimilarity between the two models are remarkable. It is interesting to observe that introducing in Eq. (III.1-3) the model proposed by Chicot *et al*. [27] applied to the estimation of the contact stiffness, it adjusts in a better way the experimental contact stiffness than replacing the contact area function proposed by Oliver and Phar [1] and the approach presented by Troyon and Huang [21], in others words, replacing the contact area function suggested by Chicot *et al.* into Eq. (III.1-3) allows to obtain a pertinent value of the contact stiffness compared with the experimental one, and accordingly an appropriate value of the reduced elastic modulus of the system.

Furthermore, in Figure III.1-12 is possible to observe that the difference between the estimation of the contact stiffness by using the three described models is approximatively more than 40% with respect to the measured contact stiffness when the indentation depths are lower than 10 nm approximately, and after both models agree with the experimental contact stiffness with a fraction difference less than 5%.

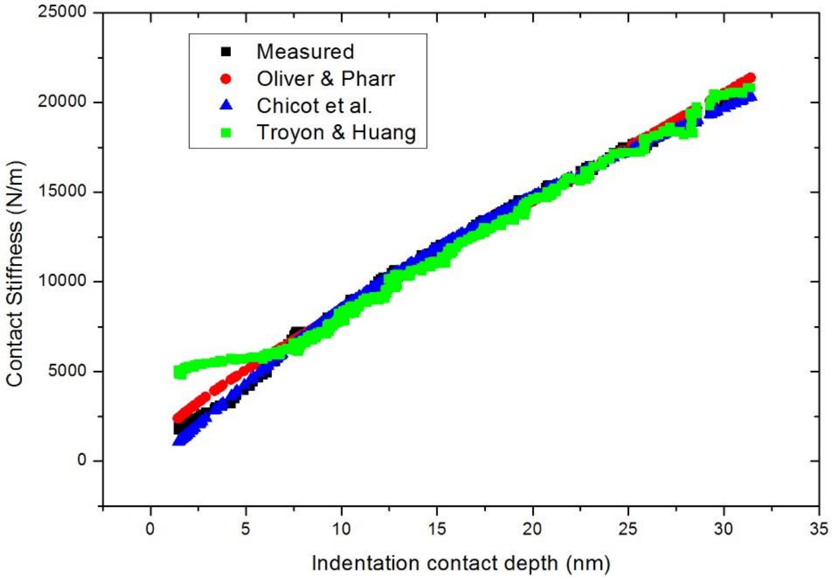

Figure III.1-11. Comparison of the contact stiffness by replacing the contact area function defined by Oliver and Pharr [20], Troyon and Huang [21] and Chicot *et al*. [27] in Eq. (III.1-3) and considering $4 < h_{\max} < 50$ nm.

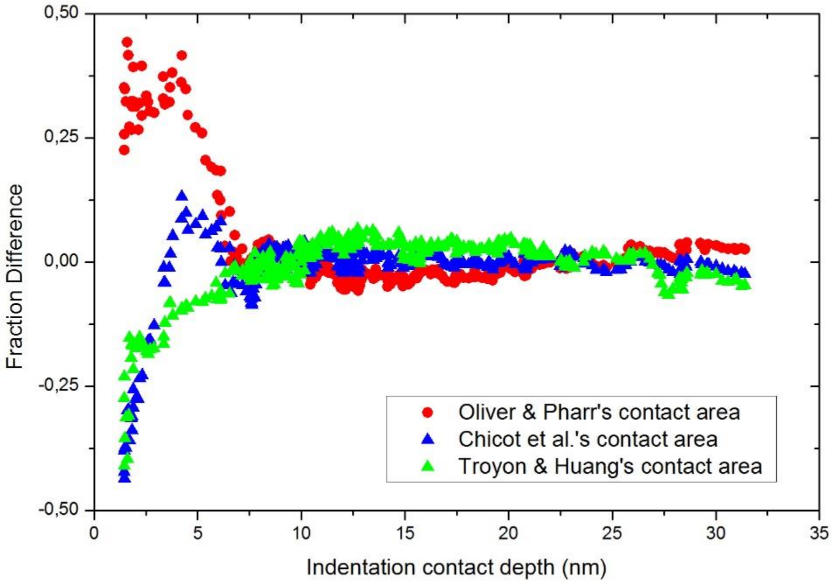

Figure III.1-12. Fraction difference between the experimental contact stiffness and the contact stiffness evaluated from the contact area functions of Oliver and Pharr [20], Troyon and Huang [21] and Chicot *et al*. [27] considering $4 < h_{\max} < 50$ nm. Contact stiffness models work better at depths greater than 10 nm.

It is important to highlight that for the two range of analysis illustrated in Figure III.1-9 and Figure III.1-11, two different non-linear least square fitting procedure were accomplished. It is clear that the extrapolation of the data from the higher range to the lower range could result in wrong estimation of the elastic modulus of the material. Table III.1-4 shows the computed values by using the nanoindentation test from a fused silica sample and applying the fitting process with considering the maximum indentation depth in the range $100 < h_{\max} < 1900$ nm. Comparing the value of the elastic modulus of the material it can be stated that the difference between the two applied models is less than 1%, and additionally, the values of the blunt defect of the indenter tip (h_{b}) were obtained when the model of Chicot *et al.* [27] was implemented.

Table III.1-4. Elastic modulus and reduced elastic modulus of fused silica by replacing the models of contact area proposed by Oliver and Pharr [1], Troyon and Huang [21] and Chicot *et al.* [27] into Eq. (III.1-3) between $100 < h_{\max} < 1900$ nm.

	Applying (III.1-4) and (III.1-7)		Applying (III.1-5) and (III.1-7)			Applying (III.1-6) and (III.1-7)		
	E_R(GPa)	E (GPa)	E_R(GPa)	E (GPa)	h_{b} (nm)	E_R(GPa)	E (GPa)	h_{b} (nm)
Average	70.0	67.9	70.4	68.2	30.5	70.4	68.2	30.3
Standard Deviation	0.3	0.3	0.3	0.3	1.9	0.3	0.3	1.8

Conversely, when the same non-linear regression analysis is performed but using the indentation data in the range $4 < h_{\max} < 50$ nm instead, some important differences arise. Table III.1-5 shows the value obtained under this last condition. It can be observed that by replacing in Eq. (III.1-3) the contact area functions advanced by Oliver and Pharr [1] and Troyon and Huang [21], the difference on the estimation of the elastic modulus is greater than 50%, nevertheless, although the estimation of the contact stiffness by replacing the Chicot *et al.*'s contact area function [27] in Eq. (III.1-3) is less than 11% with respect to the previous estimated value. This large difference, in somehow, were expected above all when replacing the contact area function proposed by Oliver and Pharr owing to the absence of non-positive coefficients which introduce a significant accuracy error in the estimation of the contact area above all when the data at low loads is analyzed. Additional, it is noticeable the large change in the estimation of the blunt defect of the tip between the two range of analysis when the contact area function suggested by Troyon and Huang [21] is implemented.

Furthermore, to verify the application of the model of Chicot *et al.* [27] by replacing it in Eq. (III.1-3) and to estimate the reduced elastic modulus of others specimens, three samples of carbon steels were used so as to compute and compare their elastic modulus by studying it when replacing the three models presented in Table III.1-3 into Eq. (III.1-3).

Table III.1-5. Elastic modulus and reduced elastic modulus of fused silica by replacing the models of contact area proposed by Oliver and Pharr [1], Troyon and Huang [21] and Chicot *et al.* [27] into Eq. (III.1-3) considering $4 < h_{\max} < 50$ nm.

	Applying (III.1-4) and (III.1-7)		Applying (III.1-5) and (III.1-7)			Applying (III.1-6) and (III.1-7)		
	E_R(GPa)	E (GPa)	E_R(GPa)	E (GPa)	h_b (nm)	E_R(GPa)	E (GPa)	h_b (nm)
Average	105.4	105.6	77.2	75.5	19.2	110.0	110.8	4.0
Standard Deviation	4.7	5.2	12.0	12.9	8.9	7.3	7.9	2.8

III.1.2.5. Study Case: Carbon Steels

The three carbon steels described in chapter 2 are analyzed to obtain their elastic modulus by replacing the contact area function proposed by Oliver and Pharr [1] and Chicot *et al.* [27] in Eq. (III.1-3). Regarding the results from the samples of SAE 1020, SAE 1045 and SAE P20 showed in Table III.1-6, Table III.1-7 and Table III.1-8, respectively, it is interesting to note that the elastic modulus computed by considering the pile-up effect around the indenter is the one which can be an acceptable value from the elastic modulus of the three samples. When the sink-in effect is taken into account the assessed values of the elastic modulus tends to be overestimated. Moreover, the standard deviation computing the value of the elastic modulus is less than 8% and less than 15% for the estimation of the blunt defect of the indenter tip when the Chicot *et al.*'s contact area function is applied.

Table III.1-6. Elastic modulus and reduced elastic modulus of SAE 1020 by replacing the contact area models proposed by Oliver and Pharr [1] and Chicot et al. [27] into Eq. (III.1-3)

	Applying Eqs. (III.1-4) and (III.1-7) (Sink-in)		Applying Eqs. (III.1-4) and (III.1-8) (Pile-up)		Applying Eqs. (III.1-5) and (III.1-8) (Pile-up)			Applying Eqs. (III.1-5) and (III.1-7) (Sink-in)		
	E_R (GPa)	E	E_R (GPa)	E	E_R (GPa)	E	h_{b} (nm)	E_R (GPa)	E	h_{b} (nm)
Average	222.9	252.0	174.8	187.7	187.7	188.4	37.9	207.4	230.5	29.9
Standard Deviation	9.3	13.2	4.4	5.6	5.6	5.6	8.0	5.3	7.2	6.6

Table III.1-7. Elastic modulus and reduced elastic modulus of SAE 1045 using the contact area approches proposed by Oliver and Pharr [1] and Chicot *et al*. [27] into Eq. (III.1-3)

	Applying Eqs. (III.1-4) and (III.1-7) (Sink-in)		Applying Eqs. (III.1-4) and (III.1-8) (Pile-up)		Applying Eqs. (III.1-5) and (III.1-8) (Pile-up)			Applying Eqs. (III.1-5) and (III.1-7) (Sink-in)		
	E_R	E	E_R	E	E_R	E	h_b	E_R	E	h_b
	(GPa)		(GPa)		(GPa)		(nm)	(GPa)		(nm)
Average	218.3	245.6	177.2	190.8	177.9	191.7	45.4	210.5	234.7	36.1
Standard Deviation	10.3	14.2	6.5	8.3	6.2	7.9	17.8	7.4	10.1	14.5

Table III.1-8. Elastic modulus and reduced elastic modulus of SAE P20 replacing the contact area functions proposed by Oliver and Pharr [20] and Chicot *et al*. [21] into Eq. (III.1-3)

	Applying Eqs. (III.1-4) and (III.1-7) (Sink-in)		Applying Eqs. (III.1-4) and (III.1-8) (Pile-up)		Applying Eqs. (III.1-5) and (III.1-8) (Pile-up)			Applying Eqs. (III.1-5) and (III.1-7) (Sink-in)		
	E_R	E	E_R	E	E_R	E	h_b	E_R	E	h_b
	(GPa)		(GPa)		(GPa)		(nm)	(GPa)		(nm)
Average	226.7	257.2	202.7	224.1	195.7	214.8	28.3	225.3	255.2	24.8
Standard Deviation	5.0	7.0	3.6	4.8	5.0	6.6	5.2	4.8	6.8	6.8

According to the figures presented in Table III.1-6, Table III.1-7 and Table III.1-8 the standard deviation of the elastic modulus of the material computed by this procedure is less than 5% when considering the pile-up effect, it means, when equations Eqs. (III.1-4) and (III.1-8), or Eqs. (III.1-5) and (III.1-8), are replaced into the Eq. (III.1-3) to estimate the contact stiffness by a non-linear regression analysis and fitting by means of this expression the parameters of the contact area function and the reduced elastic modulus of the tested material.

III.1.2.6. Discussion

Considering the non-linear least square analysis for the samples of fused silica and carbon steels SAE 1020, SAE 1045 and SAE P20, it is possible to observe that the estimation of the elastic modulus depends principally on the definition of the contact area, but also it depends on the mode of deformation of the material around the indenter, *i.e.* phenomena of sink-in and pile-up. According with the results presented in Table III.1-6, Table III.1-7 and Table III.1-8 the values of the elastic modulus computed by replacing the Oliver and Pharr's contact area function (used widely in the assessment of mechanical properties by instrumented indentation) into the explicit function of the contact stiffness and considering the effect of the pile-up around the indenter, agree with those reported in the literature [102, 112, 7].

Concerning the values of the elastic modulus from the fused silica sample, it agrees with values reported in several studies [1, 12, 68] . The estimation of the elastic modulus by using the contact area suggested by Oliver and Pharr and considering the eight-coefficients-contact-area function and the reduced elastic modulus as fitting parameters shows that the obtained value agrees with ones reported in the literature. However, the assessment of the elastic modulus of this material agrees also when the contact area proposed by Chicot *et al.* [27] is applied. When this model is used, the fitting parameters are the blunt defect of the indenter tip (h_{b}) and the reduced elastic modulus of the system (E_{R}). It is relevant to highlight that the standard deviation resulting of applying the both models is less than 5% which demonstrates the convergence of the non-linear least square analysis when using this procedure.

It is also interesting to note that applying the contact area function proposed by Chicot *et al.* [27] the value of the blunt defect of the tip indenter can be estimated. When it is performed with the acquired data from the fused silica the value estimated equals to 30.5 ± 1.9 nm when large indentation depths are used to fit the data, and 19.2 ± 8.9 if the lower indentation displacements are used to perform the non-linear regression analysis. Concerning the estimation of this value for the others samples, the value is in the same order of magnitude as it is expected and the difference between them can be associated to the perturbation that could arise at this nanoscale range of measure. From a general point of view, it can be stated that the estimation of the contact stiffness by replacing the contact area function proposed by Chicot *et al.* [27] and the one suggested by Oliver and Pharr [1], into the explicit relation (III.1-3) is consistent, but it is necessary to discriminate the deformation mode occurring around the indenter, it means, the pile-up or sink-in influence must not be neglected.

III.1.3. Conclusions

Mechanical properties of carbon steel samples, *i.e.* hardness and elastic modulus, were evaluated from continuous multicycle indentation tests at microscale range. Concerning the values obtained at every single cycle, it can be affirmed that the elastic modulus remains constant as the number of cycles increases until 100. The damage is not obvious. Moreover, by implementing the proposition suggested by Yetna *et al.* [100], the predominant deformation mode around the indenter was found to be the pile-up phenomenon, by means of the parameter Δ which remains greater than 0.83 for all continuous indentation tests. Accordingly, the elastic modulus of the carbon steel samples was found to be

© 2016 Tous droits réservés. lilliad.univ-lille.fr

between 158 and 190 GPa with a standard deviation around 5%. Regarding the hardness behavior, it was described by applying the Li and Bradt's model [103] and the model advanced by Chicot [104] when tests are performed in the microscale range. In both cases, the slight variations of the material hardness under the increasing loadings by continuous multicycle indentation tests were associated to the indentation size effect. Comparing the obtained Martens macrohardness by applying both models to all samples, it can be said that they agree each other with the obtained value for the materials no matter what model is implemented. The Martens hardness for the three carbon steel samples were found to be approximately between 1.6 and 2.8 GPa.

On the other hand, by analyzing the data acquired by indentation tests at nanoscale range and examining the previous suggested models to estimate the elastic modulus from the load-displacement curve obtained by the CSM test, the model advanced in this work to compute the contact stiffness by replacing the contact area proposed by Chicot *et al*. [27] agrees with the one suggested by Oliver and Pharr [1] when they are replaced into the explicit expression of the contact stiffness. Moreover, when a fused silica sample is examined by this method, the two derived expressions from the approach overlapped practically each other if they are effected in the range of $100 < h_{\max} < 1900$ nm. Conversely, by replacing the models of the contact area and applying a non-linear least square analysis in the range $5 < h_{\max} < 50$ nm, the contact area function proposed by Chicot *et al*. [27] describes better the values of the experimental contact stiffness than the model suggested by Oliver and Pharr [1]. Furthermore, by effectuating this novel proposal by using the data obtained by nanoindentation tests from a fused silica sample and replacing the expression of the contact area function advanced by Chicot *et al*. [27], the blunt defect of the indenter tip was found to be 30.5 ± 1.9. Accordingly, by following this innovative procedure, the elastic moduli from carbon steel samples were computed and it was concluded that the deformation around the indenter (sink-in or pile-up effect) must be taken into account when the estimation of this elastic property is achieved. The elastic modulus from these carbon steel samples were found to be between 188 and 214 GPa.

III.2. MECHANICAL PROPERTIES BY MULTICYCLE INDENTATION TEST FROM HETEROGENEOUS SAMPLES

III.2.1. Introduction

Mechanical properties of solution precursor plasma sprayed hydroxyapatite (SPPS-HA) coatings are examined using instrumented indentation tests by applying a continuous multicycle (CMC) protocol. The mechanical properties are determined by means of indentation experiments in the microscale range in order to limit the influence of the heterogeneities of the microstructure as well as the roughness over the coating surface for which the effects are predominant in the nanoscale range. Elastic modulus and hardness of the SPPS-HA coatings are compared to the mechanical characteristics of HA coatings plasma sprayed using powder and suspension feedstocks. The microstructural influence, specifically, the role of morphology and crystallinity of the SPPS-HA coatings on mechanical properties is illustrated and discussed regarding the application of some models related to this aspect. As well, a new approach is advanced to evaluate the effect of the densification process occurring in the porous structure of the hydroxyapatite coating samples on hardness behavior during the indentation process as a function of the indentation depth. Furthermore, the results obtained from the models allow to predict the elastic modulus and hardness of the SPPS-HA coatings as a function of the crystallinity volume fraction.

III.2.2. Microstructure of hydroxyapatite coating samples

The process parameters influencing the morphology of coatings have a significant effect on mechanical properties of SPPS-HA coatings. Figure III.2-1 and Figure III.2-2 illustrate the micrographs of a representative sample labeled as “H-2” that it was prepared using high solution concentration where the microstructural features such as fine particles and agglomerated fragmented shells distributed at the surface of the coatings are visible (see in particular Figure III.2-2). The image at the cross-section of the coating shows a relatively dense and very well adhered coating (and generally, for those one sprayed using the high solution concentration) with the presence of some pores.

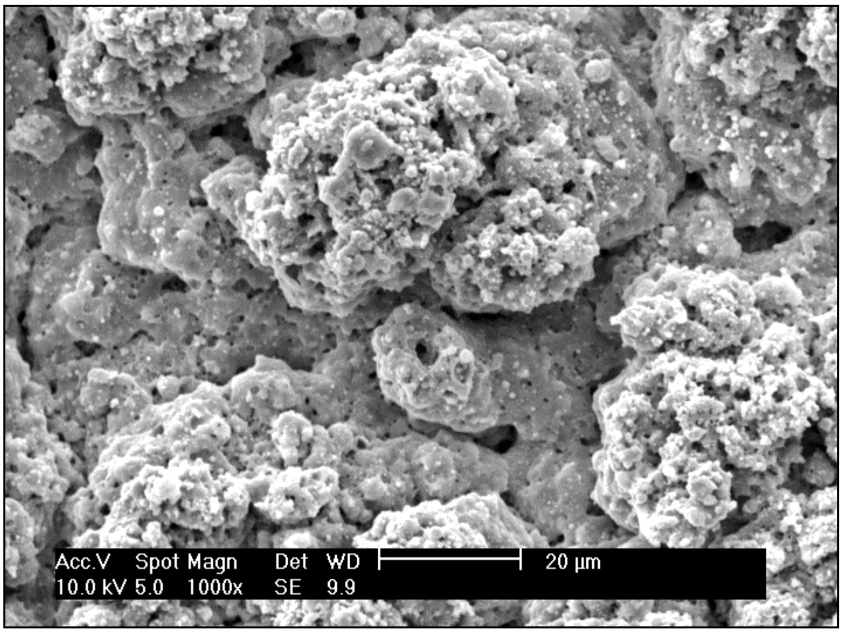

Figure III.2-1. SEM micrograph of sample H-2 (high solution concentration) at the surface of the hydroxyapatite coating sample.

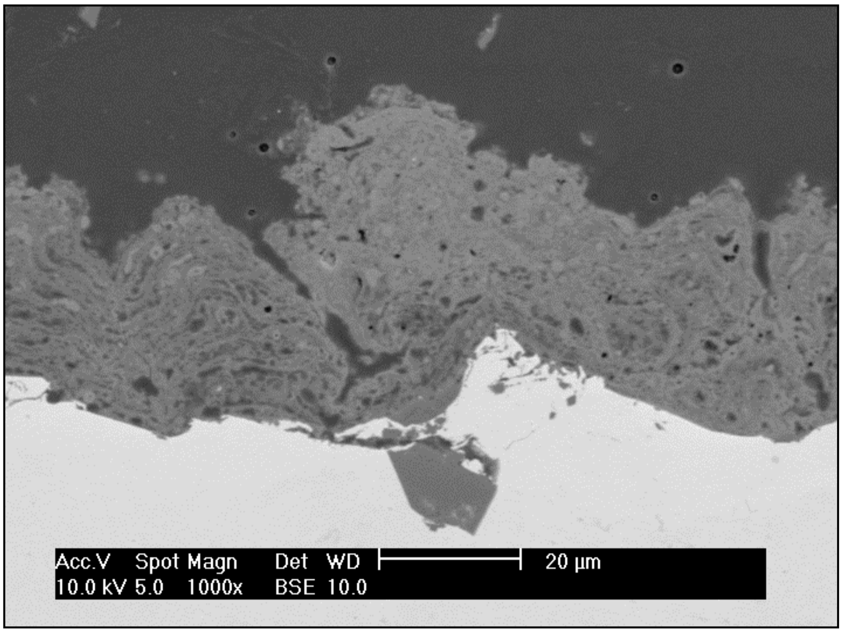

Figure III.2-2. SEM micrograph of sample H-2 (prepared with a high solution concentration) at the cross-section of the hydroxyapatite coating sample.

Conversely, Figure III.2-3 and Figure III.2-4 show the SEM images from sample labeled “L-3” prepared using the low solution concentration. It can be noted that the coating has a dome-like morphology as viewed on the surface. The cross-section (Figure III.2-4) of this coating shows a column-like microstructure that can be considered as a cone-shaped defect typical for liquid feedstock spraying. This illustration is particularly interesting owing to the amorphous nature of sample L-3 that could influence significantly its mechanical properties such as its hardness.

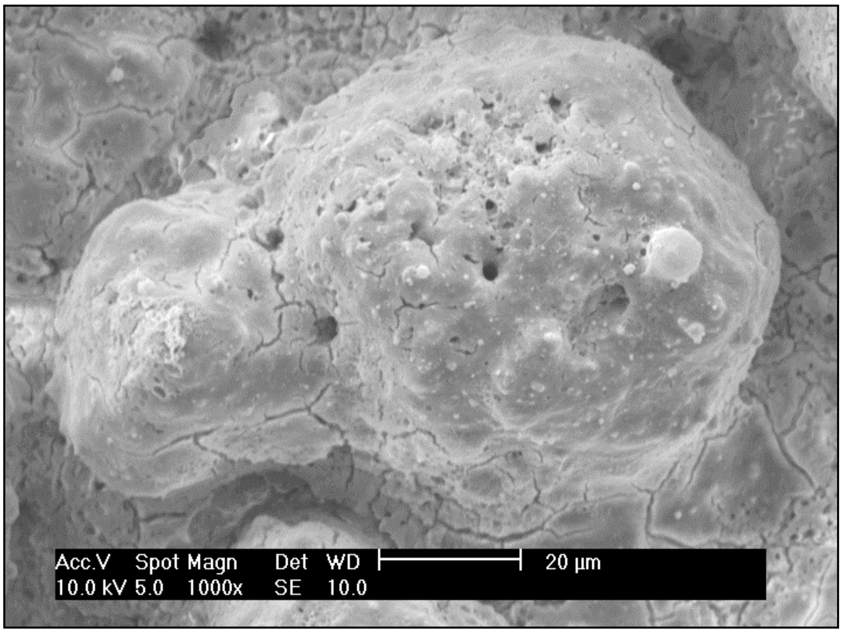

Figure III.2-3. SEM micrograph of sample L-3 (prepared with a low solution concentration) at the surface of the hydroxyapatite coating sample.

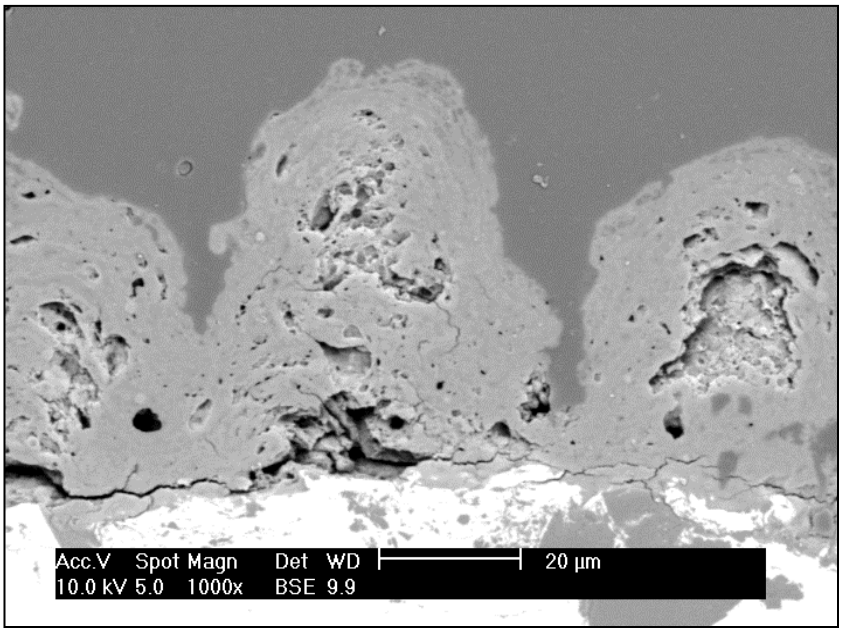

Figure III.2-4. SEM micrograph of sample L-3 (prepared with a low solution concentration) at the cross-section of the hydroxyapatite coating sample.

Regarding the XRD diagram shown in Figure III.2-5, it can be established the percentage of crystallization of samples prepared using high and low solution concentration. From this ones, and plotting the diagrams corresponding to the H-2 and L-3 samples, it can be stated that the samples formed with the high solution concentration have a higher grade of crystallinity than the ones produced with the low concentration solution.

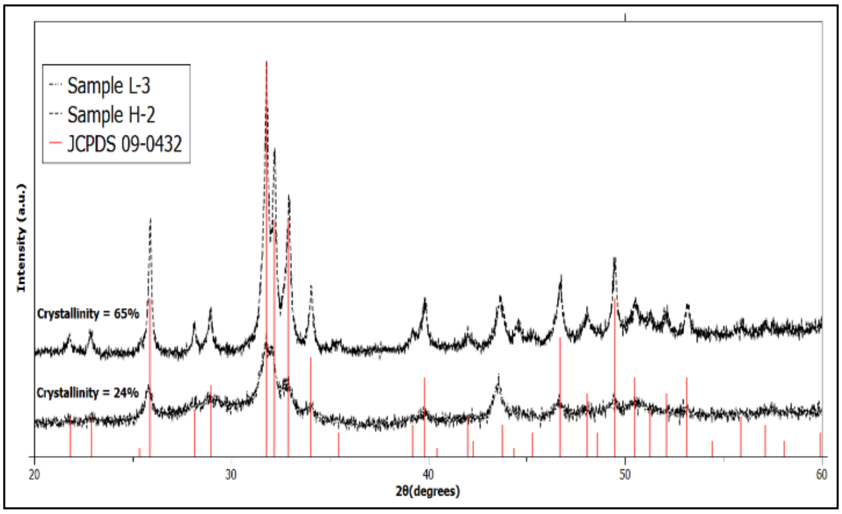

Figure III.2-5. XRD diagram of selected coatings prepared using high concentration (H-2) and low concentration (L-3) of solution precursors indexed to standard diffraction file of HA.

III.2.3. Surface condition of hydroxyapatite coatings

To take into account the surface condition of each sample into the analysis, Table II.2-1 collects the roughness and thickness from the hydroxyapatite coatings deposited on a stainless steel substrate. It can be observed from this table that the thickness of coating is around 50 µm and the surface roughness is higher on the samples sprayed with a high solution concentration than the samples produced with a low solution concentration.

Table III.2-1. Surface roughness and thickness of the sprayed Hydroxyapatite coating samples.

	High initial solution concentration				Low initial solution concentration			
Sample code	H-1	H-2	H-3	H-4	L-1	L-2	L-3	L-4
R_a (µm)	8.8	8.2	10.9	8.4	10.9	10.4	18.1	15.5
Standard deviation	0.9	0.5	0.3	0.8	0.7	0.7	0.9	1.0
Thickness (µm)	51	48	45	47	41	43	53	49
Standard deviation	8	7	4	5	3	5	3	4

III.2.4. Mechanical properties from continuous multicycle Indentation tests.

III.2.4.1. Application of continuous multicycle indentation tests

The hydroxyapatite coating samples described in chapter 2 and illustrated previously in this section were submitted to a continuous multicycle indentation tests. The experimentation was design to reach 100 cycles, between the initial load for the first cycle equals to 1 N and the load of the last cycle equals to 20 N. The load-displacement curve from the multicycle indentation test is illustrated in Figure III.2-6.

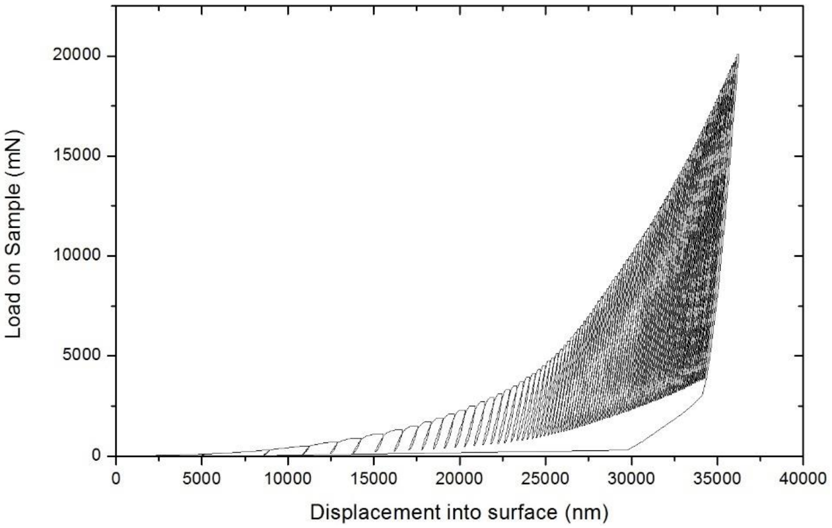

Figure III.2-6. Load-displacement curve from a continuous multicycle indentation tests between 1 N and 20 N performed on a SPPS-HA coating sample.

To establish the mechanical response around the indenter, Yetna *et al.*'s proposal [100] is implemented. The ratio $^{h_\mathrm{f}}/_{h_\mathrm{max}}$ is compute at every single cycle of the multicycle indentation test. According to their authors when the parameter Δ, defined by the ratio $\Delta = \frac{h_\mathrm{f}}{h_\mathrm{max}}$, is greater than 0.83 then the pile-up effect is present into the surface around the indenter, but if Δ is lower than 0.83 the sink-in phenomenon is the predominant mechanical response into the surface material around the indenter. Figure III.2-7 illustrates the ratio $^{h_\mathrm{f}}/_{h_\mathrm{max}}$ as a function of the maximum indentation depth, from this plot, it can be noted that this ratio is greater than 0.83 which means that the principal phenomenon around the indenter is the pile-up, and consequently, the indentation contact depth is defined by the proposal suggested by Bec *et al.* [11]; it is also important to mention that this ratio $^{h_\mathrm{f}}/_{h_\mathrm{max}}$ is a parameter depending on the material which defines the deformation mode of the material surface around the indenter.

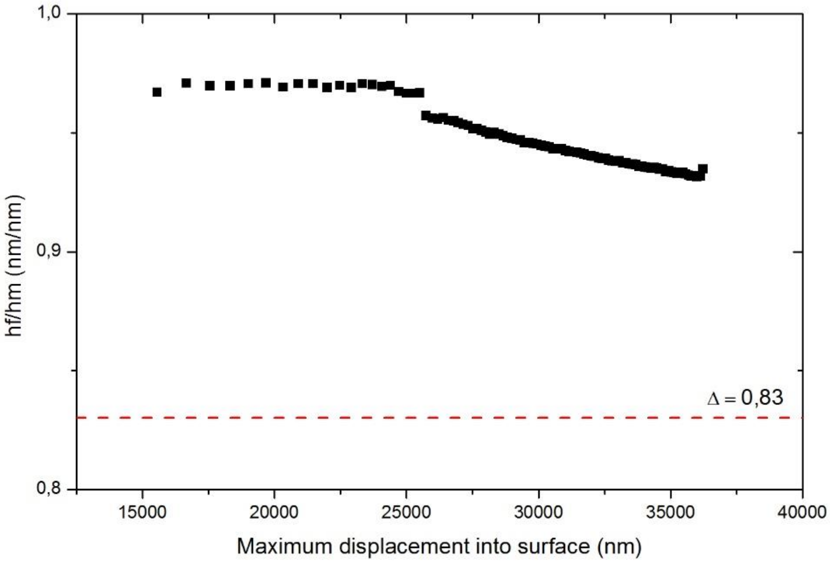

Figure III.2-7. Ratio of the residual depth to maximum indentation depth ($h_\mathrm{f}/h_\mathrm{max}$) from a SPPS-HA coating sample at each cycle evaluated by a continuous multicycle indentation test.

III.2.4.2. Hardness assessment from continuous multicycle indentation tests

Firstly, Martens hardness *(HM)* is considered for the evaluation of hardness of the SPPS-HA coatings. The Martens hardness is defined as the ratio between the maximum applied load *(P_max)* and the actual contact area *(A_m)* between the indenter and the material. This may be calculated by considering the maximum indentation depth reached by the indenter *(h_max)* in one and all cycles from the multicycle indentation test, and it can be expressed mathematically as follows:

$$HM = \frac{P_\mathrm{max}}{A_m} = \frac{P_\mathrm{max}}{26.43{h_\mathrm{max}}^2} \qquad \text{(III.2-1)}$$

In order to refine the computation of the actual contact area the indentation depth is corrected by adding the blunt defect of the indenter tip h_b, and the Eq. (III.2-1) is rewritten below:

$$HM = \frac{P_\mathrm{max}}{26.43(h_\mathrm{max} + h_\mathrm{b})^2} \tag{III.2-2}$$

Moreover, being the HA coatings deposited on a harder substrate, *i.e.* stainless steel, the values obtained by microindentation tests showed the influence of heterogenic distribution of pores in the hardness estimation illustrated in Figure III.2-8.

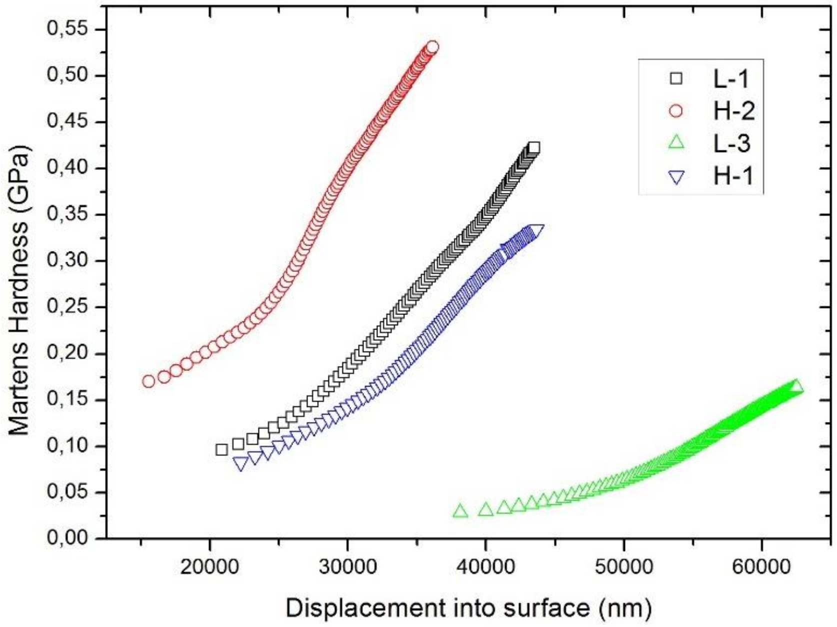

Figure III.2-8. Martens hardness computed from SPPS-HA coating samples by continuous instrumented indentation tests.

In assessing the hardness of the porous coating at the outermost and at the innermost layer of the coating, it is necessary to apply a mathematical model to describe this hardness variation as a function of the indentation contact depths. For that, it is suggested to develop a model of a typical S-curve, as for example, a model based on the same principle of the one originally proposed by Jönsson and Hogmark [67]. This model will be constructed on a linear mixture law between two limits as follows:

$$H_\mathrm{C} = a_\mathrm{P} H_\mathrm{P} + (1 - a_\mathrm{P}) H_\mathrm{D} \tag{III.2-3}$$

where H_C is the composite hardness, H_P is the hardness of porous (as received) coating, H_D is the hardness of the densified coating, and a_P represents the contribution of the porous portion of the coating material to the computed composite hardness owing to the compression exerted by the instrument beneath the indenter. To represent the S-curve behavior of the hardness as function of the indentation depth, it is proposed to write the volume fraction of the porous zone (a_P), as it follows:

$$a_\mathrm{P} = \begin{cases} 1 & \text{if } \left(\frac{\kappa}{h}\right) > 1 \\ 1 - \left(1 - \frac{\kappa}{h}\right)^2 & \text{otherwise} \end{cases} \qquad \text{(III.2-4)}$$

where κ is a fitting parameter depending on the material related to the densification process occurring throughout the multicycle indentation process, and h is the indentation depth recorded during the multicycle instrumented indentation test.

The advanced model by applying Eqs. (III.2-3) and (III.2-4) is adopted to describe the hardness comportment from the hydroxyapatite coatings submitted to continuous multicycle indentation test. Figure III.2-9 illustrates the implemented non-linear analysis regression to predict the hardness behavior from the hydroxyapatite coating samples as a function of the indentation depth from samples H-2 (high solution concentration) and L-3 (low solution concentration). This figure also shows the description of experimental data by a non-linear least square analysis using the linear mixture law described in Eqs. (III.2-3) and (III.2-4).

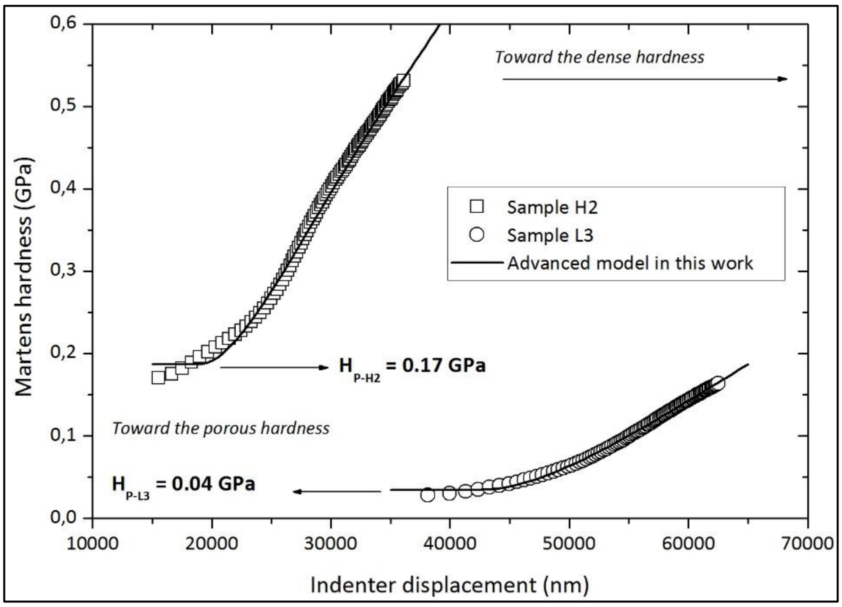

Figure III.2-9. Martens Hardness and the non-linear least square analysis using the suggested model described by Eqs. (III.2-3) and (III.2-4).

By applying the non-linear regression analysis to the acquired data from the continuous multicycle indentation tests, it was possible to obtain the hardness of the coating and substrate for every single test and sample. The mean value of the hardness of the SPPS-HA coatings and substrate together with their corresponding standard deviations are presented in Table III.2-2. The computed hardnesses from the porous coating based on the advanced model were between 0.04 to 0.17 GPa. The hardness of coatings developed by using the high solution concentration were higher compared to coatings prepared using a low solution concentration.

Table III.2-2. Hardness of porous and dense layers from the sprayed hydroxyapatite coatings.

Sample Code	Porous Hardness[a] (GPa)	Dense Hardness[a] (GPa)	Parameter κ (μm)
Using high initial concentration of solution precursor			
H-1	0.10 ± 0.01	1.9±0.6	27.8 ± 3.5
H-2	0.17 ± 0.02	2.2±0.4	23.2 ± 4.0
H-3	0.12 ± 0.03	1.7±0.2	24.6 ± 3.6
H-4	0.09 ± 0.02	1.2±0.2	42.5 ± 3.6
Using low initial concentration of solution precursor			
L-1	0.07 ± 0.03	1.5±0.2	25.9 ± 2.6
L-2	0.06 ± 0.01	1.7 ± 0.2	24.3 ± 3.9
L-3	0.04 ± 0.01	1.5±0.2	45.0 ± 4.1
L-4	0.04 ± 0.00	1.9±0.5	40.6 ± 3.4

[a] Mean (± standard deviation) calculated by the model proposed by Jönsson and Hogmark.

From the suggested model, applying Eqs. (III.2-3) and (III.2-4), the obtained values of the parameter κ are between 23.2 and 45.0 μm, which implies that the influence of the densification of material over the measured hardness by instrumented indentation begins when the indenter has reached around 50% to 85% of the measured coating thickness according to the values showed in Table III.2-2. It is interesting to observe the increasing value of the hardness from one cycle to another, illustrated in Figure III.2-9, by the phenomenon of densification occurring in this porous material during the multicycle indentation test. This influence is attributed to the modification of the porous network of HA coatings, the poor adhesion between the coating to the substrate (on the samples produced with a low solution concentration) as it can be seen in Figure III.2-4 and also to the fact that the very harder substrate of stainless steel prevents the volume displacement of the coating manifested by the pile-up behavior and the densification of the material under the indenter as it penetrates the coating.

III.2.4.3. Elastic modulus from continuous multicycle instrumented tests

To evaluate the elastic modulus of the material coating, the residual indentation depth to maximum indentation depth ratio was calculated first to determine the deformation mode according to Yetna *et al.*'s model [100]. The value of the parameter Δ has already been illustrated in Figure III.2-7. It was found that for all the coatings, this ratio was greater than 0.83, which implies that the pile-up phenomenon was the predominant behavior occurred on the surface of the material around the indenter. This pile-up behavior can be endorsed to the soft nature of HA coatings on a much harder stainless steel substrate that constrains the plastic deformation of the coating and also due to the heterogeneous nature of plastic deformation of this partially amorphous coating as it has been described in others researches [113, 114]. To have an idea on the penetration characteristic of the indenter into the surface of the coatings, electron micrographs were taken on the indented part of the coatings. Figure III.2-10 and Figure III.2-11 show the SEM images of representative samples H-2 and L-3, respectively, after the indentation experiment were effected. It is observed that the displaced deposits tend to flow-up resulting to what is called the phenomenon of pile-up. However, it is noted that sample L-3 was highly deformed by the indenter than sample H-2 which can be ascribed to the different morphological features of each coating.

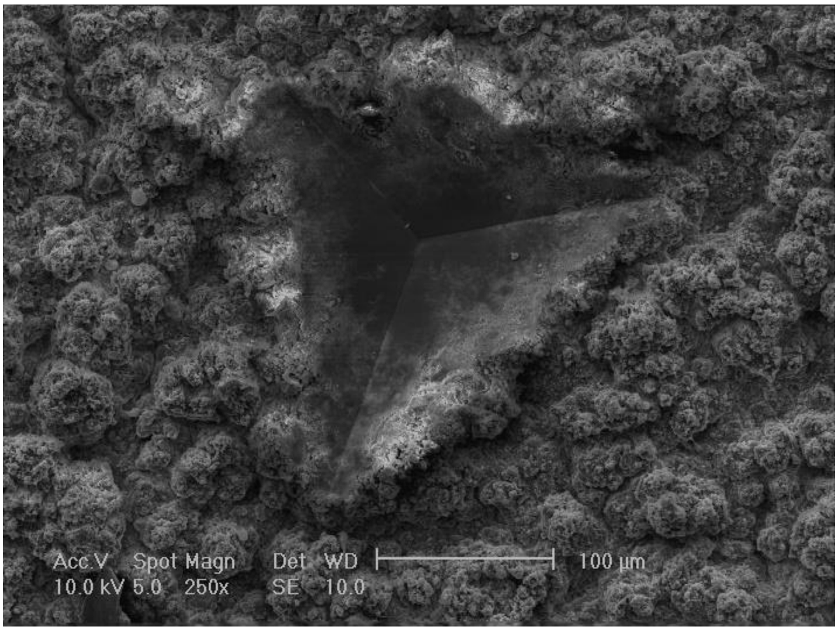

Figure III.2-10. SEM micrograph after a multicycle indentation test on the hydroxyapatite coating sample H-2 (high solution concentration) showing the print of the indenter into the surface.

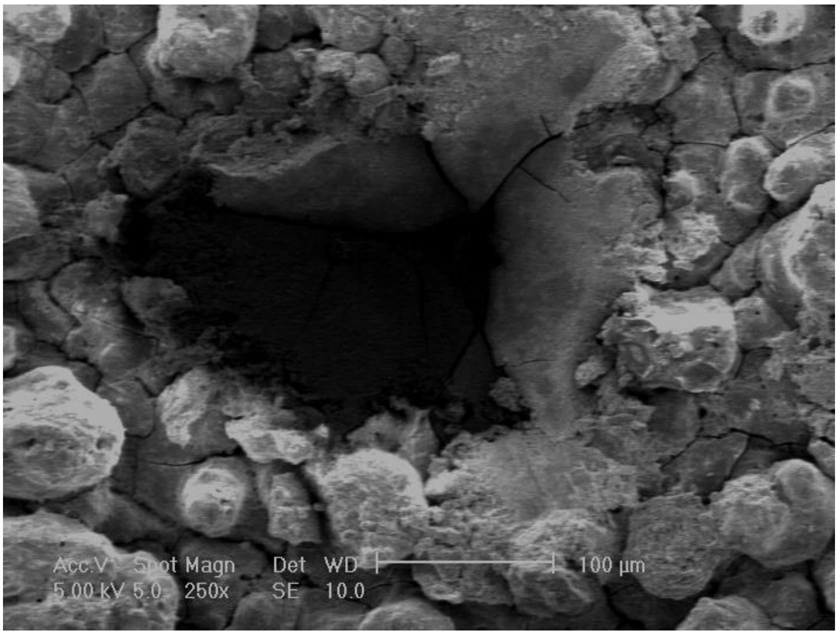

Figure III.2-11. SEM image after a multicycle indentation experiment on sample L-3 (low solution concentration) showing the residual print of the indenter into the surface.

Figure III.2-12 shows the plot of the reciprocal of contact stiffness against the reciprocal of the square root of contact area for representative coatings prepared using high solution concentration and low solution concentration together with the plot of elastic modulus as a function of the indentation depth. It can be noted that Figure III.2-12 shows a relatively good linear relationship especially regarding the morphology of the tested coatings presented in Figure III.2-2 and Figure III.2-4. Based on these graphs, the values of the elastic modulus of the HA coatings are also calculated and presented in Table III.2-3.

Table III.2-3. Elastic moduli from the sprayed hydroxyapatite coatings.

Sample Code	Elastic Modulus [b] (GPa)	Sample Code	Elastic Modulus [b] (GPa)
Using high initial concentration of solution precursor		Using low initial concentration of solution precursor	
H-1	12.0 ± 2.3	L-1	6.4 ± 1.2
H-2	22.0 ± 2.7	L-2	8.6 ± 0.9
H-3	10.0 ± 2.1	L-3	5.0 ± 0.9
H-4	10.5 ± 2.8	L-4	6.9 ± 1.3

[b] Mean (± standard deviation) assessed by multi-cycle microindentation tests (Berkovich indenter)

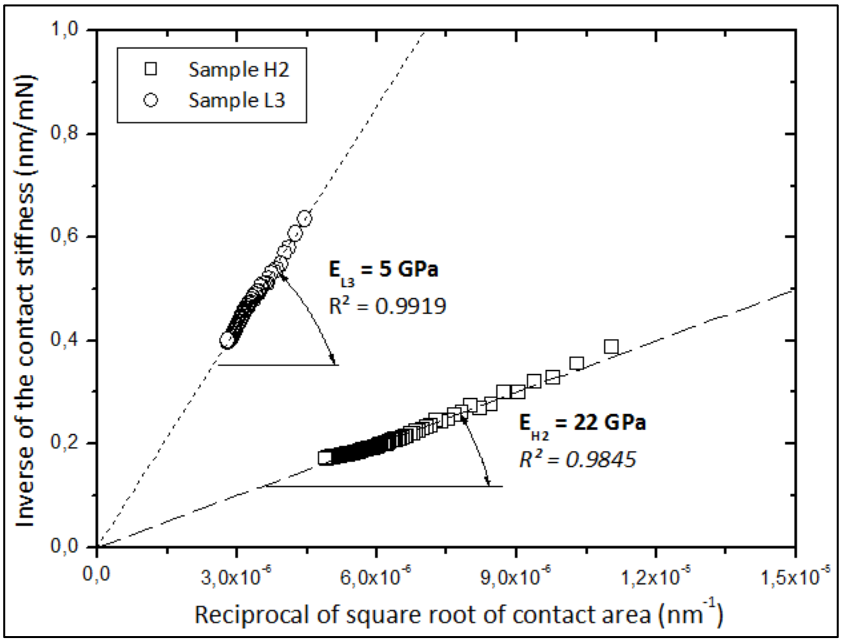

Figure III.2-12. Inverse of contact stiffness as a function of the reciprocal of the square root of contact area for representative samples H-2 and L-3.

From the obtained results, the elastic moduli had values between 5.0 and 22.0 GPa with a standard deviation ranging from 12.4% to 26.3%. It should be emphasized that HA coatings sprayed using a solution precursor with a higher initial concentration had relatively higher elastic moduli compared to coatings prepared using low initial solution concentration precursor. This finding is correlated with the relatively dense microstructure and high crystallinity of coatings prepared using highly concentrated solution. On the other hand, the obtained elastic modulus values were smaller comparing to the values obtained using different plasma spraying process [115, 116, 117]. Figure III.2-13 shows the plot of elastic modulus versus the maximum indentation depth from samples H-2 and L-3 where it can be seen that the elastic modulus remains nearly constant for both samples as the indentation depth increases regardless of the thickness implying that the elastic modulus for this material does not change with the indentation depth. Normally, the effect of compaction should be observed on elastic properties, but given the magnitude of the elastic modulus, the effect is not obvious in the multicycle indentation tests.

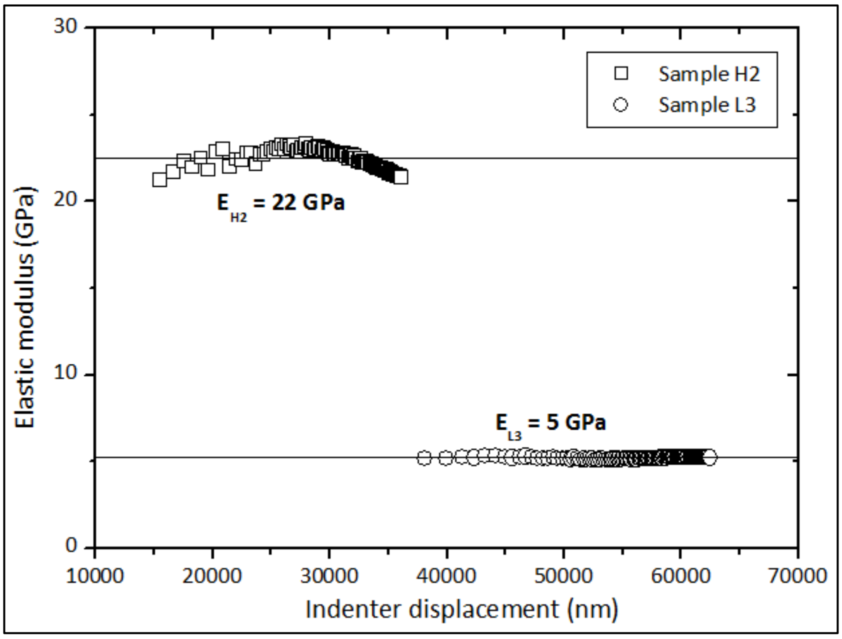

Figure III.2-13. Elastic modulus versus the maximum indentation depth for representative samples H-2 and L-3.

III.2.5. Discussion

The mechanical properties of SSPS-HA coatings were investigated in relation to their microstructural characteristics. HA coatings prepared using high solution concentration were relatively dense and more crystalline compared to coatings sprayed using low solution concentration. The values of the elastic modulus of the coatings were between 5.0 and 22.0 GPa depending on the used solution concentration. The obtained values were much lower compared to that of HA coatings sprayed using coarse powder and also lower than that of plasma sprayed coatings using suspension. These coatings had elastic modulus of 53–58 GPa [118] and 16–32 GPa [117], respectively. This difference in the elasticity of coatings is related to the microstructural features in the coatings obtained by different spray processes. The SPPS process could have led to the creation of voids between each other upon impact onto the substrate leading to porous coating formation as observed in the scanning electron micrographs. Moreover, the computed Martens hardness on the surface of the coatings were between 0.04 – 0.17 GPa which are smaller compared to the 1.9 – 4.3 GPa [119, 120] prepared using coarse HA powder and 0.2 – 0.5 GPa [117] for suspension plasma sprayed HA coatings. It is important to highlight that samples prepared with lower solution concentration of Ca/P did not exhibit any distinction on the elastic modulus and hardness values as function of the crystallinity volume fraction (determined by using an indexing software and computer assisted). This lower hardness value is endorsed to the heterogeneous microstructures present in the SPPS-HA coatings that create micropores, cracks and weak interfaces. In the presence of this microdefects, the indenter could easily penetrate into the irregular shape and fine microstructures whereas when well-melted lamellae (owing the higher crystallinity grade) are present splats providing better support to each other. Additionally, the presence of porous volume usually interferes into the indentation measurement data during the coating hardness evaluation. In the case of multicycle indentation tests, each cycle modifies the shape and distribution of the pores and finally the porosity network. Consequently, the hardness should vary between the hardness of the as-received porous coating toward that of the densified coating by the indentation process. Additionally, owing the roughness of surface and irregularities in thickness of coatings at the location where the indentation is performed, the coating thickness could be different from the mean value presented in Table II.2-1 interfering with the computation of the material property.

Initially, it was thought that changes of hardness values versus the displacement may be attributed to the influence of the substrate on the hardness of the coating. Nevertheless, according to a further analysis this change in the hardness is above all due to the densification of the coating as the indenter penetrates into the material surface. In this case, the value of the “film hardness” can be interpreted as the hardness of porous volume and the “substrate hardness” can be interpreted as the hardness of the dense volume of the coating instead. According to this approach of analysis, the values of hardness and elastic modulus are in agreement with those presented by He *et al.* [121] with a percentage of porosity between 33 % and 55%. Interestingly, the coatings prepared using high solution concentration had higher elastic modulus and hardness compared to coatings prepared using low solution concentration. This finding can be related to the crystallinity and morphology of coatings. Although, it was found that the coatings having highest crystallinity had better mechanical properties, it is however not conclusive that crystallinity alone directly enhances the cohesive strength of the coatings. It is more likely that the spray conditions, which influence the crystallinity value, might also be the same conditions that enhance the interlamellar cohesion and interface adhesion of the coatings. The micropores and weak interfaces observed in the coatings prepared using low solution concentration really contributed to their low hardness value. It is probable that during indentation, the indented large pores resulted in cracking with permanent deformation without any elastic recovery.

To study the variation of the mechanical properties of the HA coatings as a function of the crystallinity volume fraction some models validated on semi-crystalline polymers are discussed [122, 123, 124, 125]. Concerning the elastic modulus, the theoretical lower bound (linear mixture law) and the upper bound (harmonic mixture law) proposed originally by Reuss and Voigt, respectively, allow delimiting the experimental values. On the one hand, Okui and Sakai [126] simply proposed a harmonic mechanical model to relate the reciprocal of ultimate elastic modulus and the crystallinity volume fraction by the following proportional equation:

$$\frac{1}{E} = \frac{\mathrm{X}_{Cr}}{E_{Cr}} + \frac{(1 - \mathrm{X}_{Cr})}{E_a} \qquad \text{(III.2-5)}$$

where E denotes the elastic modulus and X_{Cr}, is the crystallinity volume fraction. E_{Cr} and E_a represent the elastic modulus of the crystalline and amorphous phases, respectively. Nonetheless, to represent the variation of the experimental elastic modulus between the lower and the upper bounds, the elastic modulus- crystallinity relationship proposed by the Halpin-Tsai's composite theory can also be applied as it has been carried out by previous works [123, 127].

Janzen [128] studied further the elastic modulus and the density over more than 1 100 polyethylene and, as a result, an expression was proposed obtained from the methods of Hill [124], Budianski [125] and Mossotti-Clausius [129] in which the changes of the parameter λ as a function of the Poisson's ratio, (ν) were negligible, thus it was estimated replacing it by a constant value. Following this reasoning, the equation derived by Landauer [130] and applied in the work of Janzen [128] is given by:

$$E = \frac{\varphi + (\varphi^2 + 4\,\lambda E_{Cr} E_a)^{\frac{1}{2}}}{2\lambda} \qquad \text{(III.2-6)}$$

where $\varphi = E_{Cr}[X_{Cr}(1+\lambda) - 1] + E_a[(1 - X_{Cr})(1+\lambda) - 1]$, with λ taken as a constant $(\lambda \approx 3\nu)$ as it was pointed out previously. It can be noticed that Eq. (III.2-6) can be used to estimate the value of the elastic modulus E as a composite value from the elastic modulus of the crystalline and amorphous phases.

The model proposed by Janzen [128] was derived from that of Halpin–Tsai's model which was also adopted in the works developed by Crist *et al.* [123] and Doyle [127]. In theory, using the amorphous and crystal modulus of composite materials, the called mixing parameter χ could provide a modeling of different materials in which elastic moduli are located between the Voigt (upper) and the Reuss (lower) bounds. In this sense, Humbert *et al.* [131] developed a model to analyze the influence of the crystallinity over the elastic modulus of composite materials, especially in semi-crystalline polymers, and set a physical meaning of the adjustable parameter or system. In order to describe the elastic modulus as a function of the crystallinity, the authors of this work proposed a macroscopic model from the point of view of the mechanical coupling. Finally, Humbert *et al.* [131] advanced the following relationship to express the elastic modulus as function of the crystallinity volume fraction (X_{Cr}):

© 2016 Tous droits réservés. lilliad.univ-lille.fr

$$\frac{1}{E} = \frac{1}{E_a} \cdot \frac{(1 - \mathrm{X}_{Cr})}{k_H \cdot \mathrm{X}_{Cr} + (1 - \mathrm{X}_{Cr})} + \frac{1}{E_{Cr}} \cdot \frac{\mathrm{X}_{Cr}}{\mathrm{X}_{Cr} + \frac{(1 - \mathrm{X}_{Cr})}{k_H}} \quad \text{(III.2-7)}$$

In this equation, k_H is a fitting parameter from the model; when $k_H = 1$, the obtained model is the lower bound and when $k_H = \frac{E_{Cr}}{E_a}$, the resulting model is the upper bound.

To ascertain the influence of microstructures to the elastic modulus and hardness of the coatings, the models developed by Janzen [128], Okui and Sakai [126] and Humbert *et al.* [131] were applied. The determination of the amorphous (considered as the soft phase) and the crystalline phases (estimated as the hard phase) as well as the prediction of the behavior of coating material at different crystallinity volume fractions were made possible using these models. The values obtained by applying the models concerning the variation of the elastic modulus and the hardness as a function of the crystallinity volume fraction is presented in Table III.2-4.

Table III.2-4. Fitting parameters from the models describing the elastic modulus and hardness as function of the crystallinity volume fraction used (X_{Cr}) for all the SPPS-HAP coatings.

Model	Janzen [128] (1)	Okui and Sakai [126] (2)	Humbert *et al.* [131] (3)
		Elastic modulus	
E_{Cr} (GPa)	41.4	41.4	41.4
E_a (GPa)	6.4	9.0	6.4
k_H	-	-	2
		Hardness	
H_{Cr} (GPa)	0.29	0.60	0.40
H_a (GPa)	0.07	0.07	0.07
k_H	-	-	1.11

(1) The fitting parameters in the model were E_a, E_{Cr} and H_a, H_{Cr}, where E and H denote the elastic modulus and hardness, respectively.
(2) The fitting parameter in the elastic modulus model was E_a whereas in the hardness model were H_a and H_{Cr}.
(3) The fitting parameters in the elastic modulus model were E_a and k_H and in the hardness one H_{Cr} and k_H.

Janzen's model was used first to fit the experimental data by considering the elastic modulus of the amorphous phase E_a and the crystalline phase E_{Cr} as adjustable constants. The parameter λ was assumed as constant equal to 0.75 ($\lambda \approx 3\nu$) assuming the Poisson's ratio $\nu = 0.25$ [121]. The values obtained by means of non-linear least square analysis were $E_a = 6.4$ GPa and $E_{Cr} = 41.4$ GPa. Although the elastic modulus of the material depends on the coating manufacturing procedure as well as on the crystallinity volume fraction and the percentage of porosity, the values described by the model used were of the same order of magnitude as those reported in the literature [121, 132, 133]. The Okui and Sakai's model was then tried to fit to the experimental data by taking E_a and E_{Cr} as fitting parameters using Eq. (III.2-5), but the model was not convergent. Nevertheless, by considering $E_{Cr} = 41.4$ GPa found by the Janzen's model and by letting the elastic modulus of the amorphous phase as an adjustable parameter, the value of $E_a = 9.0$ GPa was found, being in agreement with the value obtained by the model of Janzen [128]. The last model implemented to predict the behavior of the elastic modulus versus the crystallinity volume fraction was the one derived by Humbert *et al.* [131]. Following the previous reasoning, the parameters E_{Cr}, E_a and k_H of Eq. (III.2-7) were assumed as adjustable parameters. However, this model also did not converge to reasonable values. Considering purely E_a and k_H as the only adjustable parameters to fit the model, the results derived from this expression were found to be $E_a = 6.4$ GPa and $k_H = 2$.

Furthermore, the same mathematical models were applied to predict the hardness behavior as function of the crystallinity volume fraction. All the models also represent adequately the hardness-crystallinity relationship. The computed values for the hardness of the amorphous and crystalline phases are 0.07 and 0.29–0.40 GPa, respectively, except for the model proposed by Okui and Sakai [126] which tends to overestimate the hardness of the crystalline phase as well as the elastic modulus of the amorphous phase. Additionally, the fitting parameter k_H from the Humbert *et al.*' model takes different values for the determination of the elastic modulus and hardness. Figure III.2-14 represent the models from Janzen [128], Okui and Sakai [126] and Humbert *et al.* [131] applied to the description of the elastic modulus of the SPPS-HA coatings, whereas Figure III.2-15 illustrates the hardness variations as a function of the crystallinity volume fraction of the hydroxyapatite coatings by implementing the described models advanced by Janzen [128], Okui and Sakai [126] and Humbert *et al.* [131]. It is observed that the Janzen's model [128] described better the behavior of the elastic modulus as a function of the crystallinity. Conversely, the Okui and Sakai's model differs from the model of Janzen and it slightly overestimated the values of the amorphous phase predicted from the experimental data compared to the values obtained by the others two models adopted in this work. It is noticeable that the values of the elastic modulus obtained experimentally for the samples studied by the instrumented indentation test using a continuous multicycle protocol are into the two boundaries (lower and upper limits) described by the Humbert *et al.*'s model as it was explained earlier above.

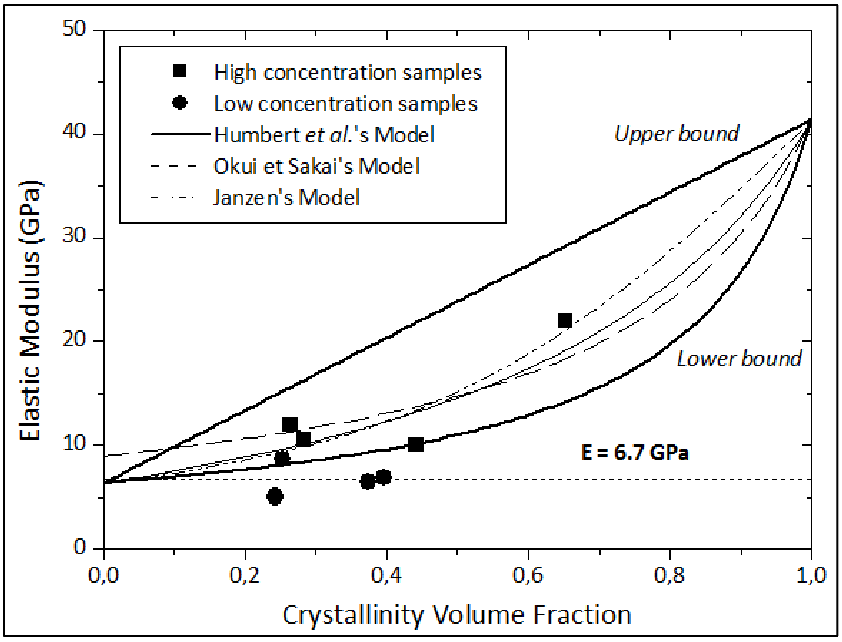

Figure III.2-14. Models describing the elastic modulus of the hydroxyapatite coating samples (specimens prepared with high and low solution concentration) as function of the crystallinity volume fraction.

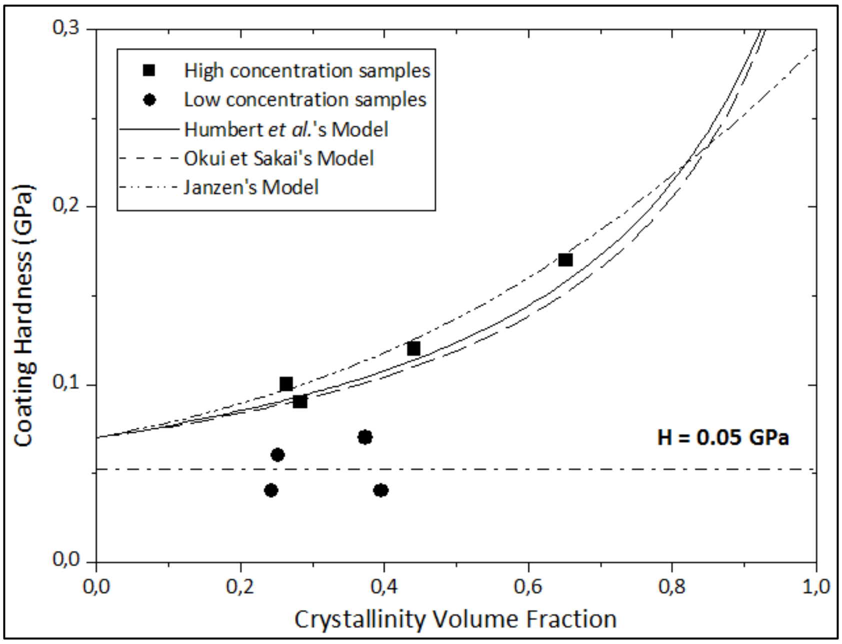

Figure III.2-15. Models describing the hardness of the hydroxyapatite coating specimens (samples produced using high and low solution concentration) versus the crystallinity volume fraction.

For the description of the elastic modulus and hardness versus the crystallinity volume fraction, only the samples prepared using high solution concentration were taken into account since the samples formed with a lower solution concentration of Ca/P did not show any distinction in the elastic modulus and in the hardness values as a function of the crystallinity volume fraction. The average elastic modulus and hardness values for the low solution concentration samples were 6.7 GPa and 0.05 GPa, respectively. Based on Janzen's model and considering the values obtained in Table III.2-4, considering in this case the highest solution concentration studied in this research, the crystallinity volume fraction corresponding to the elastic modulus of a bone-like microstructure can be predicted and it should be between 0.56 and 0.86 according to the values of elastic modulus and hardness obtained from a bone in a previous work [134].

When discussing about heterogeneities of materials, in this case, presence of pore networks, it is possible to anticipate the existence of dispersion in the results obtained for mechanical properties of materials, *i.e.* hardness and elastic modulus. Considering the profile of the load–displacement curve, there is no doubt that it will depend of the relative position of the pores to the path of displacement of the indenter, it means, that if pores are in the top of the surface then the values of hardness will be lower (the load-displacement curve would tend to the right, *i.e.* a greater contact area A_{C}) than if the porous surrounding is in the bottom of the path of the indenter during the test (the load-displacement curve would tend to the left, *i.e.* a lower contact area A_{C}), which means that the interpretation of the data acquired should be carry out very carefully.

III.2.6. Conclusions

The solution precursor plasma sprayed hydroxyapatite coatings (SPPS-HA) on stainless steel substrate were tested by multicycle indentation test at microscale range, and mechanical properties such as elastic modulus and coating hardness were found. The microstructure of relatively dense coatings prepared using high concentration of solution precursors included fine particles and agglomerated fragmented shells while the coatings obtained using low solution concentration showed less dense microstructural features with microcracks, weak interfaces and big pores present at the cross-section that greatly affects their mechanical behavior. Elastic modulus and hardness of the SPPS-HA coatings were found to be from 5.0 GPa to 22.0 GPa and from 0.04 to 0.17 GPa, respectively. Coatings sprayed using a high concentrated solution had an average elastic modulus and hardness nearly two times greater than the less concentrated ones. A novel model is advanced to separate the contribution of the hardness of a porous coating from the densified one as function of the indentation depths. Regarding this model, the influence of the densification of the coatings on hardness measurements initiates between 50% to 85% of the coating thickness, according with the obtained values of the fitting parameter κ. The sample coating having the highest crystallinity which was prepared from high concentration of solution has the greatest elastic modulus (22.0 GPa) and hardness (0.17 GPa) among all coatings. On the other hand, the studied mechanical properties of the coatings from low concentration of solution precursors was not significantly influenced by the crystallinity volume fraction having only an average hardness and elastic modulus of 0.05 GPa to 6.7 GPa, respectively. The models previously used in describing the polymers were applied to describe the behavior of mechanical properties of SPPS-HA coatings prepared using high solution concentration. The values of the mechanical parameters increase with the crystallinity volume fraction from $H_a = 0.07$ and $E_a = 6.4$ GPa to $H_{Cr} = 0.29$ GPa and $E_{Cr} = 41.4$ GPa, which correspond to the mechanical properties of the amorphous and the crystalline phases, respectively.

Moreover, mechanical properties obtained from SPPS-HA coatings were smaller in comparison to the values obtained using conventional plasma spraying process that can be attributed to the unique microstructural features present in the coatings. Hardness and elastic modulus of the samples were described as a function of the crystallinity volume fraction in order to predict its behavior for the estimation of the corresponding crystallinity volume fraction. For the precursor with higher initial solution concentration, the predicted crystallinity volume fraction to obtain a bone-like microstructure should be between 0.56 and 0.86 based on the Janzen's model. Study on the influence of the microstructure and crystallinity to the physical behavior of the SPPS-HA coatings submitted in a simulated body fluid should clarify its potential for biomedical applications.

III.3. MECHANICAL PROPERTIES BY MULTICYCLE INDENTATION TEST FROM A BILAYER COATING SYSTEMS

III.3.1. Introduction

The study of mechanical properties from multilayers coating system have been an interesting topic to researchers in the last years. With the intention of extend the analysis of the continuous multicycle indentation tests beyond bulk materials, they were performed over a bilayer electroless Ni-P coating deposited on carbon steel plates. The assessment of the hardness and elastic modulus from the whole system is an opening estimation about the properties from an each and every single component of a multilayer coating system and, accordingly, with their possible tribological applications. Nevertheless, the evaluation of the hardness and elastic modulus of one and all layers of a coated material allows to estimate its contribution to the total composite property, and consequently, a design improving, chemical composition and/or deposition process adjustment of one or another layer could be proposed and implemented. Along this section, a bilayer electroless Ni-P coating deposited on carbon steel plates is examined and described as function of its mechanical properties, when it is submitted to CSM tests at nanoscale range and continuous multicycle indentation tests at a microscale range. From SEM images coupled with the corresponding load-indentation curves, it is illustrated the phenomena that occur during the indentation process, *i.e.* microcracks growing and surface chipping.

As well, by analyzing the data obtained at the microscale range, preceding advanced physical models to examine multilayer coated systems are implemented to study the hardness and elastic modulus behavior of every layer from the electroless Ni-P coating deposited on carbon steel plates. Moreover, a different approach is proposed to compute the elastic modulus of each layer from the expression of the reciprocal of the contact stiffness as function of the contact area formerly advanced by Tricoteaux *et al*. [112] for a monolayer coated material, but now extended to be implemented as a multilayer model based on the weight function suggested by Korsunsky *et al*. [135].

III.3.2. Mechanical properties from bilayer coating system

III.3.2.1. Indentation experiments

Electroless Ni-P coating deposited on carbon steel are studied in order to evaluate the mechanical properties, *i.e.* hardness and elastic modulus, of each layer from the coated system. Nine samples were studied by implementing a continuous multicycle indentation test. To identify each sample, they were labeled as follows: 1020-B, 1020-I, 1020-O, 1045-B, 1045-I, 1045-O, P20-B, P20-I and P20-O. The first characters of the sample code are to identify the substrate, it means, to denote the SAE 1020, SAE 1045, and SAE P20 carbon steels, used as substrate; and the last characters of the sample code represent the coating electroless deposited on the substrates, where B, O and I stand for the bilayer coating (the one with two layers with different heat treatment), innermost layer and outermost layer of the bilayer coating system, respectively. To accomplish the assessment of the hardness and elastic moduli of each layer, continuous multicycle indentation tests were designed to perform at least 5 tests on each sample in the following scenery: 100 cycles between 1 N, for the first cycle, to 18 N, applied load at the last cycle. Figure III.3-1 illustrates the load-displacement curve obtained from the microindentation tests accomplished by a continuous multicycle protocol, and Figure III.3-2 shows the load-displacement curve obtained from a CSM test on a electroless Ni-P coating deposited on a carbon steel plate.

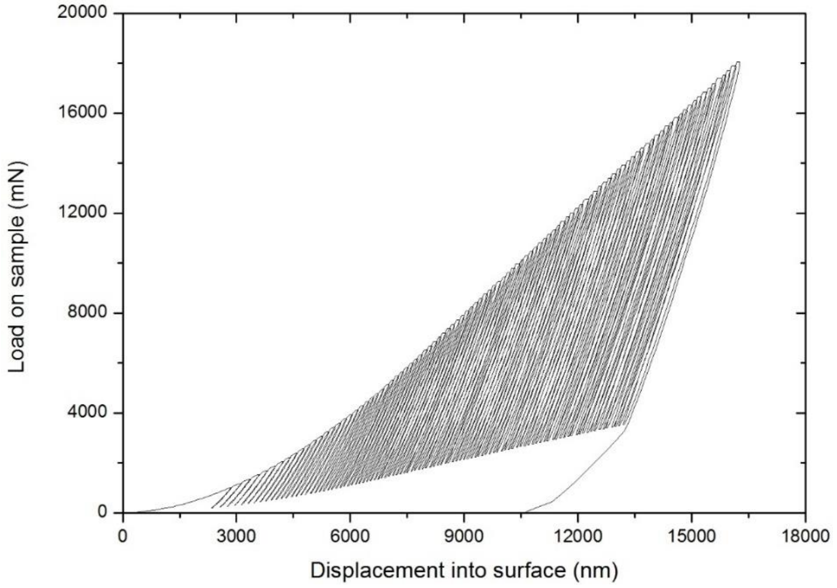

Figure III.3-1. Load-displacement curve from a continuous multicycle indentation test performed on a bilayer electroless Ni-P coating deposited on a carbon steel plate.

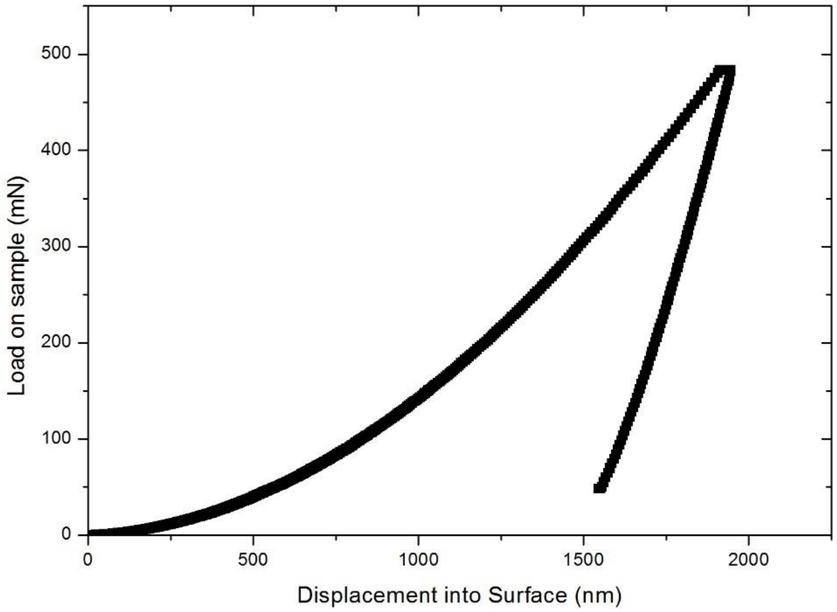

Figure III.3-2. Load-displacement curve from a CSM test performed on electroless Ni-P bilayer coating deposited on a carbon steel substrate.

By analyzing the load-displacement curve obtained by the continuous multicycle indentation tests and by means of microscope techniques, it was possible to identify some phenomena occurring during indentation tests. For example, in the Figure III.3-3 can be observed the load-displacement indentation curve and the optical micrograph of the residual impression left by the indenter into the surface of the material. It is noticeable that the only visible phenomenon is the overlapping of the material owing the load-unload sequence of the multicycle indentation test and it evidences the increasing of the plastic zone defined for the shear bands at the zone around the indenter print.

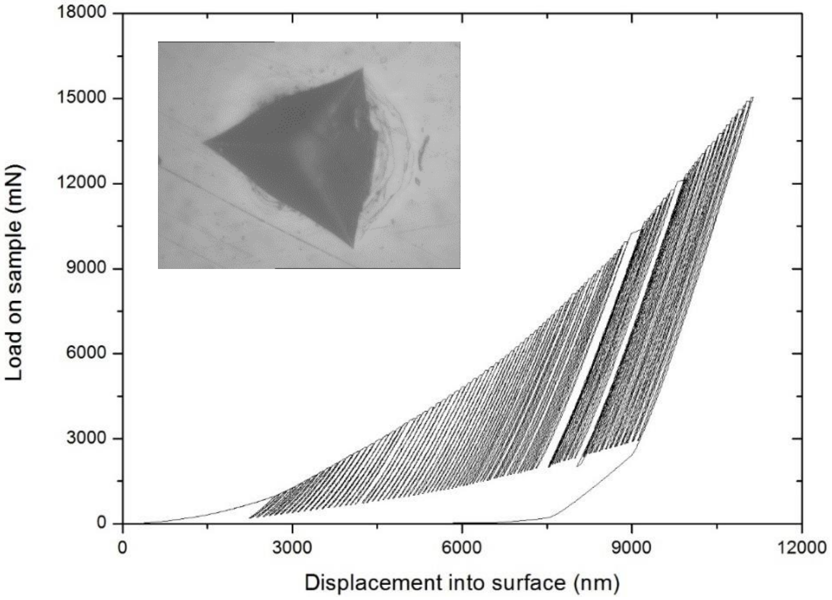

Figure III.3-3. Load-displacement curve from multicycle indentation test performed on a electroless Ni-P bilayer coating deposited on a carbon steel substrate. The pile-up effect is noticeable around the indenter impression.

Comparing the micrograph acquired by SEM technique shown in Figure III.3-4 and Figure III.3-5, it is interesting to observe that the size of the impression left by the Berkovich indenter by applying a continuous multicycle test does not exhibit a remarkable difference compared with the indenter print when a standard indentation test was performed on the bilayer Ni-P coating deposited on the SAE 1020 carbon steel sample.

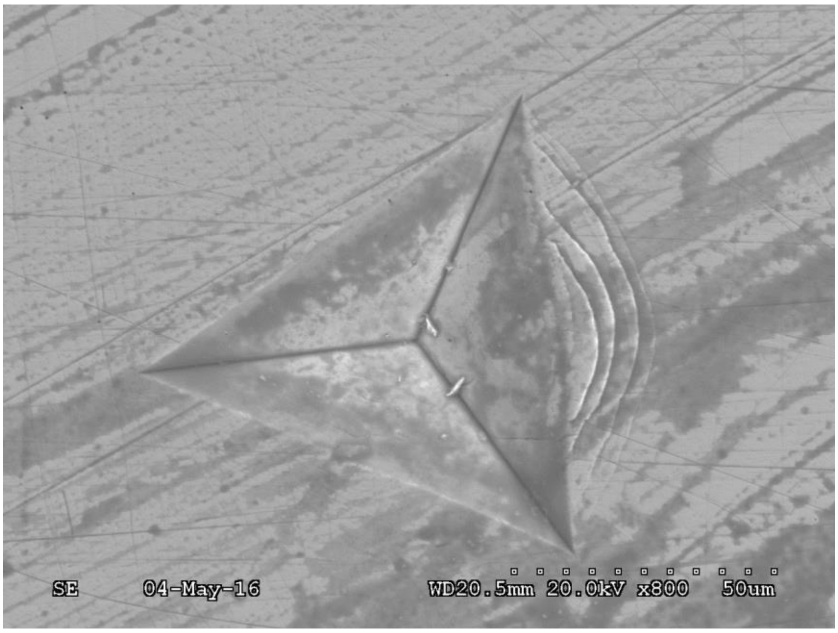

Figure III.3-4. SEM micrograph of the residual impression from a Berkovich indenter on the sample labeled as 1020-B submitted to a continuous multicycle indentation test.

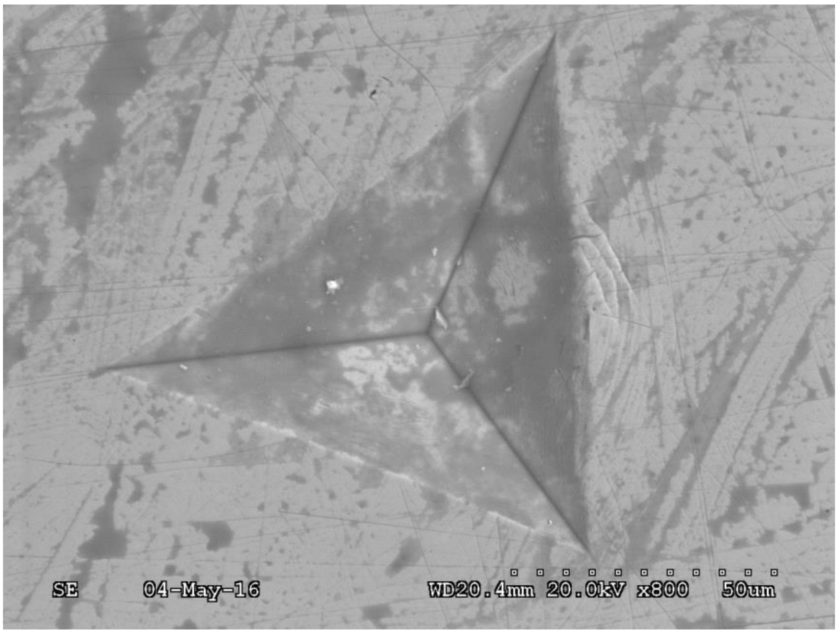

Figure III.3-5. SEM image from a residual impression from a Berkovich indenter on the sample labeled as 1020-B after standard indentation test is accomplished.

Moreover, by SEM technique in Figure III.3-4, it is possible to define the shear bands around the impression left by the Berkovich indenter where it is possible to indicate that there was not any pile-up effect around the indenter during the indentation process.

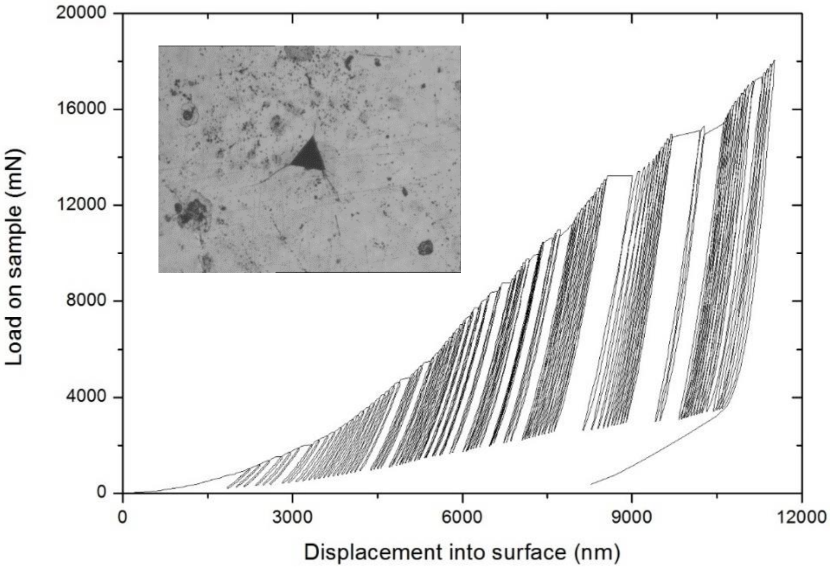

Figure III.3-6. Load-displacement curve from multicycle indentation test performed on a electroless Ni-P bilayer coating deposited on a carbon steel substrate. The crack on corners of the indenter impression is related to the large horizontal displacement on the load-displacement curve.

Conversely, Figure III.3-6 shows the load-displacement curve performed on the sample with the innermost layer of the bilayer coating system. Comparing with the preceding load-displacement curve the differences between them are manifest. In this case, it was corroborated that gaps existing between one cycle and next one was due to the growing of microcracks in the corners of the Berkovich indenter print. It can be state that each gap appearing in the load-displacement curve involves an increasing on the crack length associated to the response of the material submitted to the load-unload sequences of the multicycle instrumented indentation test.

Moreover, Figure III.3-7 suggests evidence of another phenomenon occurring during the test. As it can be seen, the indenter impression exhibits not only cracks at its corners but chipping around it. More interesting is that the load-displacement curve shows the gaps due to the crack length increasing and also the chipping phenomenon by showing a sort of hysteresis loop at each cycle from the point that chipping is presumed that arose, approximately when indentation depth is nearby 10 000 nm and the load on the sample is around 12 000 mN. Additionally, the image obtained by SEM technique exhibits in Figure III.3-8 illustrate the chipping process occurring when a continuous multicycle indentation is accomplished, nevertheless, these evidences of damage into the material was only observed in the electroless Ni-P coating with heat treatment at 400 °C, that is the innermost layer in the bilayer coating deposition.

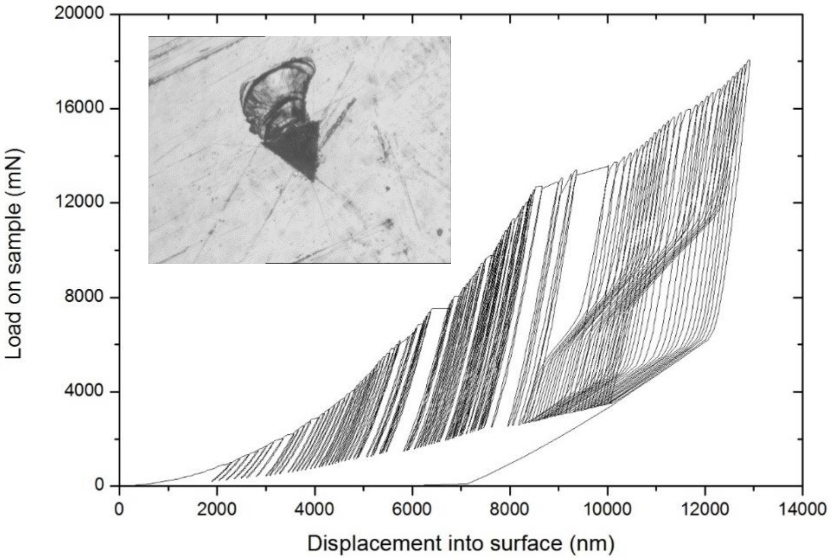

Figure III.3-7. Load-displacement curve from multicycle indentation test performed on a electroless Ni-P bilayer coating deposited on a carbon steel substrate. The chipping remarked on the indenter impression is related to the hysteresis loop observed in the load-displacement curve.

It is interesting to observe in Figure III.3-9 and Figure III.3-10 the microcracks growth when standard indentation test is accomplished on the coated sample with the electroless Ni-P coating deposited on carbon steel plates heat treated at 400°C.

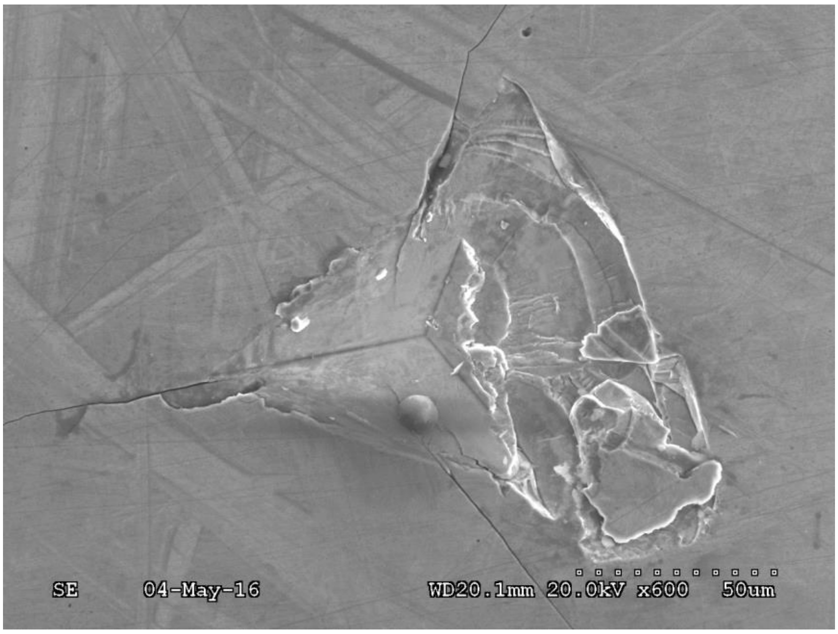

Figure III.3-8. SEM micrograph from the residual impression from a Berkovich indenter on the sample labeled as 1020-I after a continuous multicycle indentation test of 100 cycles is accomplished.

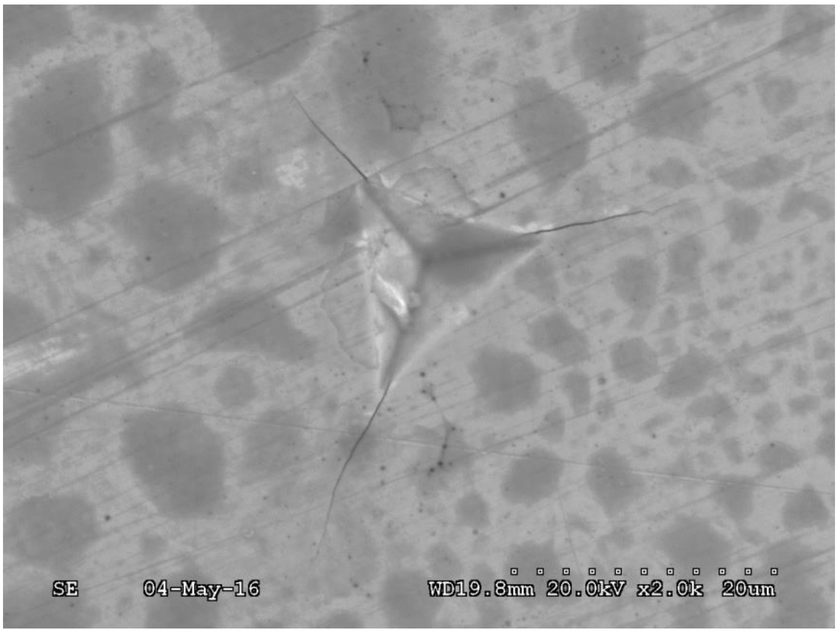

Figure III.3-9. SEM micrograph from the residual impression from a Berkovich indenter on the sample labeled as 1020-I after standard indentation test with a maximum applied load 1 N is accomplished.

As it can be noted in Figure III.3-9 and Figure III.3-10 only microcracks are present in the residual impression of the Berkovich indenter which indicates that a continuous multicycle test can be induced an important damage in brittle materials. Comparing Figure III.3-8 and Figure III.3-10 and considering that both were obtained after a maximum applied load of 18 N, but the former after a continuous multicycle test and the other one after a standard indentation test, it is remarkable the presence of chipping when the multicycle indentation test is performed, in contrast with the impression left by the indenter when a standard test is accomplished which only exhibit the microcracks along the corner of the indenter print.

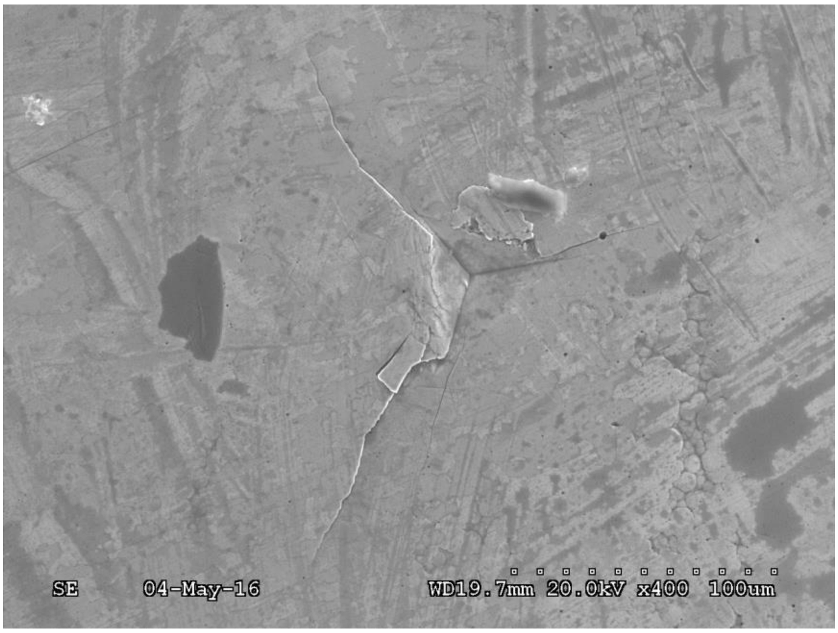

Figure III.3-10. SEM micrograph from the residual impression from a Berkovich indenter on the sample labeled as 1020-I after standard indentation test with a maximum applied load 18 N is effected.

III.3.2.2. Composite elastic modulus model.

Elastic modulus from the bilayer system is evaluated by means of CSM tests and multicycle indentation tests. Accordingly, a calibration curve is effectuated in order to obtain the contact area function proposed by Oliver and Pharr [1]. Figure III.3-11 illustrated the standard calibration performed on a fused silica specimen with an elastic modulus of 71 GPa approximately. It can be observed that the elastic modulus values remain constant from up to around 10 nm.

On the basis of the obtained calibration curve from the fused silica specimen described above, to compute and compare the elastic modulus of the sample to be examined, the values of the elastic modulus recorded from the CSM tests to be taken into account will be from 60 nm, to avoid the possible influence of the blunt defect of the indenter tip (estimate it in III.1.2.4) up to around 1800 nm. Under this consideration, Figure III.3-12 illustrates the elastic modulus behavior of the bilayer Ni-P coating system evaluated by CSM tests. It can be noted that the elastic modulus decreases from 325 GPa to 140 GPa, approximately. Now, the elastic modulus computed from multicycle indentation tests is plotted in the same graph and a tendency could be defined according to the plot presented in Figure III.3-13.

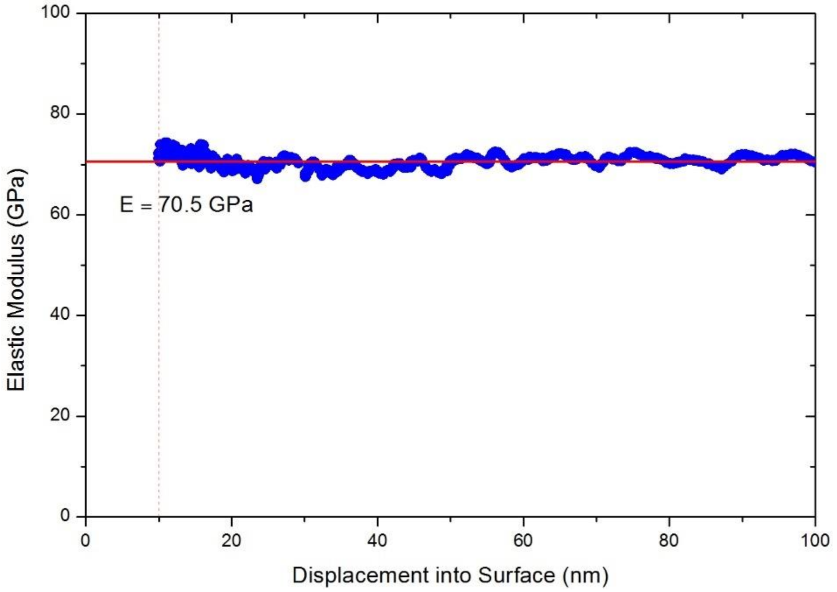

Figure III.3-11. Calibration curve of Berkovih indenter to be employed in CSM tests on Ni-P coatings. Fused silica specimen was used as the standard sample. The elastic modulus of fused silica remains constant from about 10 nm.

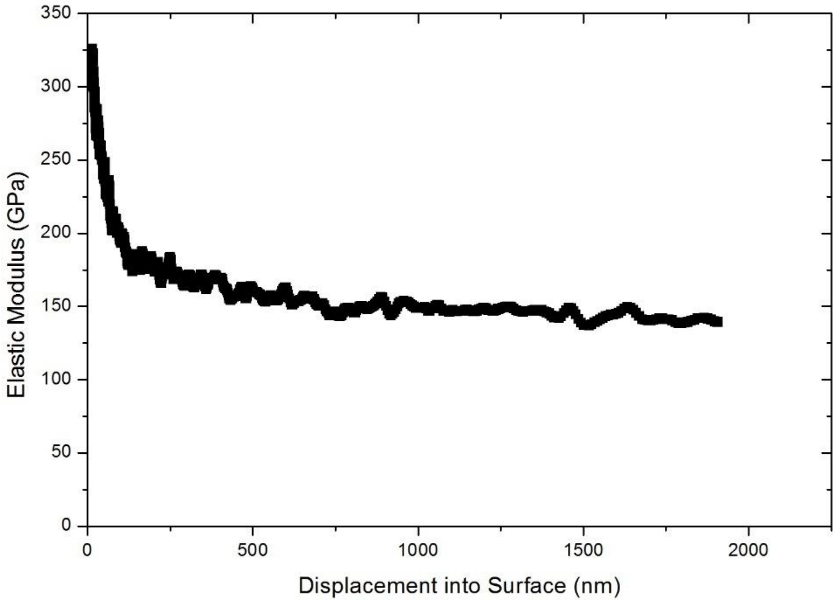

Figure III.3-12. Elastic modulus recorded by CSM test from a bilayer Ni-P coating system performed up to a depth penetration of 2000 nm.

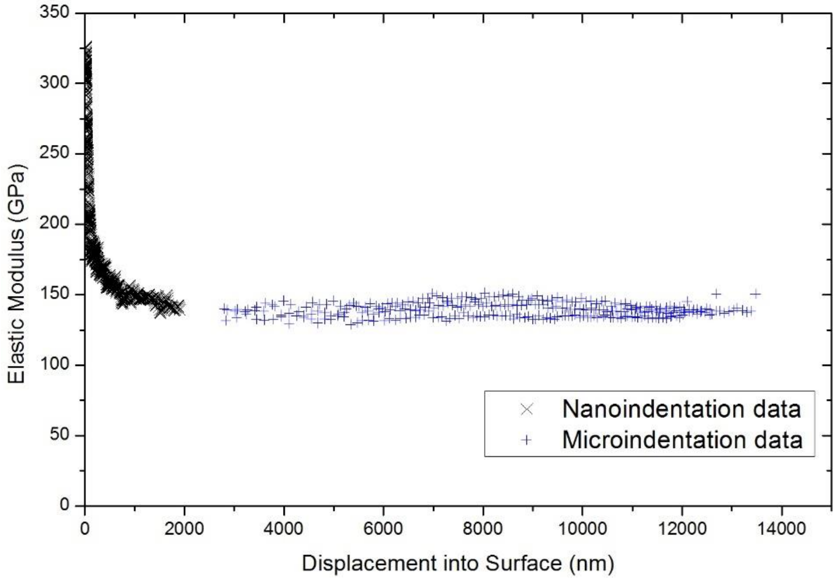

Figure III.3-13. Elastic modulus from CSM tests and continuous multicycle tests performed on a bilayer Ni-P coating system.

III.3.2.3. Composite hardness evaluation

The indentation hardness definition (HIT) is adopted to analyze the comportment of the composite hardness of the system defined as it follows:

$$HIT = \frac{P_{\max}}{A_C} \qquad \text{(III.3-1)}$$

where A_C is the contact area taking into account the blunt defect of the indenter tip. By evaluating the hardness at each cycle, it is possible to describe its variations as function of the maximum displacement.

In order, to compare the hardness values obtained by CSM tests, a standard calibration of the indenter, described in the section above, was performed. Figure III.3-14 shows the plot of hardness continuously recorded from the CSM test performed on a fused silica specimen following the methodology suggested by Oliver and Pharr [1] to obtain the contact area function of the Berkovich indenter used to achieve the tests. It can be observed that the values of hardness from the fused silica specimen stay constant up to nearby 100 nm to the value of 9.6 GPa.

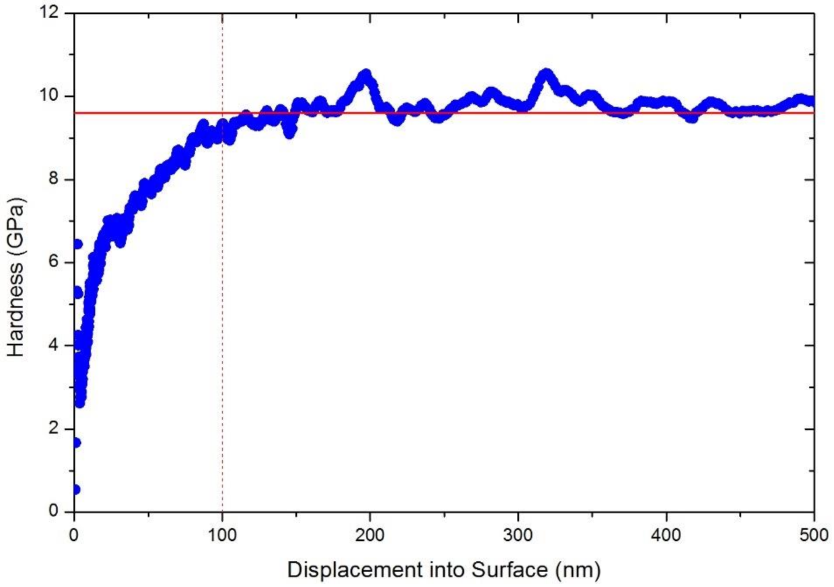

Figure III.3-14. Calibration curve of the Berkovih indenter used in tests. It was performed on a fused silica sample. A constant value of hardness is remarkable from approximately 100 nm.

According with the preceding calibration curve described, to compare and analyze the hardness value obtained from the CSM tests performed on the bilayer Ni-P coating system the data to be take into account to accomplish it will be from 100 nm to around 1800 nm by using the contact area function defined by the calibration procedure. Figure III.3-15 illustrates the hardness profile from a CSM test effected on the bilayer Ni-P coating system. It can be observed that hardness descends from 13 GPa approximately to 7 GPa which can be attribute to the indentation size effect (ISE). It is interesting when the data provided by the multicycle indentation tests and the CSM tests are plotted in the same graph as it can be seen in Figure III.3-16, that there is not a significant indentation size effect (ISE) into the computed hardness by implementing the multicycle indentation tests. However, it can be noted the continuity between the two scales of measurement resulting from nanoindentation and microindentation data.

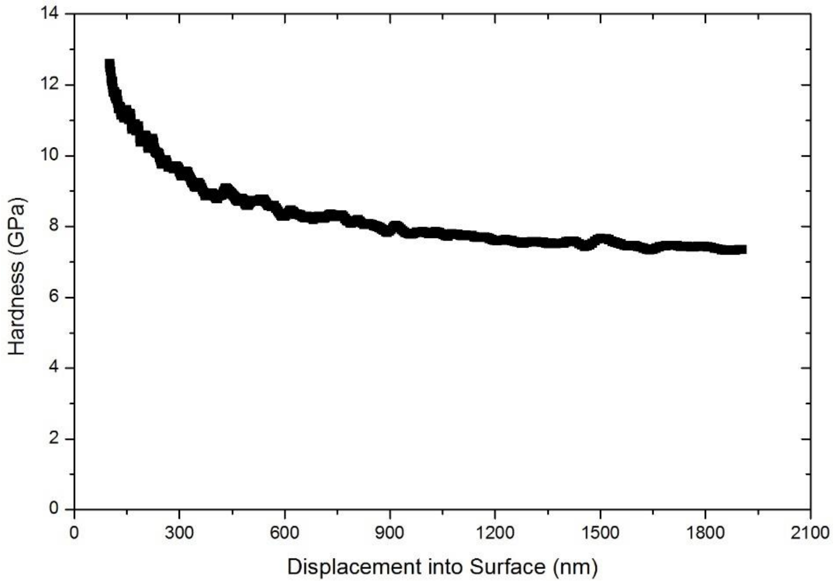

Figure III.3-15. Hardness continuously recorded from CSM test implemented on a bilayer Ni-P coating system performed up to a depth penetration of 2000 nm.

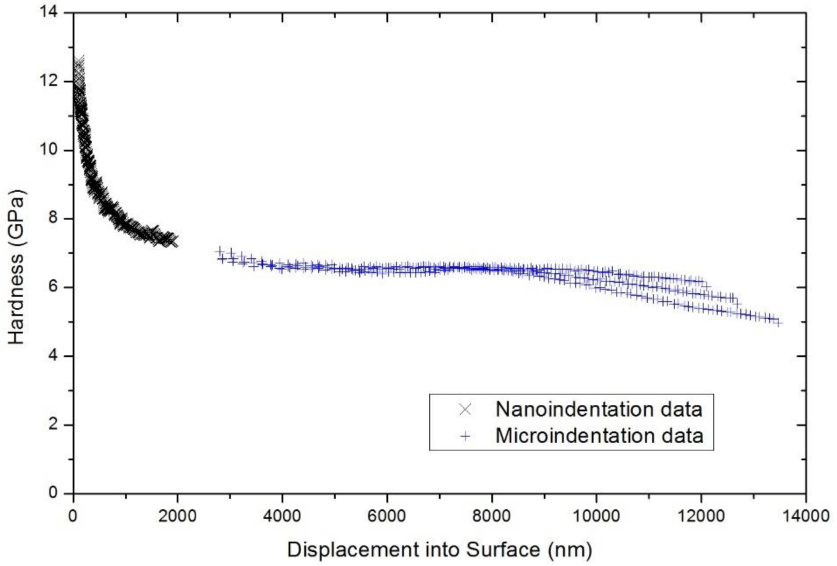

Figure III.3-16. Hardness computation from CSM tests and continuous multicycle test performed on a bilayer Ni-P coating deposited on a steel plate.

III.3.3. Discussion

Data from multicycle indentation test are analyzed in order to establish the mechanical properties, *i.e.* elastic modulus and hardness, from each layer from a bilayer Ni-P coating system. The modified Jönsson and Hogmark's model is applied with the aim of obtain the hardness of each layer of the system, according to the model, the hardness of the substrate will be considered well-known, and the hardness of each single film will be determined by non-linear least square regression analysis. Figure III.3-17 shows the description of data obtained by multicycle microindentation tests on a bilayer coating sample. On the other hand, Figure III.3-18 illustrated the description of the hardness behavior from the sample with the coating heat treated at 400 °C, as it was expected the graph shows an important gapping between one to another experimental point as it was noted in the load-displacement curve of this coating, shown earlier in Figure III.3-7 owing to the microcracks growth and the phenomenon of chipping on the surface.

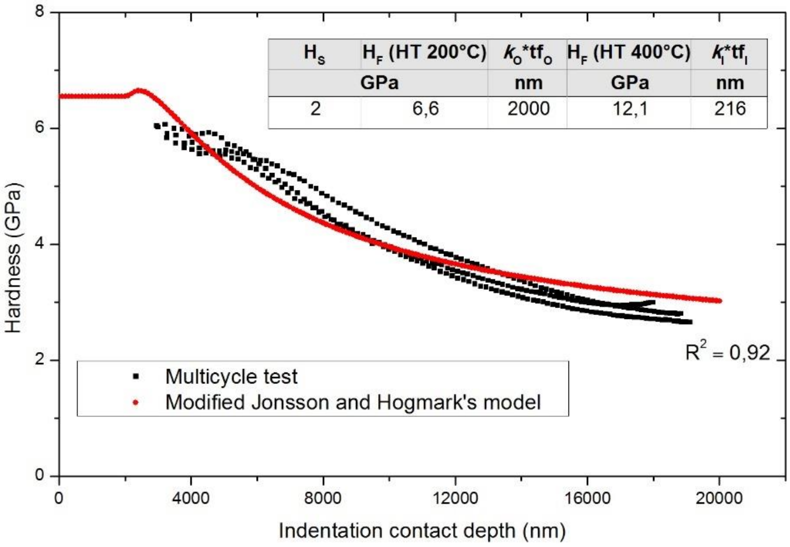

H_S	H_F (HT 200°C)	k_O*tf_O	H_F (HT 400°C)	k_I*tf_I
GPa		nm	GPa	nm
2	6,6	2000	12,1	216

Figure III.3-17. Hardness from multicycle indentation tests, described by the modified Jönsson and Hogmark 's model (sample 1020-B).

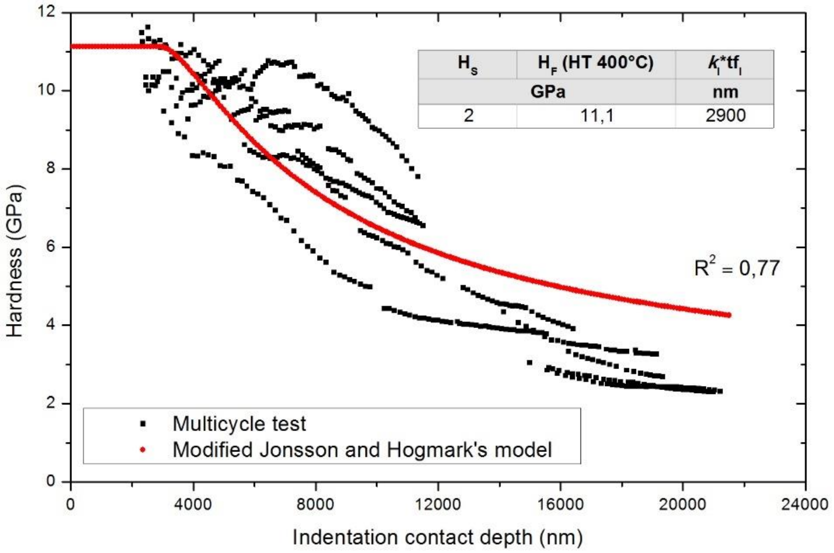

H_S	H_F (HT 400°C)	k_I*tf_I
GPa		nm
2	11,1	2900

Figure III.3-18. Hardness modeling from multicycle indentation tests by the modified Jönsson and Hogmark 's model (sample 1020-I)

On the other hand, Figure III.3-19 illustrates the behavior from the monolayer coating heat treated at 200 °C, which differs from the preceding graph in the nonappearances of gapping in the hardness behavior obtained by the continuous multicycle instrumented indentation test.

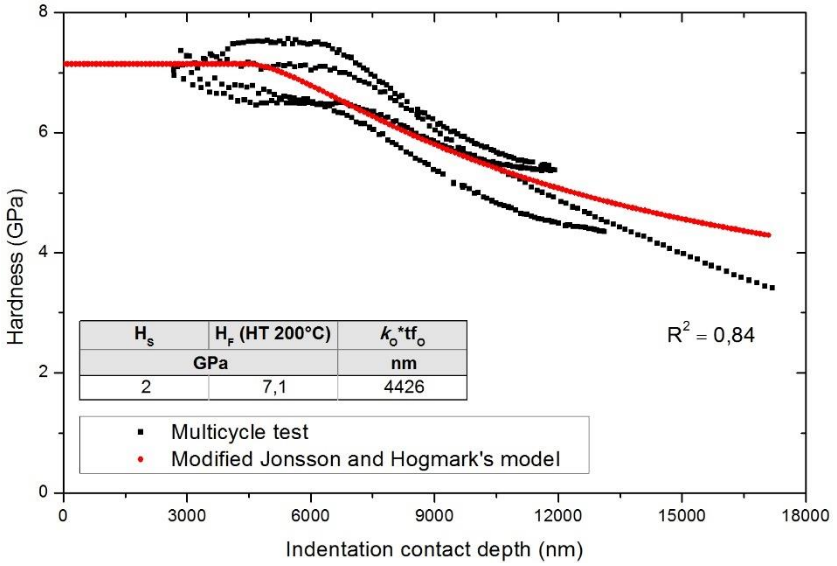

Figure III.3-19. Modified Jönsson and Hogmark 's model describing the hardness behavior of sample 1020-O from multicycle indentation tests.

As it can be observed in Table III.3-2, the hardness of the outermost layer assessed by implying the modified Jönsson and Hogmark's model was found to be between 5.9 and 8.1 GPa, when this proposal is applied to the bilayer electroless Ni-P coating system as well as when it was effected to the monolayer coating deposited on the three substrates. Regarding the computed hardness from the three deposition and substrates, the innermost layer hardness was estimated to be within 10.1 and 13.9 GPa, by implementing the mentioned model to the bilayer and the monolayer coting systems. On the other hand, when performing the non-linear regression analysis, the substrate hardness was imposed to be equal to 2 GPa which is approximately the hardness reported in the literature for carbon steel samples.

By applying the non-linear least square regression analysis, the fitting parameters were the hardness of each layer, it means, H_{F1} and H_{F2}, and also the expressions defined as $k_{\mathrm{JH}_O} \cdot t_{FO}$ and $k_{\mathrm{JH}_I} \cdot t_{FI}$. Usually if the thickness of the layer is well-known the fitting parameters would be k_{JH_O} and k_{JH_I} instead. Nevertheless, as it can be noted in the micrograph shown in Figure III.3-20 and Figure III.3-21 the thickness of each layer is not regular. Between the two images, taken in two different points, there is a remarkable difference in the thickness dimension of each layer from the bilayer electroless Ni-P coating. According to the modified Jönsson and Hogmark's model advanced by Puchi-Cabrera *et al.* [71], on the basis of the reasoning developed by Rahmoun *et al.* [69], the term $k_{\mathrm{JH}} \cdot t_F$ will represent the indentation depth at which the subsequent layer commences to contribute to the computed composite hardness from the continuous multicycle indentation test.

Table III.3-1. Elastic moduli and hardnesses of the deposited coatings and substrates.

Sample Code	Substrate Hardness (GPa)	Innermost layer Hardness [a] (GPa)	Outermost coating Hardness [a] (GPa)	$k_{\mathrm{JH}_O} \cdot t_{FO}$ (nm)	$k_{\mathrm{JH}_I} \cdot t_{FI}$ (nm)	R^2
SAE 1020 Carbon steel substrate coated						
1020-B	2.0	12.1	6.6	2 000	216	0.92
1020-I	2.0	11.1	-	-	2 900	0.77
1020-O	2.0	-	7.1	4 426	-	0.84
SAE 1045 Carbon steel substrate coated						
1045-B	2.0	10.5	6.3	6 024	278	0.37
1045-I	2.0	10.1	-	-	3 509	0.82
1045-O	2.0	-	8.1	3 760	-	0.82
SAE P20 Carbon steel substrate coated						
P20-B	2.0	13.9	6.8	4 251	426	0.73
P20-I	2.0	11.3	-	-	2 396	0.85
P20-O	2.0	-	5.9	6 826	-	0.92

[a] Mean value calculated by the modified Jönsson and Hogmark's model.

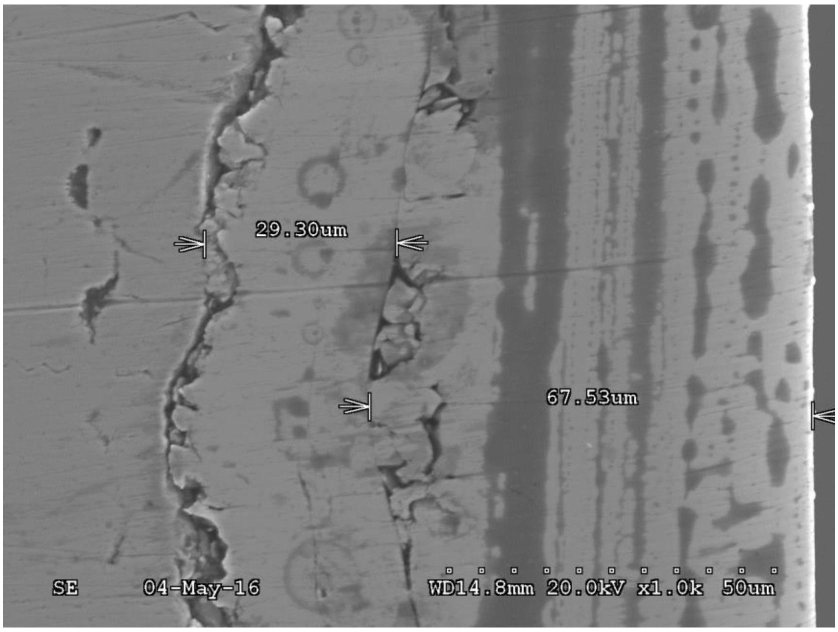

Figure III.3-20. SEM micrograph illustrating the dimension of each single layer of the bilayer electroless Ni-P coating (sample named 1020-B)

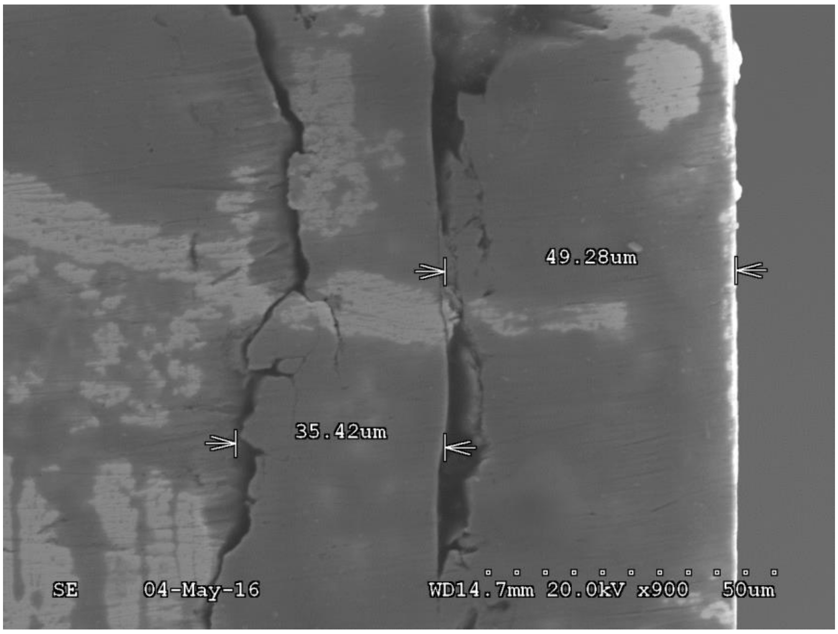

Figure III.3-21. SEM image of sample labeled 1020-B showing the dimension of each layer of the bilayer electroless Ni-P coating.

Moreover, to corroborate the values obtained by the modified Jönsson and Hogmark's model to multilayer coated systems, the hardness behavior from samples 1020-O (electroless Ni-P coating with a heat treatment at 200°C) and the sample 1020-I (electroless Ni-P coating with a heat treatment at 400°C) were described by the same model but considering it as a monolayer coating. Figure III.3-18 and Figure III.3-19 illustrate the hardness variation as function of the indentation depth of both coating composing the bilayer system studied. It is perceived that the obtained values from the hardness of each layer by applying the modified Jönsson and Hogmark's model to the bilayer coating systems agree when the model is implemented to the monolayer coating deposited on the carbon steel substrates.

Alternatively, the analysis of the elastic modulus of the bilayer system is based on the fact that the contact stiffness should be not constant when the elastic modulus varies with the displacement of the indenter into the material surface. Following the reasoning of the relation suggested by Doerner and Nix [61] to deduce the elastic modulus from a film-substrate system, a model to evaluate the bilayer Ni-P coating system is proposed to estimate the elastic modulus of the material by continuous multicycle tests, extensible to be used at nanoscale range and also to a multilayer coating system. With the aim of describe the elastic modulus of the bilayer system as a function of the depth, a macroscopic model will be defined from the point of view of the mechanical coupling, setting a physical meaning for the adjustable parameter for the bilayer system. From the following expression:

$$\frac{dh}{dP} = \frac{1}{2\beta E_{RC}}\sqrt{\frac{\pi}{A_C}} \qquad \text{(III.3-2)}$$

Where E_{RC} is the composite reduced elastic modulus from the film-substrate system, and on the basis of a harmonic mixture law, the composite contact stiffness can be expressed as it follows:

$$\frac{dh}{dP} = \frac{1}{S_C} = C_{\mathrm{f}} + \frac{1 - f_{\mathrm{n}}}{S_{\mathrm{S}}} + \frac{f_{\mathrm{n}}}{S_{\mathrm{F}}} \qquad \text{(III.3-3)}$$

Where S_C, S_S and S_{F} are the composite contact stiffness, contact stiffness from the substrate, and contact stiffness from the film, respectively, C_{f} is the frame compliance of the instrument, and f_n stands for a weight function to estimate the contribution of contact stiffness from the film and substrate to the composite contact stiffness. Tricoteaux *et al.* [112] proposed an expression based in Eq. (III.3-3), and recognizing the necessary correction to be considered in Eq. (III.3-2) it was expressed as following:

$$\frac{1}{S_C} = C_{\mathrm{f}} + \frac{1}{2\beta}\sqrt{\frac{\pi}{A_C}}\frac{f_{\mathrm{n}}}{\gamma_{\mathrm{F}} E_{RF}} + \frac{1}{2\beta}\sqrt{\frac{\pi}{A_C}}\left(\frac{1 - f_{\mathrm{n}}}{\gamma_{\mathrm{S}} E_{RS}}\right) \qquad \text{(III.3-4)}$$

Where E_{RF} and E_{RS} are the reduced elastic modulus from the film and substrate, respectively, and f_{n} is the weight function defined by the authors to compute the contribution of film and substrate to the composite contact stiffness which is the one advanced by Korsunsky *et al.* [135], written below:

$$f_{\mathrm{n}} = \frac{1}{1 + k_k\left(\frac{h_C}{t_F}\right)^2} \qquad \text{(III.3-5)}$$

According with this proposal, the model to be applied to a multilayer coating system, for the first layer, the volume fraction $a_{\mathrm{F}}^{(1)}$ contributing with the composite elastic modulus is defined as follows:

$$a_{\mathrm{F}}^{(1)} = \begin{cases} 1 & \text{if } h < \dfrac{t_F^{(1)}}{100} \\ \dfrac{1}{1 + k_k^{(1)}\left(\dfrac{h_C - t_F^{(1)}}{t_F^{(1)}}\right)^2} & \text{otherwise} \end{cases} \qquad \text{(III.3-6)}$$

© 2016 Tous droits réservés. lilliad.univ-lille.fr

Where $t_F{}^{(1)}$ is the thickness of the outermost layer, $k_k{}^{(1)}$ is a fitting parameter depending on material, and h_C represents the contact indentation depth, and

$$a_{\mathrm{F}}{}^{(j)} = \begin{cases} 1 - \sum_{i=1}^{j-1} a_{\mathrm{F}}{}^{(i)} & \text{if } h < \frac{1}{100}\sum_{i=1}^{j} t_{\mathrm{F}}{}^{(i)} \\ \dfrac{1}{1 + k_k{}^{(j)}\left(\dfrac{h_C - \frac{1}{100}\sum_{i=1}^{j} t_{\mathrm{F}}{}^{(i)}}{\sum_{i=1}^{j} t_{\mathrm{F}}{}^{(i)}}\right)^2} - \dfrac{1}{1 + k_k{}^{(j-1)}\left(\dfrac{h_C - \frac{1}{100}\sum_{i=1}^{j-1} t_{\mathrm{F}}{}^{(i)}}{\sum_{i=1}^{j-1} t_{\mathrm{F}}{}^{(i)}}\right)^2} & \text{otherwise} \end{cases} \tag{III.3-7}$$

Where the volume fraction of the jth layer $a_{\mathrm{F}}{}^{(j)}$ $(j = 2, \cdots, N)$ is used to represent the effective volume fraction of each layer contributing to the composite contact stiffness; for the jth layer the parameter $k_k{}^{(j)}$ denotes a fitting parameter to estimate by a non-linear least square regression analysis, and $t_{\mathrm{F}}{}^{(i)}$ represents its thickness. In a multilayer coating system with N layers, the influence of the substrate material $a_{\mathrm{F}}{}^{(S)}$ contributing with the composite contact stiffness is evaluated by:

$$a_{\mathrm{F}}{}^{(S)} = 1 - \sum_{i=1}^{N} a_{\mathrm{F}}{}^{(i)} \tag{III.3-8}$$

In this manner the composite contact stiffness expressed in the Eq. (III.3-3) for a monolayer system, can be rewritten for a multilayer coating system as follows:

$$\frac{1}{S_{\mathrm{C}}} = C_{\mathrm{f}} + \frac{a_{\mathrm{F}}{}^{(S)}}{S_{\mathrm{S}}} + \sum_{i=1}^{N} \frac{a_{\mathrm{F}}{}^{(i)}}{S_{\mathrm{F}}{}^{(i)}} \tag{III.3-9}$$

Where

$$\frac{1}{S_{\mathrm{F}}{}^{(i)}} = \frac{1}{2\beta}\sqrt{\frac{\pi}{A_C}}\frac{1}{\gamma_{\mathrm{F}}{}^{(i)} E_{RF}{}^{(i)}} \tag{III.3-10}$$

And

$$\frac{1}{S_{\mathrm{S}}} = \frac{1}{2\beta}\sqrt{\frac{\pi}{A_C}}\frac{1}{\gamma_{\mathrm{S}} E_{RS}} \tag{III.3-11}$$

Implementing the Eq. (III.3-6) through (III.3-11), the composite contact stiffness can be computed as function of indentation depths for a multilayer coating system, with the reduced elastic modulus of film of each layer ${E_{RF}}^{(i)}$ and ${k_k}^{(i)}$ as fitting parameters. The value of the reduced elastic modulus of each coating layer, ${E_{RF}}^{(i)}$ and the constant ${{t_F}^{(1)}}^{(i)}$ are estimated by means of a non-linear least square fitting analysis, well-knowing the elastic modulus of the substrate. Nevertheless, the layer thickness ${t_F}^{(i)}$ and the reduced modulus of substrate (E_{RS}) could be also adjustment parameters.

Figure III.3-22 shows the reciprocal of the contact stiffness from the multicycle instrumented test. It is distinguished that if a straight line is used to describe the variation of the total compliance versus the reciprocal of the indentation contact depth then the intercept of this mast will be not the origin of the coordinate system. Nevertheless, by analyzing the behavior of this variable it will be possible to compute the elastic modulus from the bilayer Ni-P coating system, and more generally, from a multilayer coating system.

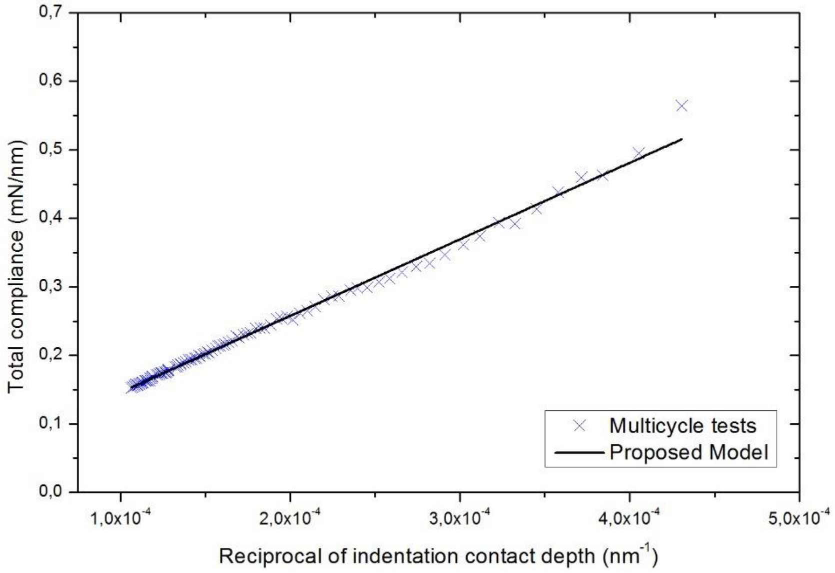

Figure III.3-22. Contact Stiffness from multicycle indentation tests performed on a bilayer Ni-P coating system, described by the model presented in the Eqs. (III.3-6) through (III.3-11) .

Table III.3-2 collects the reduced elastic modulus from the substrate, and the outer and innermost layers of the bilayer electroless coating system. By applying the non-linear least square regression analysis to the advanced model, the fitting parameters considering in the expression are the reduced modulus of each layer, *i.e.* E_{RF1} and E_{RF2}, the thickness of each layer, it means, t_{F1} and t_{F2}, and the parameter depending on the material $k_{k_{F1}}$ and $k_{k_{F2}}$. First, all parameters were considered as free parameters, nevertheless with this condition the model did not converge. But, taking into account that the reduced elastic modulus from the inner layer, considered as crystalline material compared with the outermost amorphous layer, one condition was imposed, the reduced elastic modulus from the inner layer must be greater than the reduced elastic modulus from the outermost layer. According with this consideration, from Table III.3-2 it can be seen that the model applied to the bilayer system did not discriminate the two reduced elastic modulus; this solution in some way could be ascribed to the similar reduced elastic modulus in both layer from the bilayer electroless Ni-P coating, owing to the elastic modulus of coatings was not affected by the temperature. However, it is expected that with a more dissimilar composite material the model will be performed in a better manner.

Table III.3-2. Reduced elastic modulus and fitting parameter values by applying the model proposed in this work.

Sample Code	E_S (GPa)	E_{RF1} (GPa)	E_{RF2} (GPa)	t_{F1} (µm)	t_{F2} (µm)	k_{kF1}	k_{kF2}	C_f	R^2
1020-B	180	142	142	47	28	0.85	3.43	0.10	0.98
1045-B	180	155	155	22	16	0.54	3.89	0.14	0.98
P20-B	180	141	141	13	14	0.75	7.60	0.11	0.99

With the values assessed by this model, the description of elastic modulus as function of the indentation depth is illustrated in Figure III.3-23. It can be noted how the model fits the data obtained from the continuous multicycle indentation test by taking into account the contribution of the elastic moduli and compliance from each and every single layer to the computed composite elastic modulus at each cycle.

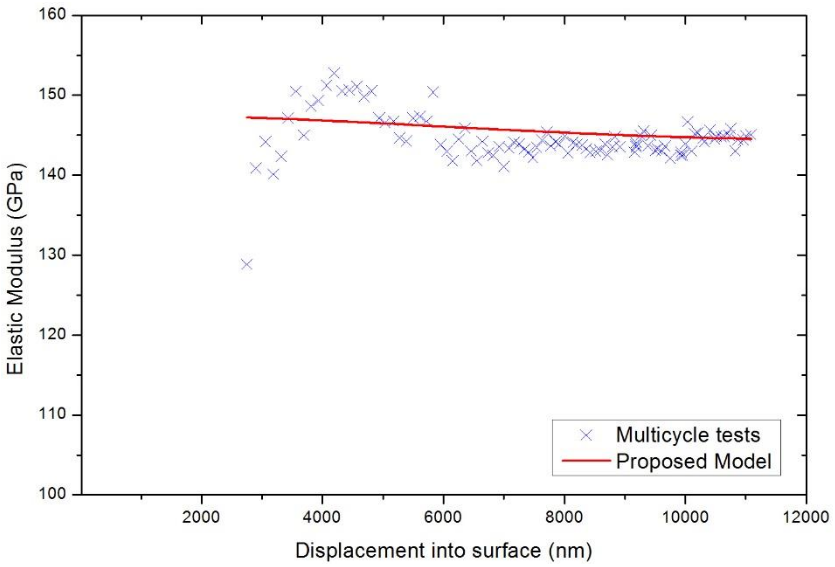

Figure III.3-23.Composite elastic modulus from multicycle indentation tests performed on a bilayer Ni-P coating system, predicted on the basis of the model presented in this section.

III.3.4. Conclusions

The mechanical properties of a bilayer Ni-P coating system were determined by applying models to discriminate the contribution of each layer from a bilayer coating system to the composite elastic modulus and hardness. To evaluate the hardness variation, the proposal of Puchi-Cabrera *et al.* [71] modifying the Jönsson and Hogmark's model [67] in order to be able to separate the contribution of each layer to the total composite hardness measurement was put into practice. According with this model and considering that the deposition of the bilayer system was effectuated on three different carbon steel samples, the hardness of the two layers were found to be between 10.1 and 12.1 GPa for the innermost layer, and between 5.9 and 8.1 GPa for the outermost layer. On the other hand, the elastic modulus was computed in the basis of the total compliance of the systems, it means, as a function of the reciprocal of the contact stiffness of the bilayer coating system determined from the multicycle instrumented indentation test. On the basis of the model advanced by Tricoteaux *et al*. [112] for monolayer coated material and implementing the weight function suggested by Konsursky *et al.* [135], a new approach is advanced to be applied to multilayer coating systems. By considering this proposal, suggested in this work, the elastic modulus of both layers were found to be between 141 GPa and 155 GPa, where the model shows that the both layers have the same elastic modulus or that there is only a small difference between them.

General Conclusions

The determination of mechanical properties such as the elastic modulus and hardness requires the treatment of a selected data derived from the load-displacement curve resulting from instrumented indentation tests. One of the most important variables to estimate is the contact area, A_C, depending on the mechanical response of the surface beneath the indenter. The defect of the rounded tip also must be estimated particularly when analysis is achieved at low loads, *i.e.* at low displacements into surface. It is important to emphasize that material and geometric corrections described in the literature must be done when performing the multicycle indentation test at the microscale range, above all the blunt defect of the indenter tip owing to that if it is neglected the variations on the elastic modulus would be very large, and the hypothesis that the elastic modulus of the material remains constant would not be true. When material hardness is evaluated the indentation size effect (ISE) describe the variations in this property at different scales of measurement. Regarding the models to analyze film-substrate systems, it can be noted that in these models that the contribution of the substrate and film to the composite elastic modulus and hardness values must be calculated, which is defined by a weight function (and consequently, the volume fraction) normally expressed as the ratio of film thickness to the indentation depth.

Mechanical properties of carbon steel samples, *i.e.* the hardness and elastic modulus, were evaluated from multicycle indentation tests. Regarding the obtained values, it can be stated that the elastic modulus remains constant as the indentation depth increases until the cycle 100. The predominant mode of deformation around the indenter was found to be the phenomenon of pile-up, by means of the parameter Δ suggested by Yetna *et al.* [100], which remains greater than 0.83 for all the continuous multicycle indentation tests. The computed elastic modulus from the carbon steel samples was found to be between 158 and 190 GPa with a standard deviation around 5%. According to the evaluation of hardness, it could be described by the Li and Bradt's model [103] and the model suggested by Chicot [104] when tests were performed at the microscale range. Both models showed that the material hardness under the increasing loadings by a continuous multicycle protocol is associated to the indentation size effect. The Martens hardness for the three carbon steel samples were found to be between 1.60 and 2.84 GPa.

Additionally, from the obtained data acquired by CSM tests, a new approach to compute the contact stiffness, by replacing the contact area function proposed by Chicot *et al.* [27] or the model suggested by Oliver and Pharr [1] into the explicit expression of the contact stiffness, agrees when using both contact area functions. The models overlapped practically each other when they are applying in the range $100 < h_{\max} < 1900$ nm. Conversely, by replacing both models and applying a non-linear least square analysis in the range $5 < h_{\max} < 50$ nm, the contact area function proposed by Chicot *et al.* [27] describes better the values of the experimental contact stiffness than the model suggested by Oliver and Pharr [1]. According to this proposal by applying the contact area function developed by Chicot *et al.* [27] the blunt defect of the indenter tip equals to 30.5 ± 1.9 nm when nanoindentation tests is performed on a fused silica sample. As well as the preceding analysis effectuated at the microscale range from carbon steel samples, the deformation around the indenter (the phenomena of sink-in or pile-up) must be taken into account in the computation of the elastic modulus. From these carbon steel samples, the elastic modulus were found to be between 188 and 214 GPa.

The solution precursor plasma sprayed hydroxyapatite coatings (SPPS-HA) sprayed on stainless steel substrate were tested by a multicycle microindentation analysis to assess their mechanical properties such as the elastic modulus and hardness of the coatings. Elastic modulus and hardness of the SPPS-HA coatings were found to be from 5.0 GPa to 22.0 GPa and from 0.04 to 0.17 GPa, respectively. Coatings sprayed using a high concentrated solution had an average elastic modulus and hardness nearly two times greater than the less concentrated ones. Moreover, mechanical properties obtained from SPPS-HA coatings were smaller in comparison to the values obtained using conventional plasma spraying process that can be attributed to the unique microstructural features present in the coatings. By applying a different approach, the influence of the compaction of the coatings on hardness measurements initiates between 50% to 85% of the coating thickness, according with the obtained values of the fitting parameter κ from the advanced model in this work. The sample coating having the highest crystallinity that was prepared from a solution of high concentration has the greatest elastic modulus (22.0 GPa) and hardness (0.17 GPa) among all coatings. It is necessary to highlight that the proposed novel approach to quantify the hardness of porous and densified hydroxyapatite coating allows to describe the hardness behaviors of this coating when it is submitted to continuous and increasing loading-unloading sequences which is an important aspect to be take into account on tribological applications. On the other hand, the studied mechanical properties of coatings from solution precursors of low concentration was not significantly influenced by the crystallinity volume fraction having only an average hardness and elastic modulus of 0.05 GPa to 6.7 GPa, respectively. Hardness and elastic modulus of the samples were described as a function of the crystallinity volume fraction in order to predict its behavior for the estimation of the corresponding crystallinity volume fraction to obtain a bone-like microstructure. The values of the mechanical parameters increase with the crystallinity volume fraction from $H_a = 0.07$ and $E_a = 6.4$ GPa to $H_{Cr} = 0.29$GPa and $E_{Cr} = 41.4$ GPa, which correspond to the mechanical properties of the amorphous and the crystalline phases, respectively. More interesting, to link the mechanical properties to its potential biomedical applications, the crystallinity volume fraction corresponding to the elastic modulus of a bone-like microstructure can be predicted from the implemented models and it should be between 0.56 and 0.86.

The mechanical properties of a bilayer Ni-P coating system were studied from multicycle instrumented indentation test by applying additionally models to discriminate the contribution of each layer to the composite elastic modulus or hardness. To evaluate the variation of hardness, the modified model of Jönsson and Hogmark was applied. According with this model, the hardness of the two layers were found to be between 10.1 and 12.1 GPa for the innermost layer, and between 5.9 and 8.1 GPa for the outermost layer. The elastic modulus was computed in the basis of the computation of the total composite compliance of the systems, it means, the evaluation of the composite elastic modulus was model as a function of the reciprocal of the experimental contact stiffness of the bilayer coating system determined from the multicycle instrumented indentation test at the microscale range. On the basis of the model proposeed by Tricoteaux *et al.* [112] for monolayer coated material and implementing the weight function suggested by Konsursky *et al.* [135], a new approach is suggested to be applied to multilayer coating systems. By considering this proposal, suggested in this work, the elastic modulus of both layers were found to be between 141 GPa and 155 GPa, where the model shows that the both layers have the same elastic modulus or that there is only a small difference between them, owing to the elastic modulus was not affected by the heat treatment.

It is envisaged that further investigations to continue as the application of multicycle indentation tests in the range of the macroscale for very thick coatings; using the multicycle indentation tests to the study of highly heterogeneous materials (like materials for brakes) for which the nanoindentation gives only very localized information; the characterization of the "damage" of materials under the effect of the multicycle indentation; study and modeling of cracking of brittle materials subjected to the multicycle indentation test; simulation of the multicycle indentation test by FEM analysis; and, using the multicycle indentation tests to the study of the adhesion of thick coatings and for the detection of the initiation charge of the interfacial cracking.

© 2016 Tous droits réservés. lilliad.univ-lille.fr

References

[1] W. Oliver et G. Pharr, «An improved technique for determining hardness and elastic modulus using load and displacement sensing indentation experiments,» *Journal of Materials Research,* vol. 6, n° 17, p. 1564–1583, 1992.

[2] J. Antunes, J. Fernandes, N. Sakharova, M. Oliveira et L. Menezes, «On the determination of the Young's modulus of thin films using indentation tests,» *International Journal of Solids and Structures,* vol. 44, n° 125–26, p. 8313–8334, 2007.

[3] D. Chicot, F. Roudet, A. Soom et J. Lesage, «Interpretation of instrumented hardness measurements on stainless steel with different surface preparations,» *Surface Engineering,* vol. 23, n° 11, p. 32–39, 2007.

[4] Y. Fenga et T. Zhang, «Determination of fracture toughness of brittle materials by indentation,» *Acta Mechanica Solida Sinica,* vol. 28, n° 13, p. 221–234, 2015.

[5] M. He, F. Lib, J. Caib et B. Chenb, «An indentation technique for estimating the energy density as fracture toughness with Berkovich indenter for ductile bulk materials,» *Theoretical and Applied Fracture Mechanics,* vol. 56, n° 12, p. 104–111, 2011.

[6] M. Yetna N'Jock, F. Roudet, M. Idriss, O. Bartier et D. Chicot, «Work-of-indentation coupled to contact stiffness for calculating elastic modulus by instrumented indentation,» *Mechanics of Materials,* vol. 94, p. 170–179, 2016.

[7] D. Chicot, E. Puchi-Cabrera, R. Aumaitre, G. Bouscarrat, C. Dublanche-Tixier, F. Roudet et M. Staiab, «Elastic modulus of TiHfCN thin films by instrumented indentation,» *Thin Solid Films,* vol. 552, p. 304–313, 2012.

[8] S. Zameer Abbas, F. Ahmad Khalid et H. Zaighama, «Indentation and deformation behavior of FeCo-based bulk metallic glass alloys,» *Materials Science and Engineering: A,* vol. 654, p. 426–435, 2016.

[9] P. Nogning Kamta, A. Mejias, F. Roudet, G. Louis, M. Touzin et D. Chicot, «Indentation creep analysis of T22 and T91 chromium based steels,» *Materials Science and Engineering: A,* vol. 652, p. 315–324, 2016.

[10] D. Chicot, «Hardness length-scale factor to model nano- and micro-indentation size effects,» *Materials Science and Engineering: A,* vol. 499, n° 11–2, p. 454–461, 2009.

[11] S. Bec, A. Tonck, J. Georges, E. Georges et J. Loubet, «Improvements in the indentation method with a surface force apparatus,» *Philosophical Magazine A,* vol. 74, n° 15, p. 1061–1072, 1996.

[12] A. Fischer-Cripps, «Nanoindentation Testing,» chez *Nanoindentation*, Second éd., vol. 6, New South Wales, Springer, 2011, p. 21–37.

[13] J. Field et R. Telling, The Young's Modulus and Poisson's ratio of Diamond, Cambridge: PCS Cavendish Lab., 1999, p. 850–854.

[14] A. Fischer-Cripps, «Critical review of analysis and interpretation of nanoindentation test data,» *Surface and Coatings Technology,* vol. 200, n° 114–15, p. 4153–4165, 2006.

[15] J. Pethica et W. Oliver, «Mechanical properties of nanometer volumes of material: use of the elastic response of small area indentations,» chez *Thin films: stresses and mechanical properties*, vol. 130, J. Bravman, W. Nix, D. Barnett et D. Smith, Éds., Pittsburgh (PA), Materials Research Society, 1989, p. 13–23.

[16] S. Syed Asif et J. Pethica, «Nano scale creep and the role of defects,» chez *Thin films: stresses and mechanical properties*, vol. 436, W. Gerberich, H. Gao, J. Sundgren et S. Baker, Éds., Pittsburgh (PA), Materials Research Society, 1997, p. 201–206.

[17] W. Oliver et G. Pharr, «Measurement of hardness and elastic modulus by instrumented indentation: Advances in understanding and refinements to methodology,» *Journal of Materials Research,* vol. 19, n° 11, p. 3–20, 2004.

[18] J. Thurn et R. Cook, «Simplified area function for sharp indenter tips in depth-sensing indentation,» *Journal of Materials Research,* vol. 17, n° 15, p. 1143–1146, 2002.

[19] L. Berla, A. Allen, S. Min Han et N. W. , «A physically based model for indenter tip shape calibration for nanoindentation,» *Journal of Materials Research,* vol. 25, n° 14, p. 735–745, 2010.

[20] J. Gong, H. Miao et Z. Peng, «On the contact area for nanoindentation tests with Berkovich indenter: case study on soda-lime glass,» *Materials Letters,* vol. 58, n° 17–8, p. 1349–53, 2004.

[21] M. Troyon et L. Huang, «Comparison of different analysis methods in nanoindentation and influence on the correction factor for contact area,» *Surface and Coatings Technology,* vol. 201, n° 13–4, p. 1613–1619, 2006.

[22] M. Troyon et L. Huang, «Correction factor for contact area in nanoindentation measurements,» *Journal of Materials Research,* vol. 20, n° 13, p. 610–617, 2005.

[23] Y.-T. Cheng et C.-M. Cheng, «Further analysis of indentation loading curves: Effects of tip rounding on mechanical property measurements,» *Journal of Materials Research,* vol. 13, n° 14, p. 1059–1064, 1998.

[24] M. Troyon et M. Martin, «A critical examination of the P-h2 relationship in nanoindentation,» *Applied Physics Letter,* vol. 83, p. 863–865, 2003.

[25] C. Shih, M. Yang et J. Li, «Effect of tip radius on nanoindentation,» *Journal of Materials Research,* vol. 6, p. 2623–2628, 1991.

[26] D. Chicot, F. Roudet, V. Lepingle et G. Louis, «Strain gradient plasticity to study hardness behavior of magnetite (Fe3O4) under multicyclic indentation,» *Journal of Materials Research,* vol. 24, n° 13, p. 749–759, 2009.

[27] D. Chicot, M. Yetna N'Jock, E. Puchi-Cabrera, A. Iost, M. Staia et G. Louis, «A contact area function for Berkovich nanoindentation: Application to hardness determination of a TiHfCN thin film,» *Thin Solid Films,* vol. 558, p. 259–266, 2014.

[28] K. Herrmann, N. Jennett, W. Wegener, J. Meneve, K. Hasche et R. Seemann, «Progress in determination of the area function of indenters used for nanoindentation,» *Thin Solid Films,* vol. 377–378, p. 394–400, 2000.

[29] K. Herrmann, K. Hasche, F. Pohlenz et R. Seemann, «Characterisation of the geometry of indenters used for the micro- and nanoindentation method,» *Measurement,* vol. 29, n° 13, p. 201–207, 2001.

[30] A. Franco Jr., G. Pintaúde, A. Sinatora, C. Pinedo et A. Tschiptschin, «The use of a Vickers indenter in depth sensing indentation for measuring elastic modulus and Vickers hardness,» *Materials Research,* vol. 7, n° 13, p. 483–491, 2004.

[31] H. Bei, E. George, J. Hay et G. Pharr, «Influence of Indenter Tip Geometry on Elastic Deformation during Nanoindentation,» *Physical Review Letters,* vol. 95, p. 045501 (1–4), 2005.

[32] J. Antunes, A. Cavaleiro, L. Menezes, M. Simoes et J. Fernandes, «Ultra-microhardness testing procedure with Vickers indenter,» *Surface and Coatings Technology,* vol. 149, n° 11, p. 27–35, 2002.

[33] D. Chicot, F. Roudet, A. Zaoui, G. Louis et V. Lepingle, «Influence of visco-elasto-plastic properties of magnetite on the elastic modulus: Multicyclic indentation and theoretical studies,» *Materials Chemistry and Physics,* vol. 119, n° 11–2, p. 75–81, 2010.

[34] J. Antunes, L. Menezes et J. Fernandes, «Three-dimensional numerical simulation of Vickers indentation tests,» *International Journal of Solids and Structures,* vol. 43, n° 13–4, p. 784–806, 2006.

[35] A. Bolshakov et G. Pharr, «Influences of pile-up on the measurement of mechanical properties by load and depth sensing indentation techniques,» *Journal of Materials Research,* vol. 13, n° 14, p. 1049–1058, 1998.

[36] Y.-T. Cheng et C.-M. Cheng, «Scaling approach to conical indentation in elastic–plastic solids with work hardening,» *Journal of Applied Physics,* vol. 84, n° 13, p. 1284–1291, 1998.

[37] Y.-T. Cheng et C.-M. Cheng, «Scaling relationships in conical indentation of perfectly elastic–plastic solids,» *International Journal of Solids Structures,* vol. 36, n° 18, p. 1231–1243, 1999.

[38] R. King, «Elastic analysis of some punch problems for layered medium,» *International Journal of Solids and Structures,* vol. 23, n° 112, p. 1657–1664, 1987.

[39] M. Dao, N. Chollacoop, K. Van Vliet, T. Venkatesh et S. Suresh, «Computational modeling of the forward reverse problems in instrumented sharp indentation,» *Acta Materialia,* vol. 49, n° 119, p. 3899–3918, 2001.

[40] J. Hay, A. Bolshakov et G. Pharr, «A critical examination of the fundamental relations used in the analysis of nanoindentation data,» *Journal of Materials Research,* vol. 14, n° 16, p. 2296–2305, 1999.

[41] M. Yetna N'jock, D. Chicot, J. Ndjaka, J. Lesage, X. Decoopman, F. Roudet et A. Mejias, «A criterion to identify sinking-in and piling-up in indentation of materials,» *International Journal of Mechanical Sciences,* vol. 90, p. 145–150, 2015.

[42] A. Giannakopoulos et S. Suresh, «Determination of elastoplastic properties by instrumented sharp indentation,» *Scripta Materialia,* vol. 40, n° 110, p. 1191–1198, 1999.

[43] Y.-T. Cheng et C.-M. Cheng, «Scaling, dimensional analysis, and indentation measurements,» *Materials Science and Engineering: R: Reports,* vol. 44, n° 14–5, p. 91–149, 2004.

[44] H. Li et R. Bradt, «The microhardness indentation load/size effect in rutile and cassiterite single crystals,» *Journal of Materials Science,* vol. 28, n° 14, p. 917–926, 1993.

[45] W. Nix et H. Gao, «Indentation size effects in crystalline materials: A law for strain gradient plasticity,» *Journal of the Mechanics and Physics of Solids,* vol. 46, n° 13, p. 411–425, 1998.

[46] Q. Ma et D. Clarke, «Size dependent hardness of silver single crystals,» *Journal of Materials Research,* vol. 10, n° 14, p. 853–863, 1995.

[47] B.-D. Michels et G. Frischat, «Microhardness of chalcogenide glasses of the system Se-Ge-As,,» *Journal of Materials Science,* vol. 17, n° 12, p. 329–334, 1982.

[48] F. Frohlich, P. Grau et W. Grellmann, «Performance and analysis of recording microhardness tests,» *Physica Status Solidi (A),* vol. 42, n° 11, p. 79–89, 1977.

[49] W. Oliver, R. Hutchings et J. Pethica, «Microindentation Techniques in Materials Science and Engineering,» chez *ASTM STP 899*, P. Blau et B. Lawn, Éds., Philadelphia, PA, ASTM, 1986, p. 90–108.

[50] J. Gong, J. Wu et Z. Guan, «Examination of the indentation size effect in low-load vickers hardness testing of ceramics,» *Journal of the European Ceramic Society,* vol. 19, n° 115, p. 2625–2631, 1999.

[51] J. Gong, Z. Zhao, Z. Guan et H. Miao, «Load-dependence of Knoop hardness of Al2O3-TiC composites,» *Journal of the European Ceramic Society,* vol. 20, n° 112, p. 1895–1900, 2000.

[52] K. Sangwal, B. Surowska et P. Błaziak, «Analysis of the indentation size effect in the microhardness measurement of some cobalt-based alloys,» *Materials Chemistry and Physics,* vol. 77, n° 12, p. 511–520, 2003.

[53] L. Shen et K. Zeng, «Comparison of mechanical properties of porous and non-porous low-k dielectric films,» *Microelectronic Engineering,* vol. 71, n° 12, p. 221–228, 2004.

[54] G. Taylor, «The Mechanism of Plastic Deformation of Crystals. Part I. Theoretical,» *Proceedings of the Royal Society of London. Series A, Containing Papers of a Mathematical and Physical Character,* vol. 145, n° 1855, p. 362–387, 1934.

[55] D. Lam et A. Chong, «Effect of cross-link density on strain gradient plasticity in epoxy,» *Materials Science and Engineering: A,* vol. 281, n° 11–2, p. 156–161, 2000.

[56] R. Abu Al-Rub et G. Voyiadjis, «Analytical and experimental determination of the material intrinsic length scale of strain gradient plasticity theory from micro- and nano-indentation experiments,» *International Journal of Plasticity,* vol. 20, n° 16, p. 1139–1182, 2004.

[57] J. Bucaille, A. Rossoll, B. Moser, S. Stauss et J. Michler, «Determination of the matrix in situ flow stress of a continuous fibre reinforced metal matrix composite using instrumented indentation,,» *Materials Science and Engineering: A,* vol. 369, n° 11–2, p. 82–92, 2004.

[58] Y. Cao, Z. Xue, X. Chen et D. Raabe, «Correlation between the flow stress and the nominal indentation hardness of soft metals,» *Scripta Materialia,* vol. 59, n° 15, p. 518–5218, 2008.

[59] D. Chicot, L. Gil, K. Silva, F. Roudet, E. Puchi-Cabrera, M. Staia et D. Teer, «Thin film hardness determination using indentation loading curve modelling,» *Thin Solid Films,* vol. 518, n° 119, p. 5565–5571, 2010.

[60] D. Chicot, H. Ageorges, M. Voda, G. Louis, M. Ben Dhia, C. Palacio et S. Kossman, «Hardness of thermal sprayed coatings: Relevance of the scale of measurement,» *Surface and Coatings Technology,* vol. 268, n° 125, p. 173–179, 2015.

[61] M. Doerner et W. Nix, «A method for interpreting the data from depth-sensing indentation instruments,» *Journal of Materials Research,* vol. 1, n° 14, p. 601–609, 1986.

[62] J. Menčík, D. Munz, E. Quandt, E. Weppelmann et M. Swain, «Determination of elastic modulus of thin layers using nanoindentation,» *Journal of Materials Research,* vol. 12, n° 19, p. 2475–2484, 1997.

[63] H. Gao, C. Chiu et J. Lee, «Elastic contact versus indentation modeling of multi-layered materials,» *International Journal of Solids and Structures,* vol. 29, n° 120, p. 2471–2492, 1992.

[64] A. Korsunsky, M. McGurk, S. Bull et T. Page, «On the hardness of coated systems,» *Surface and Coatings Technology,* vol. 99, n° 11–2, p. 171–183, 1998.

[65] E. Puchi-Cabrera, «A new model for the computation of the composite hardness of coated systems,» *Surface and Coatings Technology,* vol. 160, n° 12–3, p. 177–186, 2002.

[66] P. Liu, F. Wan et Q. Zhan, «A model to evaluate the nano-indentation hardness of ion-irradiated materials,» *Nuclear Instruments and Methods in Physics Research Section B: Beam Interactions with Materials and Atoms,* vol. 342, p. 13–18, 2015.

[67] B. Jönsson et S. Hogmark, «Hardness measurements of thin films,» *Thin Solid Films,* vol. 114, n° 13, p. 257–269, 1984.

[68] E. Puchi-Cabrera, M. Staia et A. Iost, «A description of the composite elastic modulus of multilayer coated systems,» *Thin Solid Films,* vol. 583, p. 177–193, 2015.

[69] K. Rahmoun, A. Iost, V. Keryvin, G. Guillemot et N. C. Sari, «A multilayer model for describing hardness variations of aged porous silicon low-dielectric-constant thin films,» *Thin Solid Films,* vol. 518, n° 11, p. 213–221, 2009.

[70] F. Cleymand, O. Ferry, R. Kouitat, A. Billard et J. von Stebut, «Influence of indentation depth on the determination of the apparent Young's modulus of bi-layer material: Experiments and numerical simulation,» *Surface and Coatings Technology,* vol. 200, n° 11–4, p. 890–893, 2005.

[71] E. Puchi-Cabrera, M. Staia et A. Iost., «Modeling the composite hardness of multilayer coated systems,» *Thin Solid Films,* vol. 578, p. 53–62, 2015.

[72] H. Bückle, L'essai de microdureté et ses applications, vol. 90, Paris: Publications Scientifiques et Techniques du Ministère de l'Air, 1960.

[73] H. Bückle, Use of the Hardness Test to Determine Other Materials Properties, vol. Science of Hardness Testing and Its Research Applications, J. Westbrook et H. Conrad, Éds., Ohio: ASM, Metals park, 1971, p. 453.

[74] A. Iost, D. Najjar et R. Hellouin, «Modelling of the Vickers hardness of paint coatings deposited on metallic substrates,» *Surface and Coatings Technology,* vol. 165, n° 12, p. 126–132, 2003.

[75] R. Saha et W. Nix, «Effects of the substrate on the determination of thin film mechanical properties by nanoindentation,» *Acta Materialia,* vol. 50, p. 23–38, 2002.

[76] X. Chen et J. Vlassak, «Numerical study on the measurement of thin film mechanical properties by means of nanoindentation,» *Journal of Materials Research,* vol. 16, n° 110, p. 2974–2982, 2001.

[77] Y. Benarioua, A. Mejias, F. Roudet, A. Iost et D. Chicot, «Hardness-load modelling applied to multilayer galvanised coatings,» *Surface Engineering,* vol. 32, n° 13, p. 194–200, 2016.

[78] J. Klawitter et S. Hulbert, «Application of porous ceramics for the attachment of load bearing internal orthopedic applications,» *Journal of Biomedical Materials Research Symposium,* vol. 2, p. 161–229, 1971.

[79] R. Ayers, L. Wolford, T. Bateman, V. Ferguson et S. Simske, «Qualification of bone ingrowth into porous block hydroxyapatite in humans,» *Journal of Biomedical Materials Research,* vol. 47, p. 54–59, 1999.

[80] A. Zamiri et S. De, «Mechanical properties of hydroxyapatite single crystals from nanoindentation data,» *Journal of the Mechanical Behavior of Biomedical Materials,* vol. 4, n° 12, p. 146–152, 2011.

[81] C. Rodrigues, P. Serricella, A. Linhares, R. Guerdes, R. Borojevic, M. Rossi, M. Duarte et M. Farina, «Characterization of a bovine collagen–hydroxyapatite composite scaffold for bone tissue engineering,» *Biomaterials,* vol. 24, n° 127, p. 4987–4997, 2003.

[82] M. Motskin, D. Wright, K. Muller, N. Kyle, T. Gard, A. Porter et J. Skepper, «Hydroxyapatite nano and microparticles: Correlation of particle properties with cytotoxicity and biostability,» *Biomaterials,* vol. 30, n° 119, p. 3307–3317, 2009.

[83] R. J. Candidato, P. Sokołowski, G. Nana, C. Constantinescu, A. Denoirjean et L. Pawłowski, «Possibility of Developing hydroxyapatite coatings with high purity by solution precursor plasma spray process,» *To be published,* 2016.

[84] D. Vojtěch, M. Novák, M. Zelinková, P. Novák, A. Michalcová et T. Fabián, «Structural evolution of electroless Ni–P coating on Al–12 wt. Si alloy during heat treatment at high temperatures,» *Applied Surface Science,* vol. 255, n° 16, p. 3745–3751, 2009.

© 2016 Tous droits réservés. lilliad.univ-lille.fr

[85] B. Losiewicz, A. Budniok, E. Rowinski, E. Lagiewka et A. Lasia, «Effect of Heat-Treatment on the Mechanism and Kinetics of the Hydrogen Evolution Reaction on Ni—P + TiO2 + Ti Electrodes,» *Journal of Applied Electrochemistry,* vol. 34, n° 14, p. 507–512, 2004.

[86] C. Marozzi et A. Chialvo, «Development of electrode morphologies of interest in electrocatalysis. Part 1: Electrodeposited porous nickel electrodes,» *Electrochimica Acta,* vol. 45, n° 113, p. 2111–2120, 2000.

[87] J.-D. Lin, C.-L. Kuo et C.-J. Hsia, «The influence of microwave-assisted hydrogen plasma treatment on electroless Ni–P coatings,» *Materials Chemistry and Physics,* vol. 137, n° 13, p. 848–858, 2013.

[88] G. Mallory et J. Hajdu, Electroless Plating: Fundamentals and Applications, Orlando: AESF, 1990.

[89] K. Krishnan, S. John, K. Srinivasan, J. Praveen, M. Ganesan et P. Kavimani, «Electroless Ni-P-based composite coatings,» *Metallurgical and Materials Transactions A,* vol. 37, p. 1917–1926, 2006.

[90] K. Keong et W. Sha, «Crystallisation and Phase Transformation Behaviour of Electroless Nickel-Phosphorus Deposits and Their Engineering Properties,» *Surface Engineering,* vol. 18, n° 15, p. 329–343, 2002.

[91] S. Shibli, G. Harikrishnan, V. R. Anupama, K. Chinchu et B. Meena, «Development of nano NiO incorporated nickel–phosphorus coatings for electrocatalytic applications,» *Surface & Coatings Technology,* vol. 262, p. 48–55, 2015.

[92] M. Balat, «Potential importance of hydrogen as a future solution to environmental and transportation problems,» *International Journal of Hydrogen Energy,* vol. 33, n° 115, p. 4013–4029, 2008.

[93] M. Saxe et P. Alvfors, «Advantages of integration with industry for electrolytic hydrogen production,» *Energy,* vol. 32, n° 11, p. 42–50, 2007.

[94] C. Zhang, A. Kanta, H. Yin, A. Boudiba, J. D'Haen, M.-G. Olivier et M. Debliquy, «H2 sensors based on WO3 thin films activated by platinum nanoparticles synthesized by electroless process,» *International Journal of Hydrogen Energy,* vol. 38, n° 16, p. 2929–2935, 2013.

[95] Z. Wang, F. Jia, L. Yu, Z. Qi, Y. Tang and G. Song, "Direct electroless nickelboron plating on AZ91D magnesium alloy," *Surface and Coatings Technology,* vol. 206, p. 3676–3685, 2012.

[96] J. M. A. Ramalho, «Friction and wear of electroless NiP and NiP þ PTFE coatings,» *Wear,* vol. 259, p. 828–834, 2005.

[97] G. Shi, W. Li et Y. Lu, «Fe-based surface activator for electroless nickel deposition on polyester: application to electromagnetic shielding,» *Surface and Coatings Technology,* vol. 253, p. 221–226, 2014.

[98] MTS Systems Corporation, «TestWorks® 4 Software for Nanoindentation Systems,» 2002.

[99] ASTM, «1.03,» chez *Annual Book of ASTM Standards*, Easton, MD: ASTM, 1996.

[100] M. Yetna N'jock, D. Chicot, J. Ndjaka, J. Lesage, X. Decoopman, F. Roudet et A. Mejias, «A criterion to identify sinking-in and piling-up in indentation of materials,» *International Journal of Mechanical Sciences,* vol. 90, p. 145–150, 2015.

[101] D. Chicot, P. d. Baets, M. Staia, E. Puchi-Cabrera, G. Louis, Y. Perez Delgado et J. Vleugels, «Influence of tip defect and indenter shape on the mechanical properties determination by indentation of a TiB2–60B4C ceramic composite,» *International Journal of Refractory Metals and Hard Materials,* vol. 38, p. 102–110, 2013.

[102] S. Kang, Y.-S. Jung, B.-G. Yoo, J.-I. Jang et Y.-K. Lee, «Orientation-dependent indentation modulus and yielding in a high Mn twinning-induced plasticity steel,» *Materials Science and Engineering: A,* vol. 532, p. 500–504, 2012.

[103] H. Li et R. Bradt, «The microhardness indentation load/size effect in rutile and cassiterite single crystals,» *Journal of Materials Science,* vol. 28, n° 14, p. 917–926, 1993.

[104] D. Chicot, «Hardness length-scale factor to model nano- and micro-indentation size effects,» *Materials Science and Engineering A ,* vol. 499, p. 454–461, 2009.

[105] E. Martínez-Pañeda et C. Niordsonb, «On fracture in finite strain gradient plasticity,» *International Journal of Plasticity,* vol. 80, p. 154–167, 2016.

[106] M. Taureza, X. Songb et S. Castagnea, «Depth-dependent stress–strain relation for friction prediction,» *International Journal of Mechanical Sciences,* vol. 86, p. 46–53, 2014.

[107] D. Chicot, S. Puchi-Cabrera, X. Decoopman, F. Roudet, J. Lesage et M. Staia, «Diamond-like carbon film deposited on nitrided 316L stainless steel substrate: A hardness depth-profile modeling,» *Diamond and Related Materials,* vol. 20, n° 110, p. 1344–1352, 2011.

[108] J. Chen et S. Bull, «On the factors affecting the critical indenter penetration for measurement of coating hardness,» *Vacuum,* vol. 83, p. 911–920, 2009.

[109] I. Manika et J. Maniks, «Effect of substrate hardness and film structure on indentation depth criteria for film hardness testing,» *Journal of Physics D: Applied Physics,* vol. 41, p. 074010 (6 pp), 2008.

[110] S. Bulychev, V. Alekhin, M. Shorshorov, A. Ternovskii et G. Shnyrev, «Determining Young's Modulus from the indenter penetration diagram,» *Zavodskaya Laboratoriya,* vol. 41, p. 1137–1140, 1975.

[111] M. B. S. A. V. Shorshorov, «Work of plastic deformation during indenter indentation,» *Soviet Physics - Journal of Experimental and Theoretical Physics,* vol. 26, p. 769–771, 1982.

[112] A. Tricoteaux, G. Duarte, D. Chicot, E. Le Bourhis, E. Bemporad et J. Lesage, «Depth-sensing indentation modeling for determination of Elastic modulus of thin films,» *Mechanics of Materials,* vol. 42, n° 12, p. 166–174, 2010.

[113] U. Ramamurty, S. Jana, Y. Kawamura et K. Chattopadhyay, «Hardness and plastic deformation in a bulk metallic glass,» *Acta Materialia,* vol. 53, n° 13, p. 705–717, 2005.

[114] R. Vaidyanathan, M. Dao, G. Ravichandran et S. Suresh, «Study of mechanical deformation in bulk metallic glass through instrumented indentation,» *Acta Materialia,* vol. 49, n° 118, p. 3781–3789, 2001.

[115] M. F. Hasan, J. Wang et C. Berndt, «Evaluation of mechanical properties of plasma sprayed hydroxyapatite coatings,» *Applied Surface Science,* vol. 303, p. 155–162. , 2014.

[116] M. F. Hasan, J. Wang et C. Berndt, «Determination of the Mechanical Properties of Plasma-Sprayed Hydroxyapatite Coatings Using the Knoop Indentation Technique,» *Journal of Thermal Spray Technology ,* vol. 24, n° 15, p. 865–877, 2015.

[117] L. łatka, L. Pawłowski, D. Chicot, C. Pierlot et F. Petit, «Mechanical properties of suspension plasma sprayed hydroxyapatite coatings submitted to simulated body fluid,» *Surface and Coatings Technology,* vol. 205, n° 14, p. 954–960, 2010.

[118] L. Fu, K. Khor et J. Lim, «Processing, microstructure and mechanical properties of yttria stabilized zirconia reinforced hydroxyapatite coatings,» *Materials Science and Engineering: A,* vol. 316, n° 11–2, p. 46–51, 2001.

[119] M. Morks et A. Kobayashi, «Influence of spray parameters on the microstructure and mechanical properties of gas-tunnel plasma sprayed hydroxyapatite coatings,» *Materials Science and Engineering: B ,* vol. 139, n° 12–3, p. 209–215, 2007.

[120] G. Singh, S. Singh et S. Prakash, «Surface characterization of plasma sprayed pure and reinforced hydroxyapatite coating on Ti6Al4V alloy,» *Surface and Coatings Technology,* vol. 205, n° 120, p. 4814–4820, 2011.

[121] L.-H. He, O. Standard, T. T. Huang, B. Latella et M. Swain, «Mechanical behaviour of Porous Hydroxyapatite,» *Acta Biomaterialia,* vol. 4, n° 13, p. 577–586, 2008.

[122] J. Halpin et J. Kardos, «Moduli of Crystalline Polymers Employing Composite Theory,» *Journal of Applied Physics,* vol. 43, p. 2235–2241, 1972.

[123] B. Crist, C. Fisher et P. Howard, «Mechanical properties of model polyethylenes: tensile elastic modulus and yield stress,» *Macromolecules,* vol. 22, p. 1709–1718, 1989.

[124] R. Hill, «A self-consistent mechanics of composite materials,» *Journal of the Mechanics and Physics of Solids,* vol. 13, p. 213–222, 1965.

[125] B. Budiansky, «On the elastic moduli of some heterogeneous materials,» *Journal of the Mechanics and Physics of Solids,* vol. 13, n° 14, p. 223–227, 1965.

[126] N. Okui et T. Sakai, «Effect of monomeric unit length on crystallinity and Young's modulus for highly oriented fibers,» *Polymer Bulletin,* vol. 16, p. 79–85, 1987.

[127] M. Doyle, «On the Effect of Crystallinity on the Elastic Properties of Semicrystalline Polyethylenes,» *Polymer Engineering and Science,* vol. 40, n° 12, p. 330–335, 2000.

[128] J. Janzen, «Elastic Moduli of Semicrystalline Polyethylenes Compared with Theoretical Micromechanical Models for Composites,» *Polymer Engineering and Science,* vol. 32, n° 117, p. 1242–1254, 1992.

[129] K. Markov et L. Preziosi, «Elementary Micromechanics of Heterogeneous Media,» chez *Heterogeneous Media: Modelling and Simulation*, Boston, Birkhauser, 2000, p. 1–162.

[130] R. Landauer, «The Electrical Resistance of Binary Metallic Mixtures,» *Journal of Applied Physics,* vol. 23, p. 779–784, 1952.

[131] S. Humbert, O. Lame, R. Séguéla et G. Vigier, «A re-examination of the elastic modulus dependence on crystallinity in semicrystalline polymers,» *Polymer,* vol. 52, n° 121, p. 4899–4909, 2011.

[132] A. Singhal, J. Almer et D. Dunand, «Variability in the nanoscale deformation of hydroxyapatite during compressive loading in bovine bone,» *Acta Biomaterialia,* vol. 8, n° 17, p. 2747–2758, 2012.

[133] A. Zamiri et S. De, «Mechanical properties of hydroxyapatite single crystals from nanoindentation data,» *Journal of the mechanical behavior of biomedical materials,* vol. 4, n° 12, p. 146–152, 2011.

[134] A. Bandini, D. Chicot, P. Berry, X. Decoopman, A. Pertuz et D. Ojeda, «Indentation size effect of cortical bones submitted to different soft tissue removals,» *Journal of the Mechanical Behavior of Biomedical Materials,* vol. 20, p. 338–346, 2013.

[135] A. Korsunsky, M. McGurk, S. Bull et T. Page, «On the hardness of coated systems,» *Surface and Coatings Technology,* vol. 99, n° 11–2, p. 171–183, 1998.